# An experimental and numerical investigation of vaporizer tubes associated with micro gas turbines

by
André Jacobus Olivier

*Thesis presented in partial fulfilment of the requirements for the degree of Master of Engineering (Mechanical) in the Faculty of Engineering at Stellenbosch University*

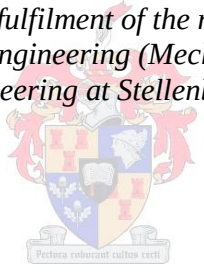


Supervisor: Prof Christian J Meyer

March 2015

## Declaration

By submitting this thesis electronically, I declare that the entirety of the work contained therein is my own, original work, that I am the sole author thereof (save to the extent explicitly otherwise stated), that reproduction and publication thereof by Stellenbosch University will not infringe any third party rights and that I have not previously in its entirety or in part submitted it for obtaining any qualification.

……

Date: 2014/11/28

## Abstract

**An experimental and numerical investigation of vaporizer tubes associated with micro gas turbines**

A.J. Olivier

*Department of Mechanical and Mechatronic Engineering, Stellenbosch University, Private Bag X1, Matieland 7602, South Africa.*
*Thesis: MEng. (Research), (Mechatronic)*

March 2015

This study is an introductory investigation into vaporizer technology as implemented in micro gas turbines. Experimental investigations are aimed at the development of expectations concerning the internal flow structure though vaporizers by generating application specific flow maps. Consolidation of these maps with other experimental data suggests that annular flow leads to increased evaporation rates. In addition, it was discovered that flow structure is affected by the injection angle and air and fuel flow rates. An investigation into the numerical modelling of vaporizers is based on two phase flow theory using a flow structure approach. The numerical behaviour is observed for parametric variations to establish the impact of assumptions. A final numerical model is formulated with empirically determined coefficients with fair correlation to experimental data. The results of this study yield recommendations towards the implementation and analysis of vaporizers with applied use in micro gas turbines.

## Uittreksel

**Eksperimentele en numeriese ondersoek**

**van verdampers met betrekking tot mikro gasturbines**

A.J. Olivier

*Departement van Meganiese en Megatroniese Ingenieurswese, Universiteit van Stellenbosch, Privaatsak X1, Matieland 7602, Suid-Afrika.*
*Tesis: MIng. (Navorsing), (Megatronies)*

Maart 2015

Hierdie studie is 'n inleidende ondersoek na verdamper tegnologie soos toegepas in mikro gasturbines. Eksperimentele ondersoeke is gerig op die ontwikkeling van kennis rakende die interne vloeistrukture deur verdampers met die bou van toepassingspesifieke vloeikaarte. Konsolidering van hierdie kaarte met verdere eksperimentele data dui daarop dat annulêre vloei lei tot verhoogde verdampingstempo's. Daar is ook bevestig dat die vloei struktuur deur die inspuitingshoek en vloeitempo's affekteer word. 'n Ondersoek na die numeriese modellering van verdampers is gebasseer op twee-fase vloei met 'n vloeistruktuur benadering. Die numeriese gedrag is waargeneem vir parametriese variasies om sodoende die impak van aannames te bevestig. Die numeriese model is voltooi met empiriese bepaalde koëffisiënte en lei tot goeie korrelasie met eksperimentele data. Resultate van hierdie studie lei tot aanbevelings rakende die implementering en ontleding van verdampers met spesifieke toepassing op mikro gas turbines.

## Acknowledgements

I would like to acknowledge the following people whom have made the fulfilment of this project possible:

- My supervisor, Prof Chris Meyer, for his support during this project.
- The CSIR for the funding of this project.
- Mr David Krige, for invaluable assistance and guidance with the experimental procedures.
- The Mr Cobus Zietsman and the entire workshop staff at the Department of Mechanical and Mechatronic Engineering for their guidance, advice and assistance.
- My fellow post graduate colleagues whose office time conversations had led to many insights.
- Lastly, my parents for always supporting me through the best and the worst of times.

## Table of contents

## List of figures

**Page**

## List of tables

**Page**

## Nomenclature

| | | |
|---|---|---|
| $d$ | Diameter | $[m]$ |
| $g$ | gravitational acceleration | $[9.81\ m/s^2]$ |
| $h$ | heat transfer coefficient / enthalpy | $[J/sm^2K\ ]$ or $[J/kgK]$ |
| $h_{fg}$ | latent heat of vaporization | $[J/kg]$ |
| $k$ | thermal conductivity | $[J/mK]$ |
| $m$ | Mass | $[kg]$ |
| $p$ | perimeter | $[m]$ |
| $t$ | time | $[s]$ |
| $u$ | internal energy/uncertainty | $[J]$ or $[-]$ |
| $v$ | velocity | $[m/s]$ |
| $x$ | mass fraction / axial position | $[-]$ or $[m]$ |
| $A$ | Area | [m^2] |
| $D$ | external diameter | $[m]$ |
| $F$ | View factor | $[-]$ |
| $M$ | Molecular weight | $[kg/mol]$ |
| $P$ | Pressure | $[N/m^2]$ |
| $R$ | Thermal resistance / Universal gas constant | $[K/sJ]$ or $[J/kgK]$ |
| $T$ | Temperature | $[K]$ |
| $Q$ | heat transfer rate | $[J/s]$ |
| $\alpha$ | Void factor | $[-]$ |
| $\beta$ | Numerical damping factor | $[-]$ |
| $\delta$ | Film thickness | $[m]$ |
| $\varepsilon$ | Emissitivity/error | $[-]$ or $[-]$ |
| $\theta$ | Angle | [rad] |
| $\mu$ | Viscosity | $[Ns/m^2]$ |
| $\rho$ | Density | $[kg/m^3]$ |
| $\sigma$ | Stefan boltsman constant | $[5.6704 \times 10^{-8}\ W/m^2K^4]$ |
| $\tau$ | Shear stress | $[N/m^2]$ |
| $\Phi$ | Damping factor | $[-]$ |
| $Nu$ | Nusselt number | $[-]$ |
| $Pr$ | Prandtl number | $[-]$ |
| $Re$ | Reynolds number | $[-]$ |
| $Vol$ | Volume | $[m^3]$ |

Acronyms

| | |
|---|---|
| AFR | Air-to-fuel ratio |
| AGARD | Advisery Group for Aerospace Research and Development |
| BMT | Beard Model Turbine |
| CSIR | Counsel for Scientific and Industrial Research |
| GTBA | Gas Turbine Builders Association |
| MGT | Micro gas turbine |
| NIST | National Institute of Standards and Technology |
| NOx | Nitrogen oxides |
| NREC | Northern Research and Engineering Counsel |
| P&ID | Process and Instrumentation diagram |

Subscripts

| | |
|---|---|
| $w$ | relation to wall shear forces |
| $cb$ | Convective boiling |
| $nb$ | Nucleate boiling |
| $mix$ | Mixture |
| $A$ | Air |
| $G$ | Gas |
| $L$ | Liquid (referring to liquid paraffin) |
| $V$ | Vapour |

Accents

| | |
|---|---|
| $\bar{}$ | Averaged value |
| $\dot{}$ | time derivative |
| $'$ | distance derivative |

# 1.
# Introduction

Vaporizer tubes aid the phase transition of liquid fuel to gas and as such play an important role towards promoting combustion. Their use in aero-derived gas turbine combustors is well-known and they provide noteworthy benefits for small and micro gas turbines (Barnes, 1954).

This study aims to review the fundamental operation of vaporizer tubes as a fuel injection system, experimentally investigate the operational conditions of straight through vaporizer tubes and establish a numerical modelling approach to analytically investigate the vaporization performance. Through experimental investigations, trends relating measured vaporization sensitivity to expectant flow regime are observed. Analytical investigation using the developed numerical model supports this behaviour and further yields insight to expectant vaporizer behaviour and numerical modelling limitations. A review of the work presented in this study along with recommendations on areas of current concern is presented in this section.

## 1.1 Background

Vaporizers are a fuel injection system used in combustion chambers. They act to assist phase transition of liquid fuel injected into combustion chambers and result in optimising the combustion reaction. Despite their operational importance, vaporizers and their operational characteristics are not as well defined as many other components within gas turbine engines (Englar, 2010). The increasing interest towards micro gas turbines (MGTs) has re-established much interest into ill-defined components such as vaporizer tubes in order to improve performance and develop more cost-effective MGTs (De Villiers, 2014).

This study forms part of a collaborative tertiary education research project administered by the Counsel for Scientific and Industrial Research (CSIR) to develop gas turbine knowledge. This study aims to investigate vaporizer tubes as a focus area of research into improving combustion chamber performance.

## 1.2 Motivation

The motivation for research towards gas turbine technology is of strategic importance to industry development both on an international and national scope. The global gas turbine market is a multi-billion Rand industry and predicted to grow steadily in the future (De Villiers, 2014). The intellectual wealth which

constitutes much of the value for this industry, however, is largely isolated within Northern hemisphere countries in America and Europe. Due to the current global socio-political climate, access to these industries is often restricted. This lends the development of such an industry within a developing country to be potentially very advantageous and profitable.

The motivation to investigate the combustor is the pivotal importance which it plays in gas turbine operation. Although stable combustion seems effortless in well-developed combustors, achieving such performance requires successful implementation and collaboration of many complex phenomena and fluid dynamics. Additionally, many problems manifest in other components with improper combustor designs. The low manufacturing cost and high operational importance results in high value to be placed on knowledge regarding combustor design and development.

The motivation to focus on vaporizer tubes with the current study is the significance vaporization has in combustor performance. Their specific operation strongly influences other aspects of combustor design and their use is seen in many commercially available MGTs (Gonzalez, Wong, & Armfield, 2007). Despite this, public access to knowledge pertaining to vaporizer operation is limited both in quantity and scope (Englar, 2010).

## 1.3 Objectives

The objective of this study is the development of knowledge to promote vaporizer tube performance with MGT combustors with applied focus on the Beard Model Turbine (BMT) 120KS MGT shown in Figure 1-1.

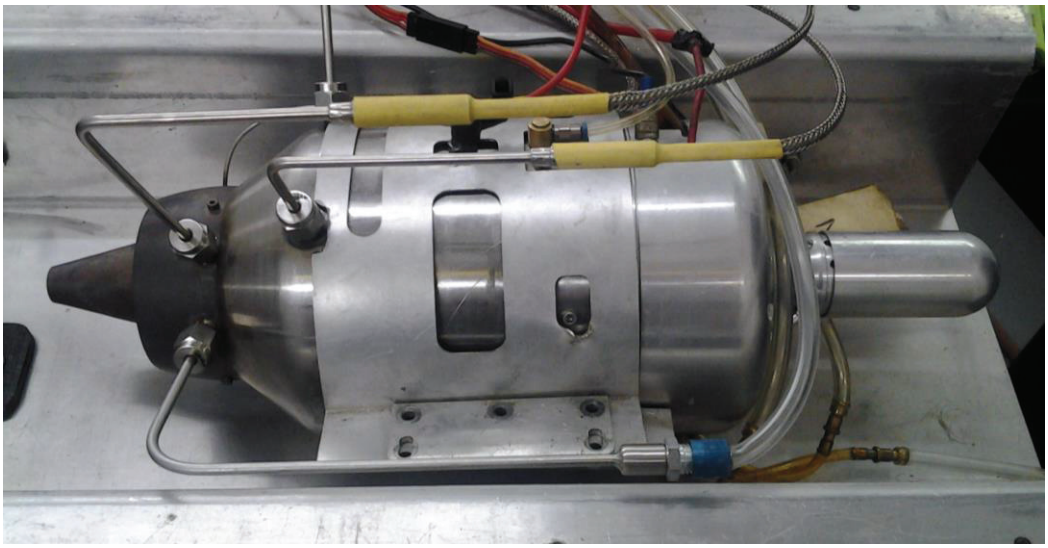

**Figure 1-1 Beard Model Turbine 120 KS on test bench**

The proposed objectives are achieved by three focus activities:

- A review of the current knowledge pertaining to the operation of vaporizer tubes as a fuel injection system and associated knowledge
- Experimental investigation of the influence of operational flow conditions on the vaporization performance of vaporizers and determining of operational boundaries
- Development of a sample numerical model using applied theoretical treatments presented in literature

The results of this project are intended to direct future endeavours towards improvement of vaporizer analyses and implementation strategies.

## 1.4 Investigative focus and approach

This study focuses on developing and executing investigations aimed at experimentally determining vaporizer operational parameters and numerically inspecting a proposed numerical modelling approach. Input arguments and resulting recommendations are aimed towards advancing performance of the BMT 120 KS MGT.

This study is intended as an introductory investigation and as such aims to form a basis of knowledge to direct future endeavours. The development of experimental and analytical approaches is based on a review of literature pertaining to gas turbines, fluid dynamics and heat and mass transfer. The experimental data is used to assist the development of numerical modelling and as such acts to indicate behaviours and adequacy of the proposed numerical treatment in predicting vaporizer performance.

The experimental and analytical scope of this project is limited to steady state operational scenarios experienced by the BMT 120 KS MGT. These operational conditions have been measured during prior studies on the BMT 120 KS at standard temperature and pressure conditions with paraffin and vaporizer geometry similar to that used for the current study. (Krige D. , 2013)

# 2.
# *Literature review*

Vaporizer tubes are used as a fuel injection method in gas turbine combustors. They act to facilitate the phase transition of liquid fuel to gas prior to combustion which poses advantages over other fuel injection systems for combustion attributes applied to MGTs (Barnes, 1954). The co-operative nature of vaporizer tubes with the other combustor components and combustion process itself necessitates a review of suitable literature to start with the combustor unit itself. Thereafter a more detailed review of vaporizer tubes and the combustion process follows. Relevant heat transfer and fluid dynamic theories are discussed within this section and are concluded with a presentation of previous work conducted and associated uncertainties towards the investigation of vaporizer tubes.

## 2.1 Gas turbine combustors

Vaporizers have a long history of use in gas turbine combustors and remain an important technology to achieve combustor requirements. The success of modern gas turbines and their associated components are arguably the consequence of the pioneering work conducted by Frank Whittle (Whittle, 1946) during the Second World War. Since then, much refinement and optimisation have been achieved through research and development with modern combustors achieving near ideal combustion efficiencies (Henderson & Blazowski, 1989). Vaporizers arguably played an important role in facilitating the continuous progress observed in the field of gas turbine technology over the past century and even more so with the increased interest in scaled gas turbines.

### 2.1.1 General design and operation

Gas turbines engines, such as the Rolls Royce EJ200 found on the Eurofighter Typhoon both shown in Figure 2-1, operate on the Brayton cycle shown in Figure 2-2. Idealised, this cycle starts with the isentropic compression of a gas initially at a low temperature and pressure. The compression of the gas, shown as the movement from point 1 to 2 on Figure 2-2, results in increasing the pressure thereby reducing its specific volume and increasing the temperature. Isobaric heat addition, presented by the movement from point 2 to 3 on Figure 2-2, is where energy is added to the working fluid. In gas turbine engines, this process is the responsibility of the combustor unit. The final stage of the cycle, isentropic expansion, occurs as the heated gas expands through the turbine section. The completion of the cycle is obtained from isobaric heat rejection to the atmosphere.

From the depiction of this cycle it is evident that the thermodynamic efficiency of a gas turbine cycle is influenced by the efficiencies whereby heat addition, compression and expansion are achieved. The promotion of heat addition efficiency, whilst minimising pressure decline due to flow resistance are the key focus of combustors.

(a) Eurofighter Typhoon (Gronemann, 2012)

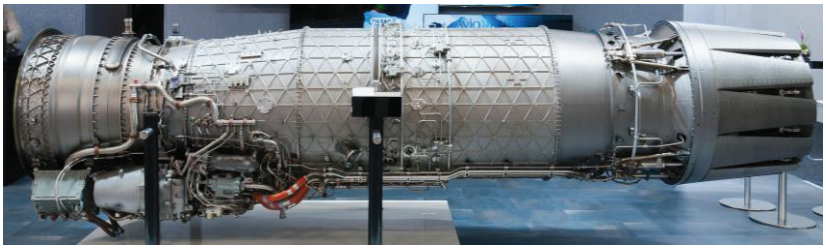

(b) Rolls Royce EJ200 (Herzog, 2013)

**Figure 2-1 Modern gas turbine engines using vaporizer tubes**

(adapted from (Gronemann, 2012) and (Herzog, 2013))

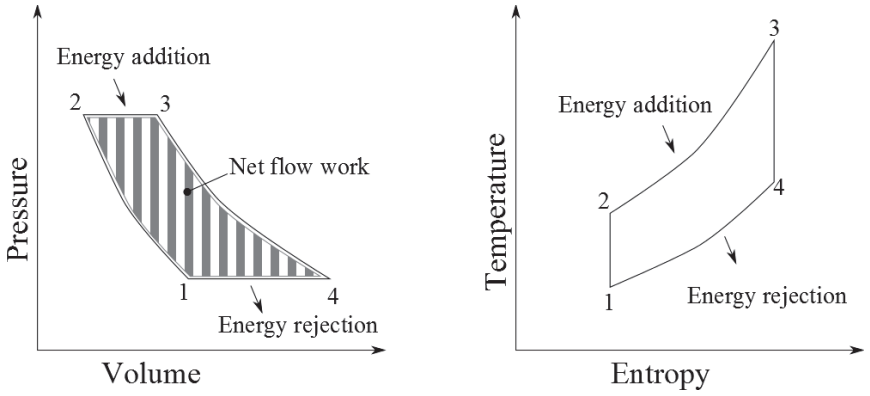


**Figure 2-2 Ideal Brayton cycle**

By definition, combustors are devices situated between the compressor and turbine sections of a gas turbine engine with the purpose to facilitate isobaric heat

addition by means of combustion. Achieving these conditions is, however, met with difficulties arising from the balance between combustion efficiency and flow resistance. These two aspects result in introducing significant complexity to the design and operation of combustors in order to achieve and optimise combustion. The rapid development of gas turbine technologies during the Second World War led to many designs as shown in Figure 2-3.

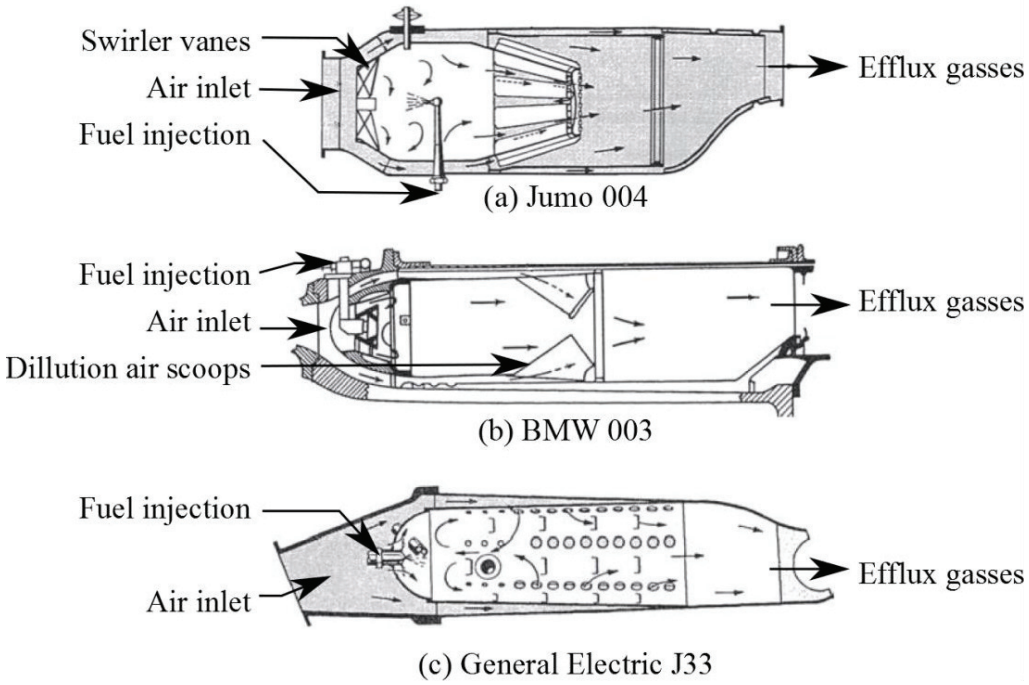


**Figure 2-3 Early combustion chambers**

(Adapted from (Lefebvre & Ballal, 2010, pp. 5,6,7))

The development of these engines produced much needed empirical data and design experience to derive recommendations and guidelines from. Refinement of combustor technologies has resulted in contributing to and defining combustor requirements ever since. Some of the cardinal requirements of modern combustors (Lefebvre & Ballal, 2010, p. 9) are:

- High-combustion efficiency
- Ignition reliability
- Low pressure loss
- Produce desired exhaust temperature profile
- Produce low smoke and particle emissions
- Have a wide range of combustion stability
- Minimise manufacturing costs
- Increased durability and maintainability
- Size

These requirements are addressed by the configuration of three components which collectively make up the combustor. These components are the diffuser, the combustor liner and the fuel injection system. The configuration and design preference of each of these components vary greatly based on combustor and engine requirements. Nevertheless, the basic configuration of all combustors is similar to that shown in Figure 2-4.

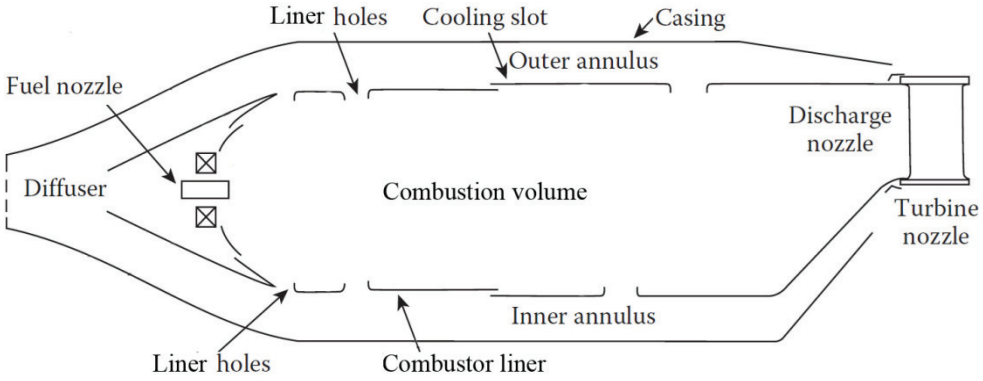


**Figure 2-4 Basic anatomy of a combustion chamber**

(Adapted from (Lefebvre & Ballal, 2010, p. 18))

Conventional combustor design methodology starts with the selection and configuration of the diffuser and combustion liner. These components are often implemented as a single component with varying geometry. Both liner and diffuser act to disrupt the flow of air through the combustor in such a way to promote favourable combustion conditions and minimise flow losses. This is achieved by reduction of the gas velocity through the combustor and topical flow admittance. The reasons for retarding and selective admittance of the flow is to reduce major flow-losses which are proportional to the square of the fluid's velocity and to attain areas of recirculation to anchor combustion which are within lean/rich extinguish limits.

In order to quantify this design rationale and relate holistic combustor parameters to more detailed design iterations, reference values as presented by the Northern Research and Engineering Council (NREC) (1980) are used. The two most prominent reference values are those representing the reference velocity and dynamic pressure through the combustor as defined in equations 2-1 and 2-2 respectively.

$$v_{ref} = \frac{\dot{m}_{combustor}}{\rho_{upstream} A_{liner}} \qquad 2\text{-}1$$

$$q_{ref} = \frac{\rho_{upstream} v_{ref}^2}{2} \qquad 2\text{-}2$$

The terms presented in equation 2-1 relate to the air mass flow through the combustor, $\dot{m}_{combustor}$, the density of the air upstream of the combustor, $\rho_{upstream}$, and the cross sectional area of the combustor liner, $A_{liner}$.

These two reference quantities are used extensively to relate combustor design parameters to conditions apparent just upstream of the combustor. This is useful as these conditions are easily obtained from compressor performance requirements and little further information is needed from the combustor itself.

### 2.1.2 Combustor pressure drop and liner design

The pressure drop over the combustor is quantified as shown in equation 2-3.

$$\Delta P_{combustor} = \Delta P_{liner} + \Delta P_{diffuser} + \Delta P_{combustion} \qquad 2\text{-}3$$

The three pressure drop parameters presented in equation 2-3 represent the pressure drops attributed to the liner, the diffuser and the combustion process respectively. The diffuser pressure drop is usually an unavoidable loss to the system, but its influence should be noted (Lefebvre & Ballal, 2010). The liner and combustion pressure drops are, however, represented as shown in equations 2-4 and 2-5 respectively.

$$\Delta P_{liner} = \frac{R}{2}\left(\frac{\dot{m}_{combustor}^2 T_{upstream}}{A_{h,effective}{}^2 P_{upstream}}\right) \qquad 2\text{-}4$$

$$\Delta P_{combustion} \cong q_{ref}\left(\frac{T_{downstream}}{T_{upstream}} - 1\right) \qquad 2\text{-}5$$

The effective hole admission area, $A_{h,effective}$, incorporates the discharge characteristics with the geometric areas of liner holes as defined in equation 2-6.

$$A_{h,effective} = \sum C_{D,i} A_{h,i} \qquad 2\text{-}6$$

Thermodynamic efficiency, with respect to the Brayton cycle, is proportional to the increase in temperature that can be attained. Thus, the combustion pressure drop is practically limited by its proportionality to the reference dynamic pressure. Introduction of the reference velocity into the dynamic pressure argument reveals that the combustion pressure drop is inversely proportional to the square of the cross sectional area of the combustor liner. Similarly, the liner pressure drop is inversely proportional to the square of the effective hole area. Both of these relations are made assuming all other parameters are fixed by design. Although an increase of these two parameters will therefore result in a reduction of the

pressure loss, practical restrictions often negate excessive scaling and limit the combustor liner cross sectional area. The effective liner admission area is thus one of the critical design parameters available to optimise combustor design.

The effective liner admission area as shown in equation 2-6 is proportional to the size, discharge coefficient and number of holes. There are many hole designs and thus also many correlations and recommendations to assist in the selection and design of specific hole configurations. Fundamentally these holes restrict or allow air flow into the inner combustor volume in specific amounts to achieve efficient combustion and desired exhaust temperature profile. Placement of holes is, therefore, directed largely by combustion and thermal quenching concerns.

Definite discretion of where combustion starts and ends is difficult to determine due to the turbulence present during combustion. In order to assist design and analysis of combustion chambers, it has become convention to divide the combustion chamber into three combustion zones as shown in Figure 2-5. Each of these three zones is tasked to address to a larger or lesser degree the combustion and thermal quenching requirements of the combustor. (NATO, 1971, pp. 4-12)

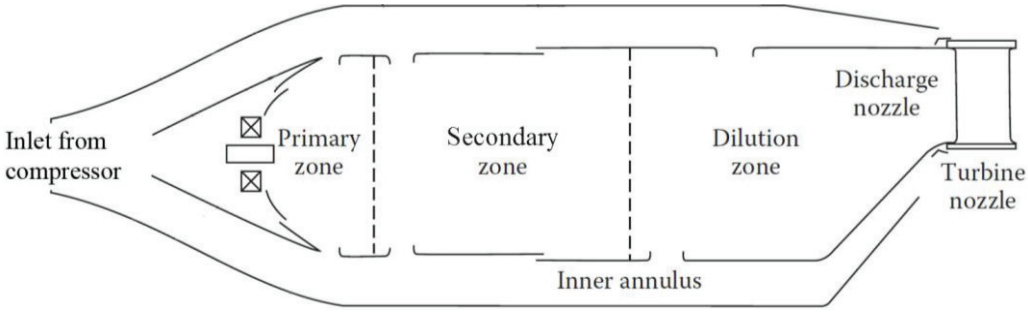


**Figure 2-5 Inner combustion zones**

(Adapted from (Lefebvre & Ballal, 2010, p. 3))

The primary combustion zone is tasked with the sole purpose to provide a favourable volume for combustion to occur. This requires the specific air-to-fuel ratio (AFR) permitted into this area to be well within combustion extinguish limits. The primary combustion zone should also provide conditions to promote ignition and re-light reliability over the entire operational spectrum. (Mattingly, 2006, p. 761)

The secondary combustion zone is tasked with completion of any incomplete combustion and to start conditioning the high temperature combustion gasses towards thermal quenching requirements. (Mattingly, 2006, p. 761)

The dilution zone aims to quench any continued combustion and distribute the hot combustion gasses as is desired for the exhaust temperature profile. (Mattingly, 2006, p. 761)

### 2.1.3 Fuel injection systems

Fuel injection systems supply fuel to the combustion process and thereby directly interact with the primary combustion zone. Various fuel injection devices exist, but generally all these devices can be described as injecting the fuel either directly into or upwind of the combustion area and as either using pressure atomization or vaporization to achieve fuel dispersion (Henderson & Blazowski, 1989).

The majority of combustion applications use direct injection of fuel into the combustion zone. The reason for this is that flashback and combustion instability may occur with upwind/premixed injection. Both these considerations pose significant safety and operational risks. (Henderson & Blazowski, 1989)

Selection between pressure atomizers and vaporizers is, however, a more involved process. Experimentation with Whittle's earlier gas turbine engines led to both vaporizers and pressure atomizers to be installed into similar combustors as shown in Figure 2-6. Invaluable results were obtained from operating these combustors using both systems in otherwise similar conditions, but design specific advantages led to both technologies surviving the test of time.

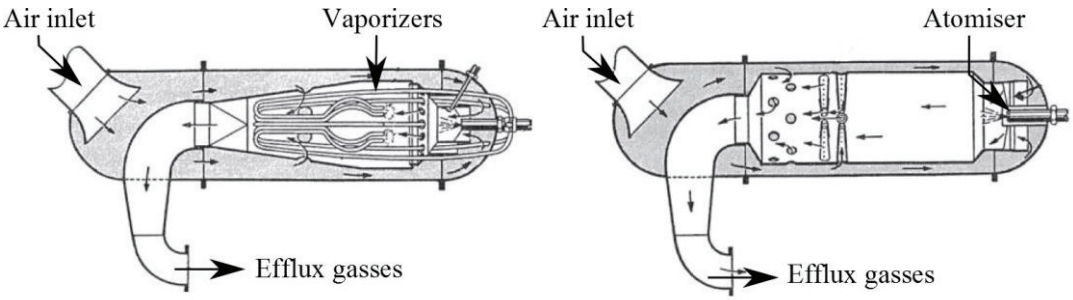


(a)Using vaporizer injection (b) Using atomiser injection

**Figure 2-6 Early Whittle combustion chamber**

(Adapted from (Lefebvre & Ballal, 2010, p. 3))

Selection factors that distinguish fuel injection systems in modern gas turbine engines are fuel flow range, maintenance requirements and combustion responsiveness (Lefebvre A. , 1989). The specific influence with regards to combustor design by using vaporizers is deduced from its influence on the effective hole area term shown in equations 2-6. As vaporizers also permit air and therefore act as a type of hole, the effective hole area is increased accordingly.

### 2.1.4 Application in gas turbines

Over the past century developments in combustor design have addressed the 9 listed requirements according to specific operational requirements with much success. Modern gas turbines readily achieve combustion efficiencies up to 99%

and liner pressure drops of around 3% of the total upstream pressure (NATO, 1971, pp. 1-11). MGT combustors, however, do not yet meet these performance figures. Investigations by Barnes (1954), NATO (1971, pp. 4-13) and Henderson & Blazowski (1989, p. 128) have concluded that vaporizer tubes result in promoting combustion conditions in such a way as to contribute to resolving these shortcomings in MGT combustors, despite reported bad ignition reliability.

Vaporizer tubes are documented to have been in use with gas turbine combustors as early as 1941 (Whittle, 1946) with this design shown in Figure 2-6. Whittle (1946) reported that vaporisers provided adequate performance, but were prone to thermal cracking and blockage. The development of vaporizers since then has resulted in addressing these issues and in doing so resulted in simplifying and enhancing vaporizer technology.

## 2.2 Vaporizer tubes

Vaporizer systems usually consist of a single or series of narrow tubes through which liquid fuel is passed into the primary combustion zone. These tubes are placed within the combustion volume and use the combustion heat to facilitate vaporization of the fuel. This section discusses the fundamentals surrounding vaporizer tubes, relating to the mechanisms that make them work and methods adopted to incorporate them into combustors.

### 2.2.1 Operation

The purpose of vaporizers is the vaporization of liquid fuel and topical dispersion of a reactive air-fuel mixture within the combustion chamber. This is achieved by promoting heat transfer from the hot combustion gasses to the fuel and positioning the outlet of the vaporizer within the primary combustion zone.

Heat transfer related to vaporizers occurs from the combustion heat through the vaporizer walls to the enveloped fluid. The heat transfer characteristics can therefore be altered by adaptation of the exterior and interior fluid-surface interaction or the vaporizer's material properties and geometry.

Due to the high heat of combustion, the majority of vaporizers are made of thermal resistant materials, such as Inconel. This increases their durability, but limits the variation of materials that can be selected.

Vaporizer geometry varies significantly with design. Various methods have been used to promote heat transfer characteristics, most of which have been based on experience or pseudo-scientific rationale.

Despite retained performance throughout operational spectrums, heat transfer through vaporizers is restricted by design and has been observed to lead to

vaporization inadequacies at high flow rates (Lefebvre & Ballal, 2010). Based on such observations, recommendations for the permitted air-to-fuel ratio (AFR) through the tubes have been separately determined to be 3 (NREC, 1980, pp. 6-44) and 6 (Barnes, 1954). It should be noted, however, that these recommendations have been deduced from experimental observations on vaporizers used in large gas turbine combustors.

### 2.2.2 Advantages and disadvantages

Vaporizers have significant advantages over alternative fuel injection systems which apply in particular to small and micro gas turbine applications.

The most significant of these advantages is the observed reduction of both required combustor height (NATO, 1971, pp. 4-13) and combustion length (Barnes, 1954) resulting from their use. These reductions are attributed to the topical injection of combustion reactants within the primary combustion zone which results in improved mixing and resulting reaction speed. The increased reaction speed consequently acts to further reduce the required combustion length by flattening the observed flame structure (Barnes, 1954). This observation is confirmed with numerical simulations conducted on a KJ66 MGT combustor (Gonzalez, Wong, & Armfield, 2007) as seen from the apparent flame front identified in Figure 2-7.

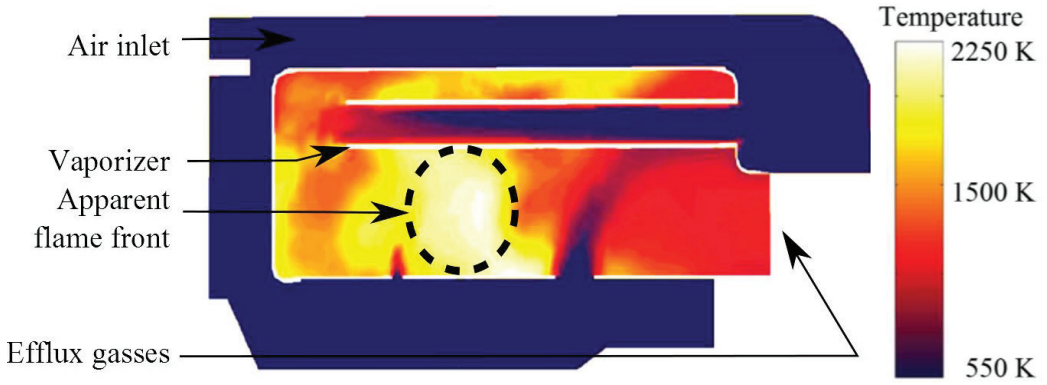


**Figure 2-7 Simulated thermal distribution within a KJ66 combustor**

(Adapted from (Gonzalez, Wong, & Armfield, 2007))

Fuel injection pressures are also greatly reduced compared to pressure atomisers and air blast atomisers. The reduced injection pressure results in fuel pumps to achieve a wider operational flow range and the rest of the fuel system to operate with reduced stress loading. The reduced stress on components results in reduced maintenance, less expensive designs due to lowered strength requirements and can lead to reduced overall component weight (Jasuja & Low, 1987).

The main disadvantages of vaporizers occur during start-up and re-ignition. The inherently slow transient response and required perpetual operating conditions mean that vaporizers cannot produce an ignitable mixture by themselves without being heated externally or by incumbent heat. This also reduces re-ignition probability during flame extinction. As such, vaporizers require auxiliary components to aid with ignition during these scenarios.

### 2.2.3 Design adaptations for micro gas turbines

The first successfully scaled MGT was produced by Kurt Schreckling (GTBA, 1999) and used a coiled vaporizer tube as shown in Figure 2-8. This configuration maximised residence time within the combustion flame, but presented significant flow resistance within the combustion chamber and resulted in low performance output (GTBA, 1999).

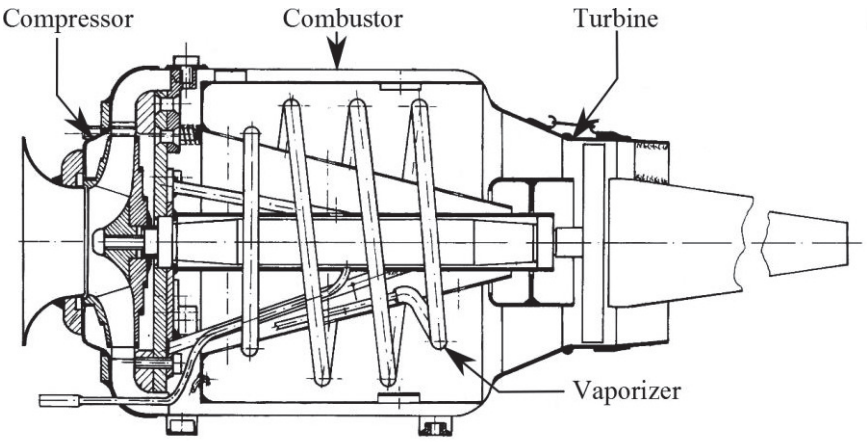


**Figure 2-8 FD3-64 MGT**

(adapted from (http://img.vx.com/uploadfile/data/2014/0126/))

Notable vaporiser design features on the FD3-64 MGT are the front entry and liquid only flow through the vaporizer tube. The front entry design is a popular configuration used for combustors, as the length of the vaporizer is reduced whilst still obtaining adequate fuel dispersion. Liquid only flow through the vaporizer tube result in flash vaporization as experienced by Whittle (1946). Additionally this implies that all primary zone air is introduced through admittance holes which reduce fuel dispersion. Although this configuration can result in obtaining adequate combustion, better fuel dispersion and reduction of the issues associated with flash vaporization is achieved with the inclusion of air into the vaporizer tube. Drawing from aviation gas turbine technologies, the hook or candy stick vaporizer design as shown in Figure 2-9 is often used in MGT combustors.

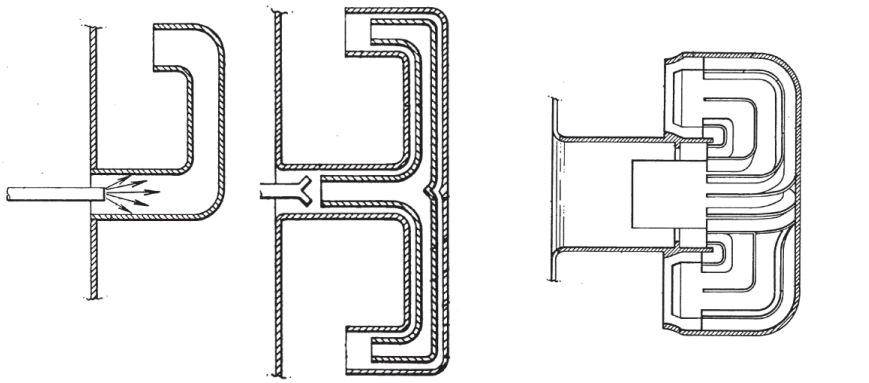

(a) simple (b) annular (c) annular with guide vanes

**Figure 2-9 Hook tube vaporizer designs**

(adapted from (Overton, Langley, & Millener, 1992))

The evolution of hook tube design shown in Figure 2-9 emphasizes achieving and promoting annular flow. This is apparent from designs 'b' and 'c' whereby fuel is passed only thought the outer annulus (Overton, Langley, & Millener, 1992).

The reduced size of MGT combustors lead to an inevitable increase in the combustor pressure drop as per the implications of equation 2-3 as previously discussed. This is confirmed by comparison of the reported pressure drops of 3% (NATO, 1971, pp. 1-11) and 12% (Gonzalez, Wong, & Armfield, 2007) relative to the upstream pressure for a large gas turbine and a MGT respectively. Reducing the flow resistance within the combustor volume is thus important to improve thermodynamic efficiency. The two previously discussed vaporiser designs, however, result in substantially increasing the flow resistance within the combustion volume when applied to MGT combustors. Therefore rear entry vaporizers as shown in Figure 2-10 are widely used in MGTs (GTBA, 2010).

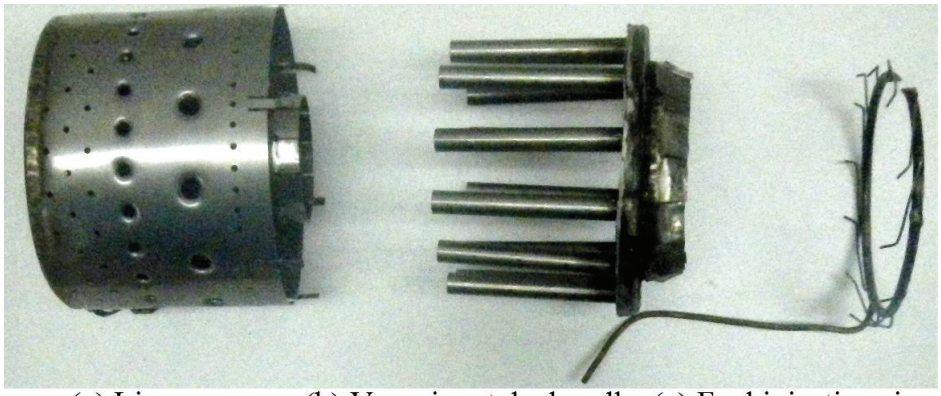

(a) Liner (b) Vaporizer tube bundle (c) Fuel injection ring

**Figure 2-10 BMT120KS rear entry vaporizer tube combustor disassembly**

The majority of rear entry vaporizers are straight in form, as the design shown in Figure 2-10, which make them resilient to blockage and easy to manufacture.

Observed design variations of these types of vaporizers are the addition of a slight curvature in the tubes and addition of internal flow inserts.

The curving of straight rear entry vaporizers results in promoting heat transfer by inducing more turbulence and forcing internal liquid-wall contact by adjusting the flow path. This form also reduces flow instability resulting from inaccurate spacing between the vaporizer outlet and impinged combustor wall (Englar, 2010). This design shown in Figure 2-11 is often referred to as a worm tube or Wren tube as this design was made popular by the Wren turbine company.

**Figure 2-11 Wren tube vaporizer manifold**

(adapted from (Englar, 2010))

Vaporizer tube inserts act to promote heat transfer by enforcing specific internal flow to occur. The use of inserts, however, increase the risk of blockages and manufacturing difficulty and have not yet been proven to promote performance much beyond the reach of alternative methods. Spiral inserts as shown in Figure 2-12 are the most widely cited type of insert in use with vaporizers for MGTs.

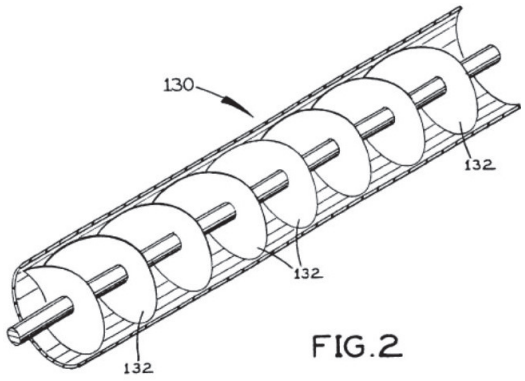


**Figure 2-12 Vaporizer tubes with inserts**

(adapted from (Rowley, 2003))

The presented vaporizer designs are widely used and seen in many modern MGTs (GTBA, 2010). The selection and specific adaption of these designs are, however, subject to artesian experience and preference leading to iterative prototyping still being conducted to optimise vaporizer operational functionality (Englar, 2010).

## 2.3 Combustion

Combustion is one of the most common occurring and widely applied chemical reactions in the world (Williams, 1985). It occurs when a fuel undergoes exothermic oxidization in the presence of an oxidizer. This section discusses the chemistry of combustion, the specific conditions applicable to combustion within gas turbines and implications of using vaporizers on the combustion process.

### 2.3.1 Combustion stoichiometry

The combustion reaction requires reactants to be energized to the point where molecules ionize and dissociative electrons become present. At this point the mixture transitions to plasma where reactants become highly reactive and molecular breakdown and oxidation can occur spontaneously. These processes result in large amounts of energy to be released. A small portion of this energy is required to perpetuate the reaction and the remainder is transferred to neighbouring gasses. The transferred excess energy energizes particles within the plasma such that they emit radiation within the visible spectral range and appear as a luminous flame. (Williams, 1985)

Industrial application of combustion often involves hydrocarbon polymer fuels, of which most notably are petrol, paraffin and diesel (Lefebvre & Ballal, 2010). These compounds do not have oxygen molecules inherent in their molecular structure and require oxygen from the environment or alternative source in order to combust. As the mixing movement of reactants is physically dependent, these types of fuels result in producing low velocity combustion, or deflagration. Ideal combustion of hydrocarbon fuels results in producing carbon dioxide, water and energy with the stoichiometric chemical reaction as shown in equation 2-7.

$$C_nH_m + \left(n + \frac{m}{4}\right)(O_2 + 3.78N_2) \rightarrow nCO_2 + \frac{m}{2}H_2O + 3.78\left(n + \frac{m}{4}\right)N_2 \qquad 2\text{-}7$$

Hydrocarbon fuels, however, consists of a mixture of various length hydrocarbon polymers and isomers. The specific combination of these compounds is dependent on source, processing procedures and history of the fuel (Barnes, 1954). Analyses of combustion with regards to combustor design are, however, simplified by using surrogate fuels. The surrogate fuels are assumed to be of a singular molecule type and present with similar combustion and other thermodynamic properties than the

multicomponent fuels. Recommended surrogates to be used for paraffin type fuels are Dodecane ($C_{12}H_{24}$ ) and Dodecene ($C_{12}H_{26}$) (Lefebvre & Ballal, 2010).

Ideally a slightly richer than stoichiometric AFR is desired within the primary combustion zone (Mattingly, 2006). The specific value of this ratio is dependent on the specific fuel used, which for paraffin with an stoichiometric AFR of around 15, results in values of around 10 to be recommended (Mattingly, 2006).

### 2.3.2 Combustion inefficiencies

Combustion inefficiencies manifest as the formation of nitrogen oxides (NOx), soot, carbon monoxide and unused fuel in the exhaust gasses. Increasing global emission regulations pressure combustion applications to reduce the emission of these particles. The formations of these particles are influenced by the combustion characteristics related to the degree of reactant mixing, combustion AFR, combustion temperatures and quench rate. (Lefebvre & Ballal, 2010)

### 2.3.3 Combustion implications on MGTs

Continuous combustion, as occurring within gas turbines, is the main reason for the industrial success of gas turbines. The reason being that continuous combustion does not require as high ignition repeatability as with discrete combustion, typically found in automobile engines. Therefore, gas turbine components can be refined to achieve optimal operating conditions regardless of the type or grade of fuel used. (Lefebvre & Ballal, 2010)

MGTs are, however, predominantly still only used in aviation applications which require a degree of resilience to operating condition variations and ignition reliability. The limits to these operating conditions where combustion can still be attained are influenced by several factors (Lefebvre & Ballal, 2010). The factors act to vary the energy transfer rate between combustion products and reactants.

The reduced size and associated component inefficiencies found on MGTs make them inherently less resilient to variations in operating conditions and fuel sources. As such, combustors and associated components are still built based on aviation fuel standards. Investigations have indicated that vaporizer tubes are very sensitive to the type of fuel (NREC, 1980), but fairly insensitive to changes in fuel quality (Barnes, 1954). Despite these and observed transient difficulties, the flattening of apparent flame structure and topical injection and dispersion of combustion reactants resulting from vaporizer usage make vaporizers specifically advantageous to use in MGT combustors. The reasons being are that the topical injection and dispersion promotes fuel and air mixing which improves flammability and the flattening of flame structure reduces the required combustor length.

## 2.4 Bulk fluid movement

The flow of fluids through a vaporizer is inherently turbulent. Furthermore it is highly dependent on the vaporizer and combustor design. The scope of discussion for this study is therefore limited to that expected to occur within a straight through rear entry vaporizer as installed on the BMT120KS MGT.

### 2.4.1 Expected fluid movement

The BMT 120 KS makes use of 12 equally spaced 80 mm vaporizers mounted on a rear manifold and protruding inwards towards the inner front wall surface of the combustor. The liquid is injected into each tube through a hypodermic needle which is positioned at an angle and at an offset with respect to the tube's axis. The in-situ configuration of this is shown in Figure 2-13.

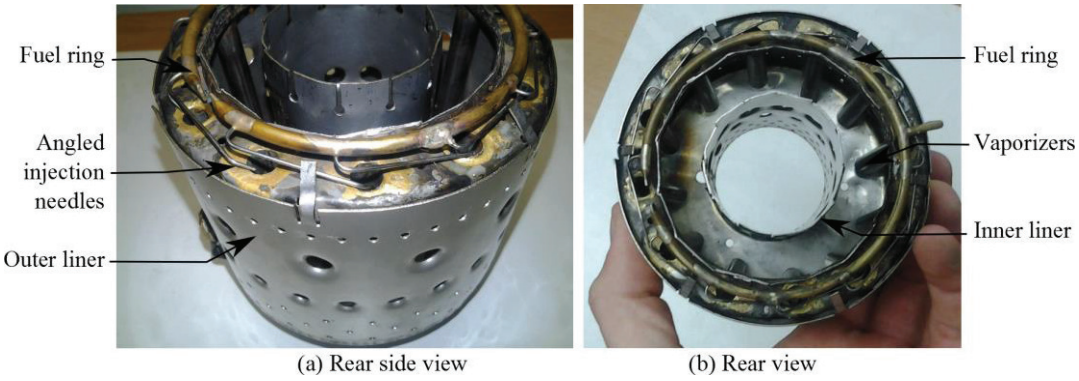


**Figure 2-13 BMT120KS vaporizer tube configuration**

The angled injection is intended to result in forcing the liquid into an annular flow structure within the tube. Observed flow rates over the operational range of the BMT 120 KS MGT as measured at sea-level with room temperature inlet conditions (Krige D. , 2013) are presented in Figure 2-14 with relation to operational speed. Measurement values are listed in Table A-4.

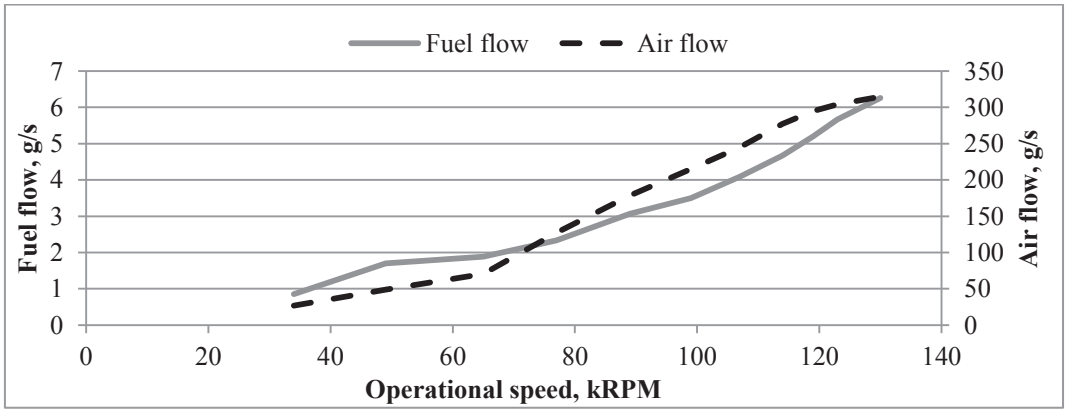


**Figure 2-14 Measured BMT 120 operational flow rates**

The amount of air permitted through the vaporizers is measured, as indicated in Appendix A, to vary between 3% and 5% of the total air flow under cold flow test conditions. Assuming uniform flow distributions between vaporizers, the expected flow ranges are between 0.071 and 0.522 g/s and between 0.067 and 1.312 g/s for paraffin and air respectively. These flow rates indicate in-tube AFRs between 0.943 and 2.513. Although adequacy of performance is deduced from observed operation of the BMT120KS MGT, no further information regarding the vaporizers is available.

The MGT orientation and therefore the vaporizer orientation are assumed to remain horizontal for this study. The bulk fluid theoretical treatment follows.

### 2.4.2 Control volume approach to two phase flow

The flow through a vaporizer, limited to the scenario as previously discussed, consists of a vaporizing liquid fuel and air mixture. The treatment of such a mixture as presented by Doster (2006) is presented here in summary.

A simplified incremental control volume representation of the flow is derived by grouping gaseous components together and assuming liquid and gas fluids are clearly separable by phase. This result in a volume as defined in Figure 2-15.

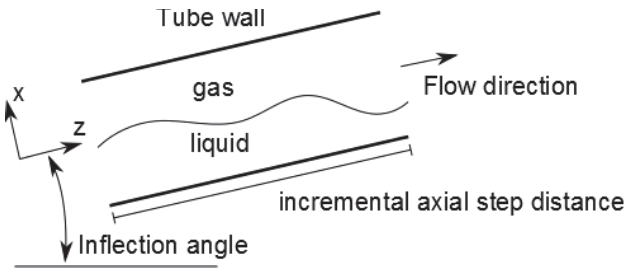


**Figure 2-15 Simplified representation of flow through a vaporizer**

Further isolation of individual phases as separate control volumes enable analytical treatment to further account for phasic interactions. Mass, energy and momentum conservation laws applied to the resulting control volumes lead to the graphical representations shown in Figure 2-16. Mathematical representation of the six resulting conservation equations represents the current state-of-the-art of two phase flow modelling (Doster, 2006).

Despite this model's accuracy and general validity, by not incurring any time or property dependant assumptions, its usage is limited due to its high computational requirements and the ill-defined nature of interphasic terms. Therefore, its use in industry is limited to academic purposes. More practical models are derived from the six-equation model as base by numerical manipulation in order to mitigate the aforementioned restrictions.

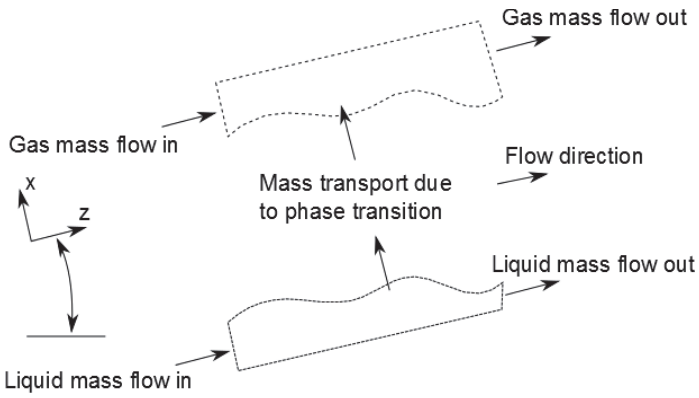


(a) Mass conservation applied to separate phasic volumes

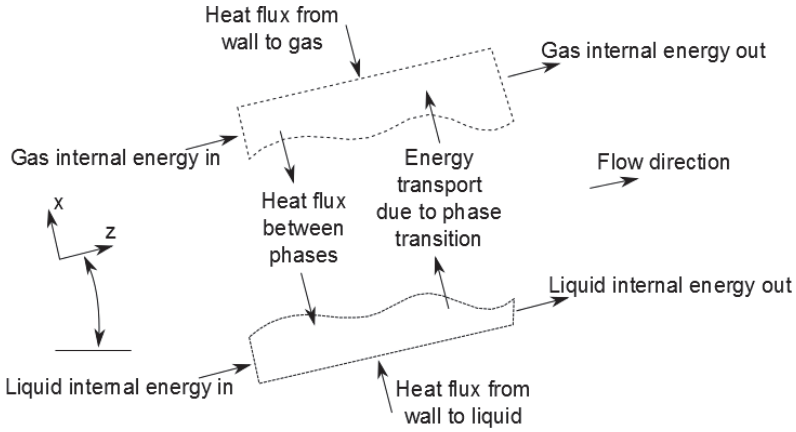


(b) Energy conservation applied to separate phasic volumes

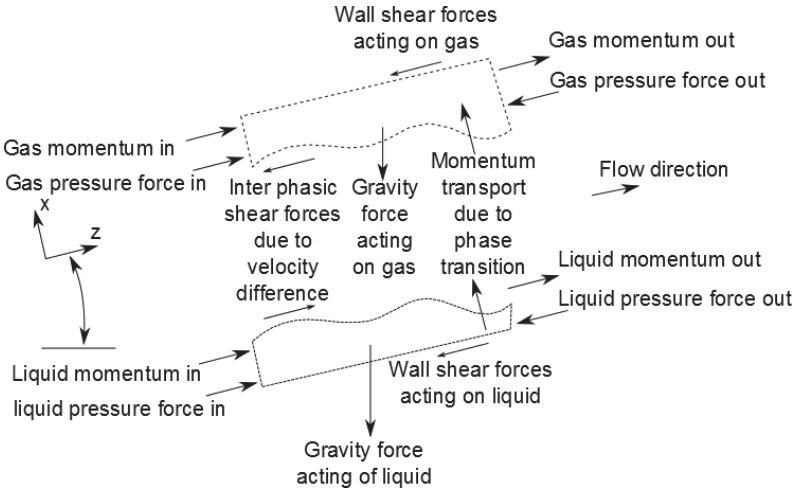


(c) Momentum conservation applied to separate phasic volumes

**Figure 2-16 Application of conservation laws to phasic volumes**

Summation of the respective conservation models results in eliminating these terms at the cost of losing analytical detail at the phasic interface. The resulting 3 numerical models representing the bulk mixture and shown in equations 2-8 through 2-10 is, however, more readily applicable to practical investigations and current capabilities (Doster, 2006).

$$\frac{\partial}{\partial z}\left(\sum_{i=L,G}\frac{\dot{m}_i}{A_{tube}}\right)+\frac{\partial}{\partial t}(\rho_{mix})=0 \qquad 2\text{-}8$$

$$\frac{\partial}{\partial z}\left(\sum_{i=L,G}\dot{m}_i h_i\right)+\frac{\partial}{\partial t}\left(\sum_{i=L,G}\alpha_i\rho_i u_i\, A_{tube}\right)=\dot{q}'_{w,total} \qquad 2\text{-}9$$

$$\frac{\partial}{\partial t}\left(\sum_{i=L,G}\dot{m}_i\right)+\frac{\partial}{\partial z}\left(\sum_{i=L,G}\frac{{\dot{m}_i}^2}{\alpha_i\rho_i {A_{tube}}^2}\right)+\frac{\partial}{\partial z}(P)=-\frac{(\tau_w\bar{p}_w)_{total}}{A_{tube}}-\rho_{mix}g\sin\theta \qquad 2\text{-}10$$

The three models shown above represent a transient two phase mixture model. This study is, however, limited to the study of steady state operation of vaporizers. Therefore time derivative terms may be neglected. Furthermore, the study aims to focus on horizontally orientated vaporizers as this is the orientation they predominantly operate at. The implication of this is that the static pressure gradient term of equation 2-10 equates to zero. Subsequently, equations 2-8 through 2-10 are simplified to equations 2-11 through 2-13.

$$\frac{1}{A_{tube}}\frac{\partial}{\partial z}\left(\sum_{i=L,G}\dot{m}_i\right)=0 \qquad 2\text{-}11$$

$$\frac{\partial}{\partial z}\left(\sum_{i=L,G}\dot{m}_i h_i\right)=\dot{q}'_{w,total} \qquad 2\text{-}12$$

$$\frac{1}{{A_{tube}}^2}\frac{\partial}{\partial z}\left(\sum_{i=L,G}\frac{{\dot{m}_i}^2}{\alpha_i\rho_i}\right)+\frac{\partial}{\partial z}(P)=-\frac{(\tau_w\bar{p}_w)_{total}}{A_{tube}} \qquad 2\text{-}13$$

This form of the mixture model conservation equations represents steady state horizontal flow of a two phase mixture. These equations are used as the basis for numerical modelling with empirical correlations adding to model definition.

### 2.4.3 Two phase flow regimes

Comprehensive detail modelling of two phase flows is complicated by the occurrence of large variation in apparent flow structures. The various flow structures result in grossly different flow interactions and behaviours. As such, pure analytical methods are not yet capable of describing two phase flows in general and treatment is limited to empirical models with limited applicability within defined flow regimes (Doster, 2006). Investigations into two phase flows therefore require guidance by a flow map which predicts flow regimes based on flow conditions.

Identified flow regimes include stratified, wavy, annular, frothy and intermittent flow as presented in Figure 2-17.

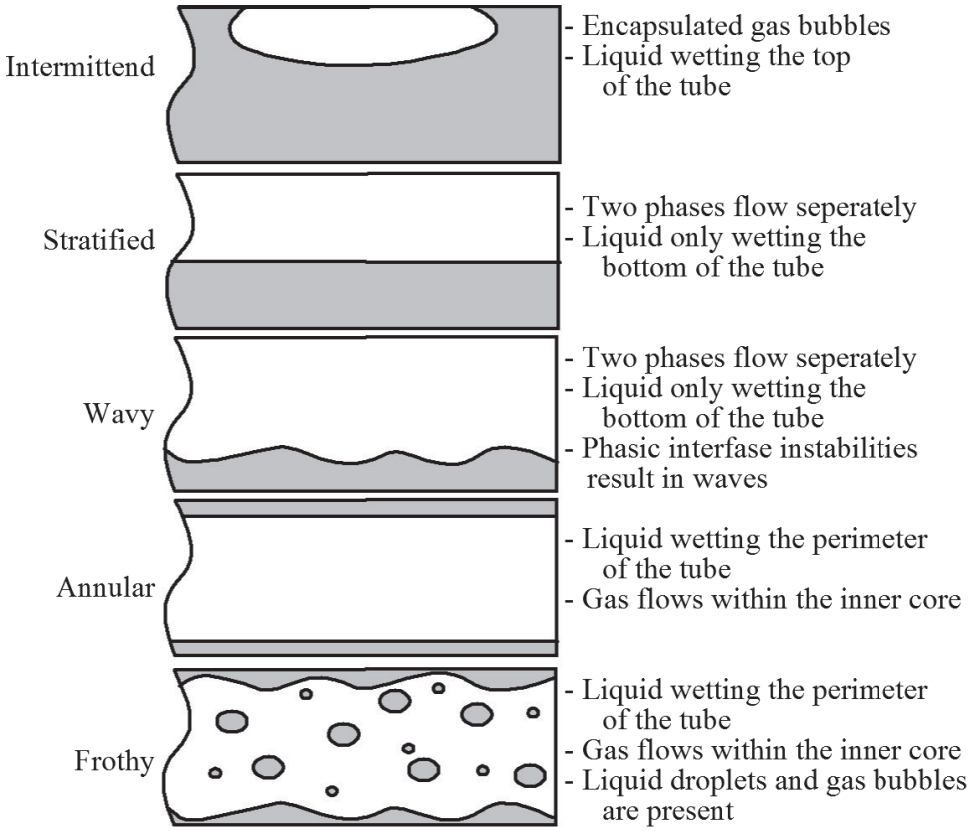


**Figure 2-17 Horizontal two phase flow regimes**

Notable flow maps applicable for horizontal two phase flow are that by Baker (1954) and Taitel-Dukler (1976) and more recently Wojtan et al (2005). These maps are, however, defined for limited flow mixtures, geometries and steadied flow conditions.

Flow maps are developed from visual observations of flow conditions. Accuracy of test data is further assisted by maintaining and minimising heat flux to the flow with boiling or condensing flows. No flow map exists, to the best of the author's knowledge, to describe the flow regime of a forced flow structure and of a very high heat flux, both of which is expected to be characteristic of vaporizers.

The topical interest of the vaporizers within the BMT 120 KS MGT with angled injection is expected to result in forcing the liquid fuel to flow differently than would be present in steadied conditions. The relatively short length of vaporizers also does not allow for much settling to occur prior to vaporization and ejection into the combustion volume.

### 2.4.4 Heat transfer correlations

Heat transfer of two phase flows is one of the cardinal concerns associated with applications where two phase flows are expected. The reason being that significant variation of the heat transfer occurs as fluids transition from being liquid to gaseous.

Two phase heat transfer correlations are derived using semi-empirical methods based on various theoretical descriptions of the applicable heat transfer mechanisms. These correlations are presented as a superposition, a greater-of-two or an asymptotic account of theorized heat transfer mechanisms. The most widely cited correlations of each of these forms are those by Chen (1966), Shah (1982) and Kandlikar (1990) respectively.

The adequacies of each of these correlations have been observed to vary based on the heat flux (Jung & Radermacher, 1989) and tube diameter (Wambsganss, FranceD.M., Jendrzejczyk, & Tran, 1993). Wattlet (1994) recommended that a greater-of-two model is more accurate than an asymptotic model in prediction of heat transfer in small diameter tubes which have similar dimensions to vaporizers.

The applicability of adapted conventional models have been question by Kattan (1998) as these correlations were developed using vertical flow experimental data and significant differences are observed with horizontal flows. These differences are attributed to the gravitational effects on the flow which act to pool the liquid phase at the bottom due to density variance relative to the gas. This action results in radially varied heat transfer to occur due to the large variation in heat transfer coefficients with respective phases. This occurrence is deemed significant enough (Liu, 2012) to necessitate alternative approaches.

Incorporation of the expected flow regime geometry into the development of simplified heat transfer models have been shown to provide a significant increase in accuracy despite using simple models (Kattan, 1998). Complications in earlier models using this approach during partial dry-out scenarios (Zürcher, Thome, & Favrat, 2000) were addressed by recent contributions by Wojtan (2005). The heat transfer coefficient as developed by Wojtan (2005) is presented in equation 2-14.

$$h_{tp} = \frac{\theta_{dry} h_{dry} + \theta_{wet} h_{wet}}{2\pi} \qquad 2\text{-}14$$

The angular terms present in this model represents the exposure angle of the inner flow perimeter to either liquid or gas interface heat transfer. This both accounts for the large difference in heat transfer coefficients of dissimilar phases and facilitate a reasonable description of the heat transfer interaction occurring during

horizontal two phase flow. A representation of these angles is shown in Figure 2-18 for stratified and annular flows.

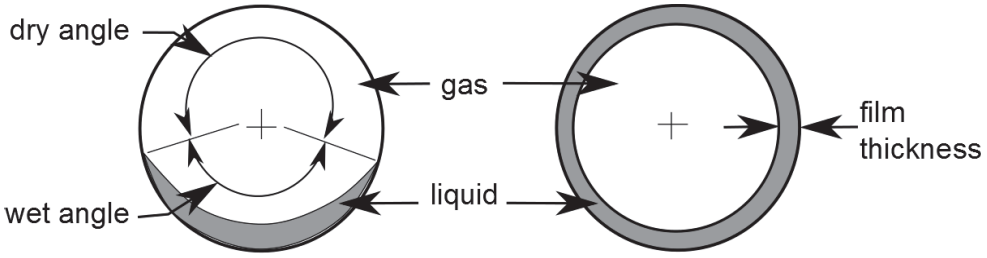


(a) Stratified flow structure (b) Annular flow structure

**Figure 2-18 Simplified model flow representation**

The construction of this heat transfer model is beneficial to the specific analyses of flows through vaporizers. This being because the model can be numerically manipulated into annular or stratified flow behaviour guided by experimental observations. The is achieved by making the stratification angle, $\theta_{dry}$, zero for annular flow or computing it using equation 2-15 (Biberg, 1999) for stratified flow.

$$\theta_{dry} = 2\pi - 2[A - B] \qquad 2\text{-}15$$

With $A$ and $B$ calculated as

$$A = \pi(1-\alpha) + \left(\frac{3\pi}{2}\right)^{1/3}\left[2\alpha - 1 + (1-\alpha)^{1/3} - \alpha^{1/3}\right]$$

$$B = -\frac{1}{200}(1-\alpha)^2\alpha[1 + 4((1-\alpha)^2 + \alpha^2)]$$

The gaseous heat transfer coefficient, $h_{dry}$, is determined from the Dittus-Boelter (1930) correlation for turbulent flows in equation 2-16 using gas properties.

$$h_{dry} = 0.023 Re_H^{0.8} Pr_G^{0.4} k_G d^{-1} \qquad 2\text{-}16$$

The liquid heat transfer coefficient, $h_{wet}$, is determined from a 3rd degree asymptotic model as shown in equation 2-17.

$$h_{wet} = [h_{cb}^3 + h_{nb}^3]^{1/3} \qquad 2\text{-}17$$

Although the accuracy of an asymptotic model has been expressed for conventional homogeneous flow structure approaches (Wattelet, 1994), using the proposed regime dependent flow structure approach is reported to result in improved accuracy nevertheless (Kattan, 1998). The convective and nucleate boiling terms are determined from Dittus-Boelter (1930) correlation for laminar

flows and correlation by Cooper, as proposed by Wojtan (2005), shown in equations 2-18 and 2-19 respectively.

$$h_{cb} = 0.0133 Re_{\delta}^{0.69} Pr_L^{0.4} k_L \delta^{-1} \quad 2\text{-}18$$

$$h_{nb} = 55\, P_r^{0.12} (-\log P_r)^{-0.55} M^{-0.5} q''^{0.67} \quad 2\text{-}19$$

The significant difference in fluid behaviour and characteristics of gaseous and liquid phases necessitate different methods to determine the Reynolds numbers for heat transfer correlations.

The relatively low density of gaseous phases results in producing high void fractions despite moderate mass fraction flow conditions. Complete disregard for the impact of the liquid phase, however, results in degrading model fidelity. For these reasons, the Reynolds number for equation 2-16 is determined as per convention using the tube diameter, but using homogenous fluid properties. This accounts for the liquid's presence, whilst emphasising gaseous characteristics.

The liquid's momentum is contained in the thin film that occurs during either annular or stratified flow. Resultantly, the Reynolds number is determined from conventional relation using the liquid properties and assuming uniform film thickness of the liquid resulting in equation 2-20.

$$Re_{\delta} = \frac{\dot{m}_L \delta}{\mu_L A_L} \approx \frac{2\dot{m}_L}{\mu_L \theta_{wet} d} \quad 2\text{-}20$$

The nucleate boiling correlation by Cooper introduces a reduced pressure term. This pressure represents the ratio of ambient pressure to critical liquid pressure as shown in equation 2-21. The critical pressure of 1800 kPa is recommended for use with the paraffin surrogate, Dodecane (Ambrose & Tsonopoulos, 1995).

$$P_r = \frac{P}{P_{crit}}. \quad 2\text{-}21$$

The heat transfer correlation as presented here represents a collaborative effort to enhance model fidelity as much as possible. Although more detailed models exist, they introduce numerical complexities that cannot yet be tolerated within the limited problem definition.

### 2.4.5 Pressure drop correlations

Vaporization occurring in two phase flows cause a rapid increase of the fluid's momentum due to a decrease in fluid density and the resulting acceleration. This action results in inducing three pressure gradients described in equation 2-10. The current study is, however, limited to horizontal flow and negates the static pressure gradient term.

The momentum pressure gradient is represented by the second term in equation 2-10 and represents the pressure variation resulting from the increase in momentum of the fluid during vaporization. This pressure gradient often embodies the majority of the total pressure gradient. As its form is derived from fundamental dynamics concerning the flow structure, its empirical complexity is limited to the methods used to determine appropriate void and mass fractions.

The frictional pressure gradient term is represented in the fourth term of equation 2-10 and represents the wall shear forces acting on the fluid. The turbulent and irregularly defined nature of two phase flows results in the pure theoretical derivation of this term to be impractical. As such two phase frictional pressure gradient has been the focus of many investigations. The majority of classical empirical frictional pressure correlations were developed using vertical flow data. The most widely cited (Ould Didi, Kattan, & Thome, 2002) frictional pressure drop correlations are those by Lockhart and Martinelli (1949), Chisholm (1973), Friedel (1979) and Muller-Steinhagen and Heck (1986). The review of these methods on experimental data revealed that the correlations by Friedel (1979) and Muller-Steinhagen and Heck (1986) are the best suited for application on horizontal flows (Ould Didi, Kattan, & Thome, 2002). Recent work (Quiben & Thome, 2007) developed a frictional pressure gradient correlation based on a flow regime dependent approach with significant increase in accuracy reported. Frictional pressure gradients are, however, much smaller in magnitude than momentum pressure gradients of boiling two phase flows.

Combustor liner pressure drops of 3% (NATO, 1971, pp. 1-11) and 12% (Gonzalez, Wong, & Armfield, 2007, pp. C-413) are reported for comparatively large and small gas turbines respectively. Because the vaporizers form part of the flow path through the combustor, their operation is also governed by the liner pressure drop.

### 2.4.6 Void factor correlations

The void factor represents the percentage of the total cross sectional area which is occupied by the gaseous phase. Fundamental deduction from mass conservation shown in equation 2-11, the void factor is derived as shown in equation 2-22.

$$\alpha = \left(1 + \frac{\rho_G}{\rho_L}\frac{(1-x)}{x}\frac{v_G}{v_L}\right)^{-1} \qquad 2\text{-}22$$

This correlation for the void factor is very convenient to use, although reported to be inaccurate (Ould Didi, Kattan, & Thome, 2002). The Rouhani-Axelsson drift-flux correlation (1970) is a widely cited alternative with good performance with

use in steam and refrigerant applications (Ould Didi, Kattan, & Thome, 2002). This model and alike, however, make use of empirically adjusted parameters.

The limited data available on paraffin-air in literature, limits the practicality of more complex void factor models in the current study. The model shown in equation 2-22 therefore provides the best option in predicting this parameter.

## 2.5 Vaporization

Vaporization describes the phase change phenomena of a liquid to a gas. This process is required for combustion to enable reactant to progress to plasma. Its importance is emphasized more so within MGTs to promote the reactivity and mixing rate of fuel and air to increase combustion speed. The mechanisms that result in vaporization, how they are employed in vaporizers and methods to manipulate the process are discussed in this section.

### 2.5.1 Vaporization process

Vaporization occurs when the restraining forces on liquid molecules are overpowered by kinetic energy of the particles. Macroscopically this is observed as when the ambient pressure is equalled by the vapour pressure of the liquid.

Vaporization is induced by either reducing the restraining forces resulting from ambient pressure and surface tension or by increasing the vapour pressure with an increase in temperature. Gas turbine applications, however, seldom use pressure reduction methods, apart from flash vaporization, as this leads to increased wear and operational difficulties (Whittle, 1946). Temperature increase is thus the primary method of achieving vaporization in gas turbine engines.

### 2.5.2 Evaporation and boiling

Vaporization occurs when the vapour pressure exceeds the ambient pressure exerted on the liquid. By invoking the mechanisms as previously mentioned, this can occur at the surface or submerged within a liquid volume. Vaporization is generally classified as evaporation and boiling depending on whether its occurrence is at a gas or solid interface respectively.

Evaporation is described as the movement of molecules from the liquid to a gas across the interphasic interface. As seen in Figure 2-19, evaporation is countered by condensation rates. During observed evaporation, the magnitude of actual evaporation is greater than the magnitude of actual condensation.

Boiling mechanisms refer to heat transfer at a solid interface submerged within a liquid. The heat transfer may result in either inducing vaporization within the liquid volume, which is observed as submerged bubbles, or aid evaporation at the gas interface. Two types of boiling are considered for this study relating to the

numerical heat transfer models as previously described. These boiling mechanisms are nucleate and convective boiling as shown in Figure 2-20.

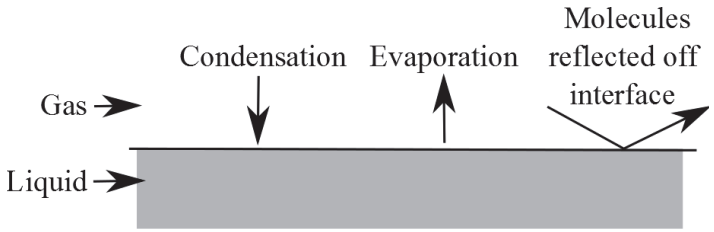


**Figure 2-19 Phase transition at liquid-gas interface**

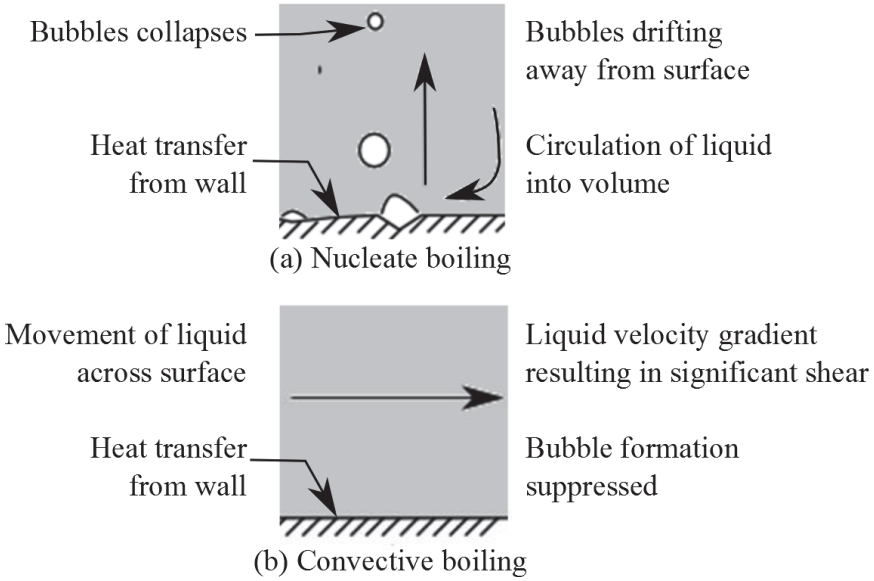


**Figure 2-20 Phase transition at liquid-solid interface**

Nucleate boiling occurs at localized surface imperfections, as shown in Figure 2-20, where heat transfer to the liquid is intensified by the geometry of the imperfection or nucleation site. The increased heat transfer result in vaporization to occur and superheated bubbles to form. The structure of these bubbles is maintained within the nucleation sites, but collapse once heat transfer to the sub-cooled surrounding liquid reduces the vapour's ability to oppose liquid's forces on it. The amount of heat transfer from the bubbles to the liquid is fairly low, but the turbulence invoked by the movement of these bubbles and collapse of them significantly promotes heat transfer.

Convective boiling, illustrated in Figure 2-20, occurs when liquid movement produce a surface boundary layer sufficient to reduce the occurrence of localised areas of superheated liquid. This suppresses the occurrence of nucleation and heat

transfer is achieved by thermal conduction and turbulence. This type of boiling is more efficient than nucleate boiling as thermal conduction away from the heated wall is not restricted by lowered thermal conductivity of vapour bubbles. This reduces localised wall hot spots which decrease thermally induced stresses.

### 2.5.3 Mass transfer models

Vaporization models range in complexity. Simple models are widely used and are based on experimental observations, but lack the detailed definition achieved with more advance models. A discussion of the various models is presented here.

Simple numerical modelling of vaporization and condensation is based on the assumption that phase transition only occur when vapour or liquid volumes are at an experimentally determined saturation temperature and pressure. The amount of energy required for vaporization is termed the latent heat of vaporization and equals the change in internal energy and work performed during expansion of the substance. This model as shown in equation 2-23 is convenient to use, but fails to predict sub-cooled liquid boiling, superheated gas formation and mass diffusion evaporation (Doster, 2006).

$$\dot{m}_{vaporize} = Q_{vaporize}/h_{fg} \qquad 2\text{-}23$$

A more detailed model compared to the previous model can be obtained by microscopic inspection of the vaporization process using particle kinetic theory using a liquid-gas interface as shown in Figure 2-19. The Hertz-Knudsen equation for mass transfer as shown in equation 2-24 and the resulting energy flux term as shown in equation 2-25 follow from fundamental approximations regarding molecular movement across the interface.

$$\dot{m}''_{vaporize} = \frac{1}{\sqrt{2\pi}}\left(\frac{\emptyset_e P_{sat}(T_L)}{\sqrt{RT_L}} - \frac{\emptyset_c P_V}{\sqrt{RT_V}}\right) \qquad 2\text{-}24$$

$$Q'' = \sqrt{2/\pi}\left[P_{sat}(T_L)\sqrt{RT_L} - P_V\sqrt{RT_V}\right] \qquad 2\text{-}25$$

This model assumes that liquid and gas temperatures may be dissimilar and that evaporation may occur below the saturation temperature of the liquid. The complexity of these equations, however, result from the ill-defined evaporation, $\emptyset_e$, and condensation, $\emptyset_c$, coefficients which are not defined for many substances and vary considerably in literature.

An additional modelling approach results in the use of the Sherwood number. This modelling approach relates mass transfer with respect to the Sherwood number in a similar fashion to which heat transfer is related to the Nusselt number. Therefor this modelling approach is popular with concurrent heat and

mass transfer. Its use is, however, limited to low relative mass flux mass transfer (Cengal & Cimbala, 2006, p. 837) and as such this modelling approach is inappropriate for the current study.

Ideally, all liquid should vaporize when moving through a vaporizer. For this case, the macroscopic approach without any supplementary functions should be adequate to describe the phase change process. A more detailed approach which permit an earlier onset of vaporization within a sub cooled liquid would require application of supplementary functions or a microscopic modelling approach. Due to the current uncertainty surrounding the validity of vaporization models applied to the conditions and fluids associated with vaporizers, the model presented in equation 2-23 is used in this study.

## 2.6 Current uncertainty

Limited academic work has been conducted towards the improvement of vaporizer tubes in MGTs. Design and use of vaporizers is left largely to the fabricator's discretion and experience (Englar, 2010). The limited current state of knowledge pertaining particularly to vaporizers comes despite promising results from early research on the technology.

Barnes (1954) provided recommendations to direct further investigations on the subject of vaporizers based on his findings. The most prominent of his recommendations is the isolation of the vaporizer from the combustion chamber. This is argued to result in more simplistic investigations which will yield much more directed insight into vaporizer operational parameters. Based on these recommendations no further research realised into vaporizers to best the author's knowledge. Deducing from recent patents, however, it is presumed that proprietary development had been conducted, albeit not publically available yet.

The processes and mechanisms related to vaporizer operation, as presented in this chapter, have experienced substantial development to promote accuracy and definition. Much of these developments have realised as research into dissimilar fields of interest to vaporizers which is evident from the lack of definition of fuel behaviour with regards to the presented models.

The primary concern with regards to current uncertainty with regards to the aforementioned literature and models is the lack of adequate property models for typically used fluid mixtures and lack of operational guidelines with regards to MGT combustion chambers. As such, much of the analyses presented in this study are conducted based on assumptions motivated by literary accounts with unconfirmed validity on MGT applications.

# 3.
# *Experimental investigation*

The experimental investigations conducted in this study aim to establish operational boundaries based on benchmarked expectations of vaporization performance. The amount of vaporization is considered indicative of vaporizer performance, which is thought to be affected by flow regime. Several flow regimes are identified during experimental investigations and classified according to air and paraffin flow rates. Transitions between flow regimes appear to be influenced by flow rates and injection angle with further investigations resulting in an observed trend between expected annular flow regime and an increase in the amount of vaporization. This section discusses the experimental approaches, information drawn from literature and results, concluding with a review of the experimental procedures and certainty analyses of the measured data.

## 3.1 Experimental definition and considerations

The initial development and experimental rationale are described in this section.

### 3.1.1 Derivation of experimental objectives

The purpose of vaporizers is to facilitate the vaporization of liquid fuel during its movement through the vaporizer. A logical assessment of vaporizer performance is therefore deemed to be a measurement of the amount of vaporization which occurs. However, consideration must also be granted to how experimental data can be transitioned into theoretical analyses, despite this project involving only limited numerical analytics.

From literature it is evident that a cardinal characteristic required for numerical analyses is knowledge about the flow structure during its movement through a body. This information is vital in validating a selection of heat transfer models from those proposed in literature. Classification of the flow structure is usually made based on an experimentally determined flow regime map. No flow map exists to the best of the author's knowledge for the specific flow scenarios applicable to this study and thus the need to develop such a map is the first experimental objective.

Many factors affect the amount of realised vaporization within a combustion chamber and often combustion performance is maintained despite incomplete vaporization (Lefebvre & Ballal, 2010). The measurement of vaporization is thus better directed to observe trends corresponding to vaporization performance rather

than the extent of vaporization itself. Confirmation of a trend relating to flow structure and its influence on vaporization is selected as the second experimental objective.

Experimentally gained knowledge is directed to be applied to the BMT120KS MGT. Therefore similar vaporizer tube geometry and operational conditions are used to direct experimental design and regulation of flow conditions.

The conditions used for the aforementioned investigations concern the flows of air and paraffin. The flow of paraffin and air through the vaporizers within an MGT is governed by a controlled pumping system and the pressure differential arising over the combustor liner respectively. Replication of paraffin flow conditions are readily achieved with a calibrated pumping configuration whereas air flow is more complex. Replication of air flow scenarios by invoking a differential pressure is opposed in favour of the more robust control achieved by forcing a specified air flow through the vaporizer. Use of forced air flow is simpler to establish, is less prone to flow instabilities and results are more widely applicable as vaporizer design may influence actual flow resistance and differential pressure.

### 3.1.2 Measurement parameter selection and injection system design

The two proposed experiments aim to observe flow structures and apparent trends relating to flow structure and vaporization performance with paraffin and air flow rates as control variables. From this brief the following five parameters are identified as being required to define the aforementioned experimental data:

- Paraffin inlet mass flow rate
- Air inlet mass flow rate
- Visual observation of the flow
- Thermal exposure profile
- Vaporization rate

Injected flow rates and the regulatory systems for these flows are important to both experiments and are therefore discussed in this section preceding separate discussions of components developed for each separate experiment.

The paraffin mass flow is calculated from equation 3-1 using depletion volume, depletion time and density measurements.

$$\dot{m}_L = \frac{Vol_L \rho_L}{t_L} \qquad 3\text{-}1$$

The density of the paraffin blend used with tests is measured to be 0.8 g/ml at room temperature. Deviations from this value due to thermal expansion is minimised by maintaining metered liquids near room temperature.

Accurate paraffin flow control is achieved by using a return valve configuration as shown in Figure 3-1. A shutoff valve isolates the system from the supply reservoir at discrete time intervals during which time only paraffin stored in the metering column is pumped towards the injection block.

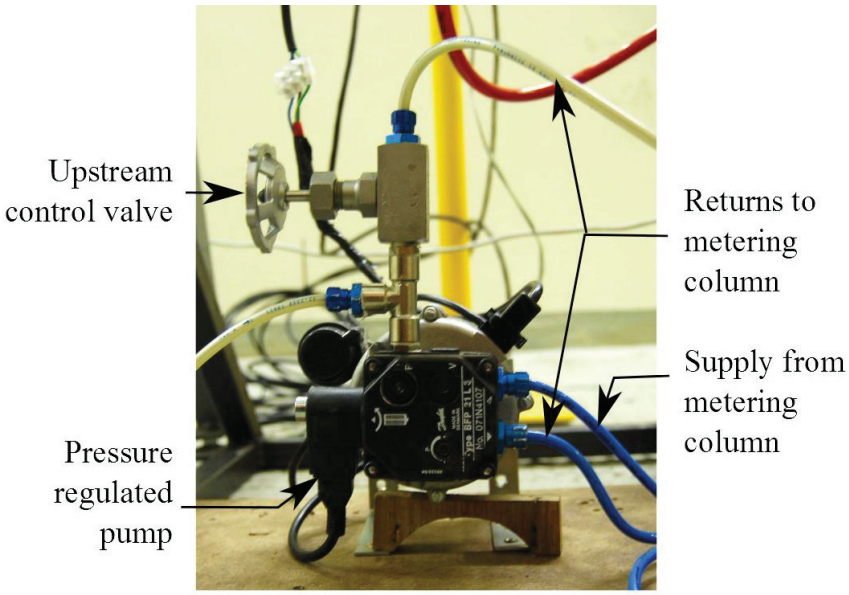


(a) Paraffin pump configuration

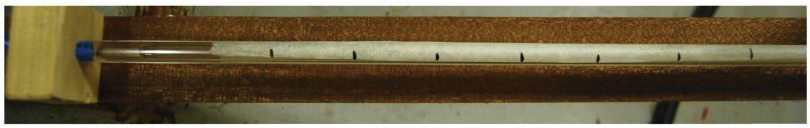

(b) Acrylic metering column

**Figure 3-1 Paraffin flow control and metering components**

Volumetric paraffin flow rate is determined from a measurement of the required depletion time of a metered volume. A transparent metering column as shown in Figure 3-1 is used for this purpose. The column is calibrated to a resolution of 32mm/ml within an accuracy of ± 1% per ml and each metering marker is indicative of a millilitre volume. Additionally, the metering column is orientated horizontally with only a slight inclination angle to reduce the hydrostatic pressure variation of paraffin fed to the pump. The low inclination angle is made possible by the small diameter of the metering column which results in the paraffin's surface tension to maintain a perceived perpendicular meniscus level relative to the metering column's axis.

Depletion time is recorded directly by a portable computer using user guided interaction to indicate each time the liquid's perceived level passes an indicator

along the metering columns length. Multiple measurements are recorded and statistically interpreted to reduce and quantify the error inherent in human reaction present in this measurement. An averaged depletion time is used for volumetric flow rate calculations, providing a variance threshold is met or the measurement is repeated. The amount of samples, predetermined depletion volume and variance threshold is varied according to flow rate which influence depletion velocity and required reaction time.

Air mass flow rate is calculated from equation 3-2 using a volumetric flow rate, absolute pressure and temperature measurements assuming ideal gas behaviour.

$$\dot{m}_A = \dot{Vol}_A \frac{P_{A,abs} M_{air}}{R T_A} \qquad 3\text{-}2$$

A volumetric flow rate measurement is obtained directly from the flow meter shown in Figure 3-2. The temperature and pressure measurements are taken as close as possible to the flow meter to reduce pressure decline and temperature variation to increase accuracy of the compounded mass flow measurement. The placement of these measurements is made upstream of the flow meter to reduce leakage losses with proximity to the volumetric flow meter limited by considerations of imposed turbulence by the thermocouple protrusion into the flow stream. Definition of equation 3-2 is completed by assuming dry air conditions which imply a molar mass of $28.964\ mol/g$.

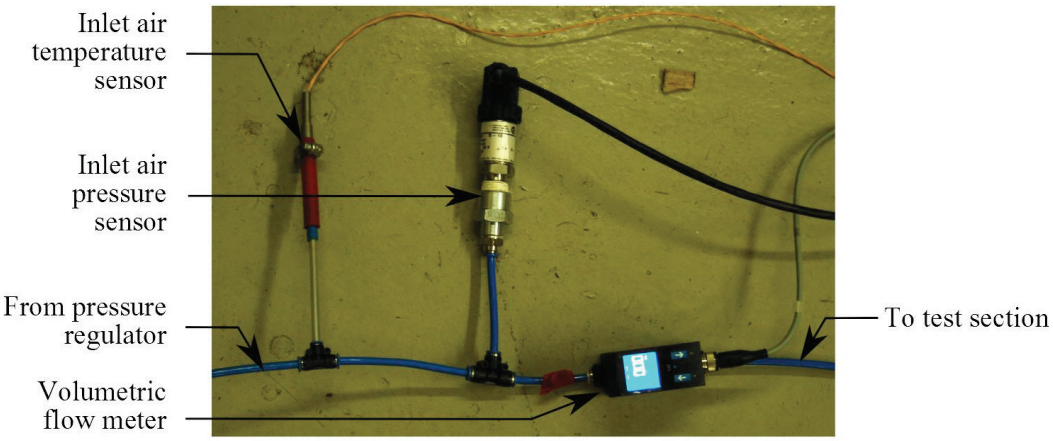


**Figure 3-2 Air flow metering components**

The supply pressure to the measurement cluster is regulated to approximately 6 Bar gauge pressure to minimise pressure induced errors as indicated by manufacture recommendations for the flow meter. As seen in Figure 3-2, all measurements are taken as close to each other as possible with the flow meter being the furthest downstream to negate possible leakages at metering junctions.

The aforementioned components direct measured flow rates towards an injection junction which is configured according to the experimental requirements. These components are integrated into a final injection system along with additional downstream flow control valves as shown in Figure 3-3.

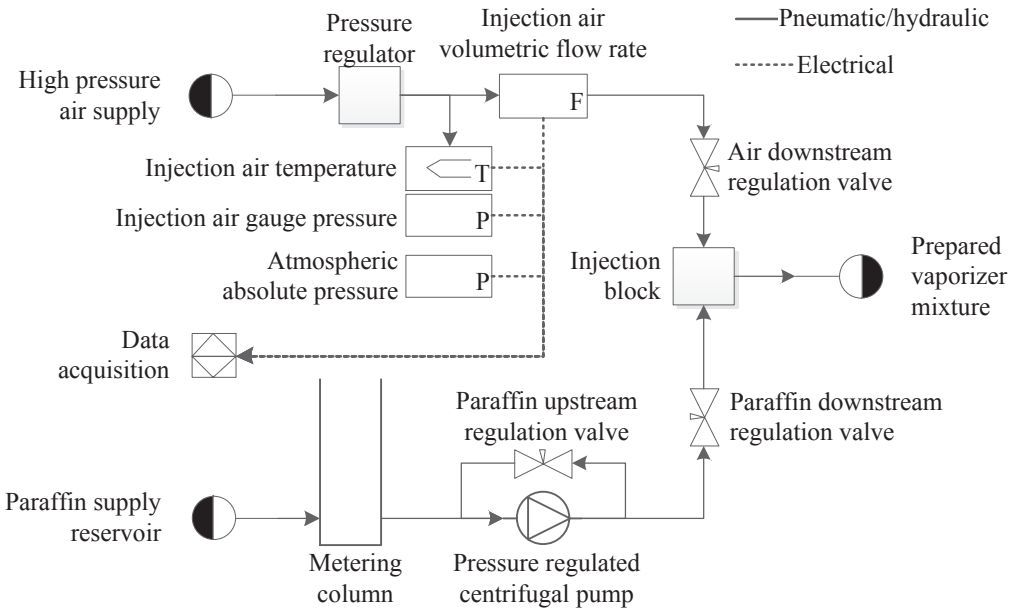


**Figure 3-3 P&ID of injection system used in experiments**

Signal acquisition is accomplished with a National Instruments cDAQ-9184 unit with NI-9213 and NI-9203 modules each relaying thermocouple and current signals respectively. Measurements are processed and presented in real-time using National Instruments Signal Express 2013 (version 7.0.0). The sampling rate on all measurements is set to 1 kHz. Acquired measurement signals are adjusted according to calibration curves as presented in Appendix A and further processed within the Signal Express environment. Post-processing of data is done in Microsoft Excel 2010.

Visual observation, thermal exposure and vaporization rate measurements form cardinal aspects of the two experimental procedures. Thus these measurements are discussed in detail along with their respective experimental setups.

### 3.1.3 Multivariate experimental uncertainty

Accurate measurement of the flow conditions is cardinal to validate confidence in experimental data. The measurement parameters are, however, subject to some degree of uncertainty relating to measurement resolution and variation. An uncertainty analyses is presented pertaining to metered flow rate measurements.

The air mass flow rate is derived from equation 3-2. This measurement's error is deduced by separation of the measured value into an actual and error deviation term as shown in equation 3-3. This equation is simplified using a Taylor expansion resulting in a form as shown in equation 3-4. This function describes the error variance of the air mass flow measurement in terms of individual measurement variations and mean values.

$$(\overline{\dot{m}_A} + \varepsilon_A) = \left(\overline{\dot{V}ol_A} + \varepsilon_{\dot{V}ol}\right) \frac{\left(\overline{P_{A,abs}} + \varepsilon_{Pabs} + \varepsilon_{Pgauge}\right)}{R_{dry\ air}\left(\overline{T_A} + \varepsilon_T\right)} \tag{3-3}$$

$$\varepsilon_A = \varepsilon_{Pabs} \frac{\overline{\dot{V}ol_A}}{R\overline{T_A}} + \varepsilon_{Pgauge} \frac{\overline{\dot{V}ol_A}}{R\overline{T_A}} + \varepsilon_T \frac{\overline{P_{A,abs}}}{R\overline{T_A}^2} + \varepsilon_{\dot{V}ol} \frac{\overline{P_{A,abs}}}{R\overline{T_A}} \tag{3-4}$$

Appling similar treatment to equation 3-1 for paraffin flow rates, equation 3-5 is obtained which indicates the liquid mass flow rate measurement error.

$$\varepsilon_L = \varepsilon_\rho \frac{\overline{Vol_L}}{\overline{t_L}} + \varepsilon_{Vol} \frac{\overline{\rho_L}}{\overline{t_L}} + \varepsilon_t \frac{\overline{Vol_L}\,\overline{\rho_L}}{\overline{t_L}^2} \tag{3-5}$$

The paraffin accumulation rate, which is introduced in a latter description, is computed similarly to the paraffin inlet flow rate, but with different error values.

## 3.2 Flow regime classification experiments

The flow regime classification experiment aim to visually observe and classify the flow within geometry similar to that of the vaporizers found on the BMT 120 KS MGT. Scenarios are quantified relative to air flow rate and in-tube AFR with fuel injection angle providing an additional controlled variance. Flow regimes are classified according to guidelines as presented in Figure 2-17. The obtained data resulted in the successful population of flow maps applicable to 6mm straight through vaporizers with clear regime transitions sensitive to injection angle.

### 3.2.1 Deduction of experimental approach

The aim of this experiment is to populate flow pattern maps for horizontal flows inside vaporizer tubes of 6 mm diameter with injection angle variations. These maps are to be used to estimate the flow regime resulting from flow conditions and better select an appropriate flow structure to base numerical modelling on.

Observed flow regimes are subject to the regulated air and paraffin flow rates. Representation of data and selection of flow rate values are, however, made in terms of air flow rate and AFR as this is found to be more appropriate. Ideally vaporizers are designed to operate on fairly constant AFRs (NREC, 1980). This implies a relatively linear proportionality between fuel and air flow through the combustor which is similar to what is observed from reported operational

conditions on the BMT120KS shown in Figure 2-14. According to assumed uniform flow distribution as mentioned in section 2.4.1, the AFR for the BMT, however, varies between 0.9 and 2.5. This is much lower than recommended AFR bounds for vaporiser flows of between either 3 (Barnes, 1954) or 6 (NREC, 1980) and upper bounds well within the rich extinction limits of the fuel (NREC, 1980).

Air flow rate is selected to describe the alternative control axis. This more easily relates to engine operational conditions and flow split design selection and as such results in making generated data more readily applicable. Additionally, the significantly larger volumetric flow rate versus that measured for paraffin flow reduces overall measurement uncertainty.

Efficient coverage over the entirety of flow ranges is achieved by a systematic measurement approach. The lower and higher limits for air flow rates are selected to be 0.5 and 4.5 g/s respectively based on considerations relating to accuracy and measurement significance. Liquid flow rates were varied to correlate with an upper limit coinciding with an AFR value of 10 and lower limit based on the highest accurately measurable flow rates that can be achieved. Redundant measurements were made near areas of distinguishable flow regime transitions.

Injection of liquid paraffin into the vaporizers of the BMT 120 KS is achieved through the use of hypodermic needles which are declined to the axis of the vaporizer tube. This is shown in Figure 2-13. The declination of the needle with respect to the axis of the tube intends to provoke annular flow and thereby improve surface contact of the liquid fuel to aid heat transfer and vaporization. The sensitivity of flow regime to injection declinations is, however, not defined and thus, variation of injection angle is included as an additional controlled parameter.

### 3.2.2 Experiment design and configuration

The experimental setup to perform flow regime classification experiments is shown in Figure 3-4. Individual component design and selection is prompted by functional requirements and practical considerations.

The test setup is required to assist visual classification of the flow regime during the initial distance where the influence of injection characteristics is prominent. This necessitated the use of an optically transparent test section. An acrylic tube as indicated in Figure 3-5 is selected to best accomplish this requirement. The material properties of acrylic, however, limited the operational test conditions to atmospheric pressures and room temperatures. The tube length is chosen much longer than a typical straight through vaporizer to minimise any influence the outlet may have on the flow.

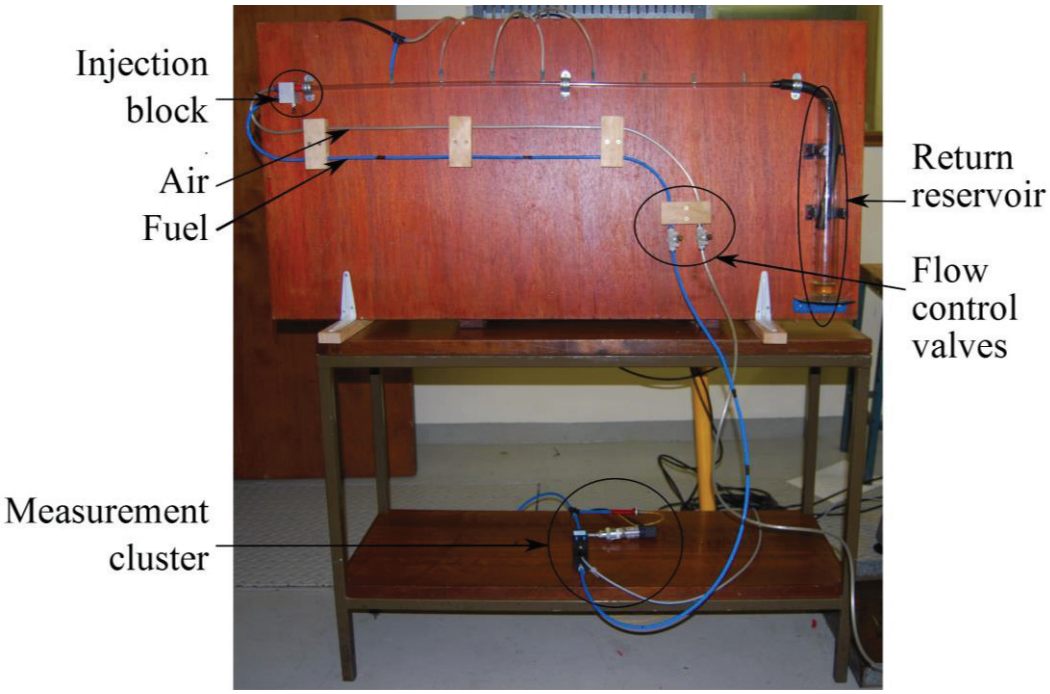


**Figure 3-4 Experimental setup for flow regime classification**

Additionally, the long length allows the flow to attain a steadied condition with reduced influence of injection. Visual observations are made at the inlet and outlet sections of the transparent acrylic test section shown in Figure 3-4. These sections are chosen as they represent the distance of fluid movement associated with significant and negligible injection influence on flow conditions. The observed inlet flow is expected to be dominated by the liquid's injection momentum and thus result in flow structures highly influenced by the injection angle as well as flow conditions. In contrast, the observed flow at the outlet section is expected to be only affected by flow conditions due to diminished momentum transients from injection.

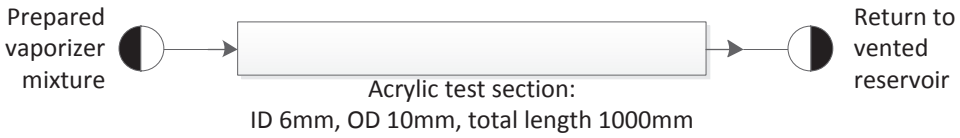


**Figure 3-5 P&ID of flow classification experiment**

Flow conditions are quantified by air and paraffin mass flow rates. These flows are supplied and regulated as previously described and indicated in Figure 3-3. Blue and white supply lines as shown in Figure 3-4 are used to respectively indicate air and paraffin flows.

Replication of the injection conditions and the injection orientation inside the tube during testing is achieved by an injection block. The block allows for the accurate positioning of the fuel injection needle and facilitates secure connection of paraffin and air supply on the test section. The needle orientation protruding from the block, shown in Figure 3-6, is configured to inject liquid at a predetermined angle tangent to the inner tube curvature. The cut away view shown in Figure 3-6 indicates how the flow of paraffin and air is directed from adjacent inlet ports into a singular outlet which connects to the test section. The upper pilot hole seen on the cut-away view is used to secure the test section.

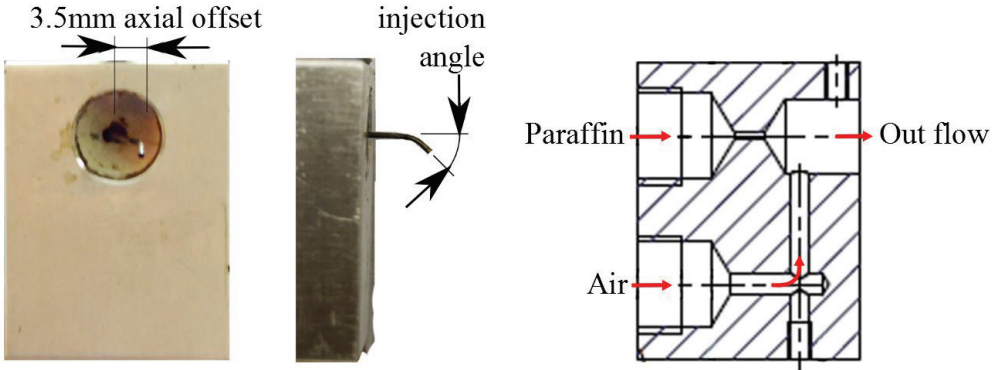


(a) front view (b) partial side view (c) cut away side view

**Figure 3-6 Needle orientation and flow diagram of injection block**

Variations of the injection angle are achieved by manipulating the front tip of the protruding needle injector. The tip is bent to 30, 45 and 60 degree angles with respect to the tubes axis as shown in Figure 3-7.

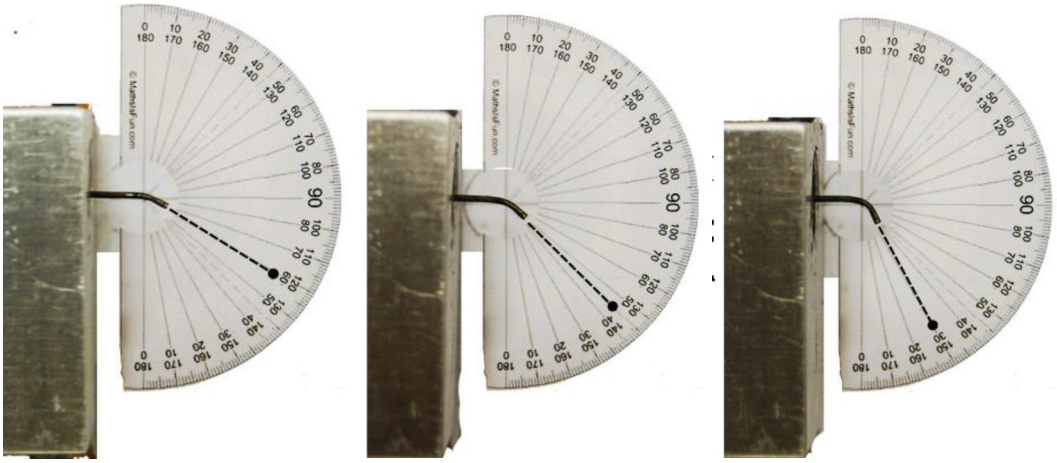

(a) 30 degrees (b) 45 degrees (c) 60 degrees

**Figure 3-7 Varied injection angles**

Observed flow regimes are classified according to those presented in Figure 2-17. The transparencies of air and paraffin, however, result in somewhat ambiguous visual discretion of documented flow structures. A sample and identification guideline is presented in Figure 3-8 for four of the most encountered flow regimes. Intermitted flow is not shown here as it resembles stratified flow, but with clearly distinguishable intermittent slugs that travel along the tube.

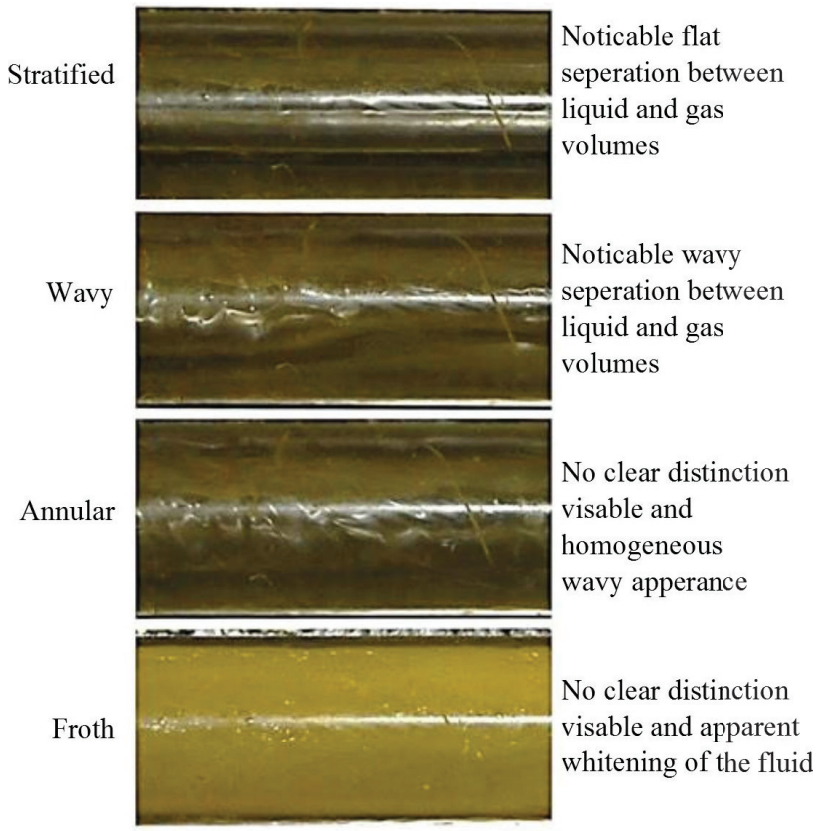


**Figure 3-8 Flow regime classification guideline**

Data is presented in the proceeding section as populated flow maps.

### 3.2.3 Results

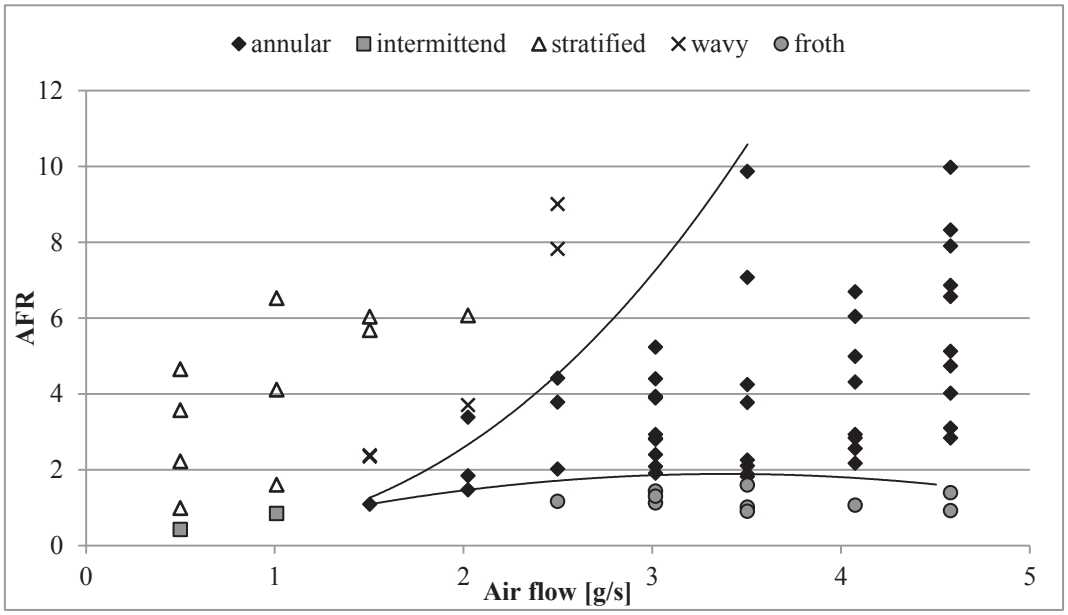


(a) Inlet flow section

Annular flow boundaries:

- With stratified flow: $AFR > 0.4539\dot{m}_{air}^{2.5116}$
- With frothy flow: $AFR < -0.2247\dot{m}_{air}^{2} + 1.5234\dot{m}_{air} - 0.6904$

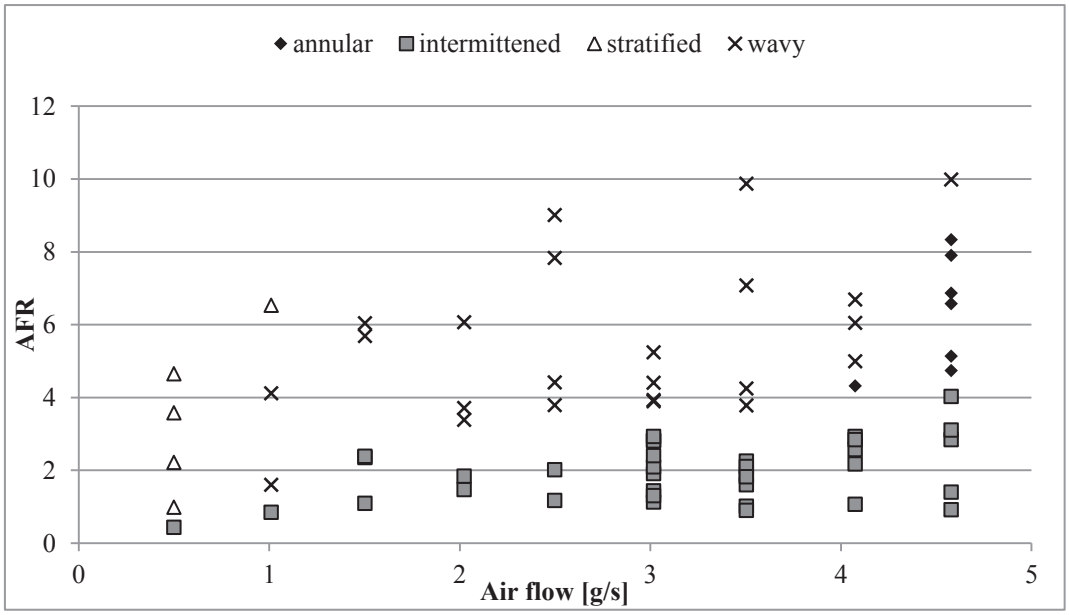


(b) Steadied flow section

**Figure 3-9 Classified flow regimes at 30 degree injection**

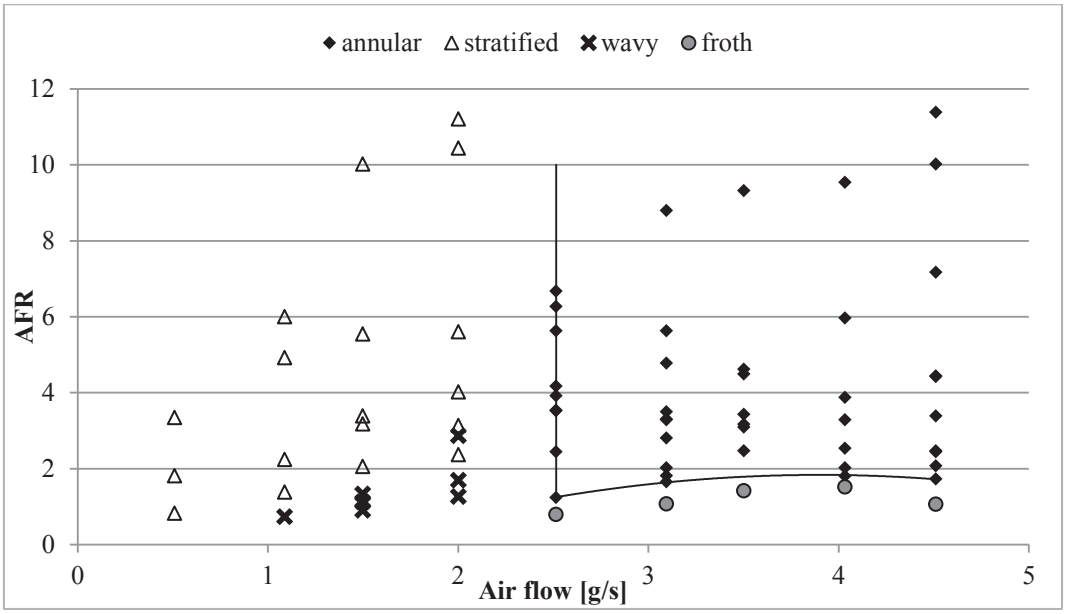


(a) Inlet flow section

Annular flow boundaries:

- With stratified flow: $\dot{m}_{air} < 2.5$
- With frothy flow: $AFR < -0.3059\dot{m}_{air}^2 + 2.3854\dot{m}_{air} - 2.8129$

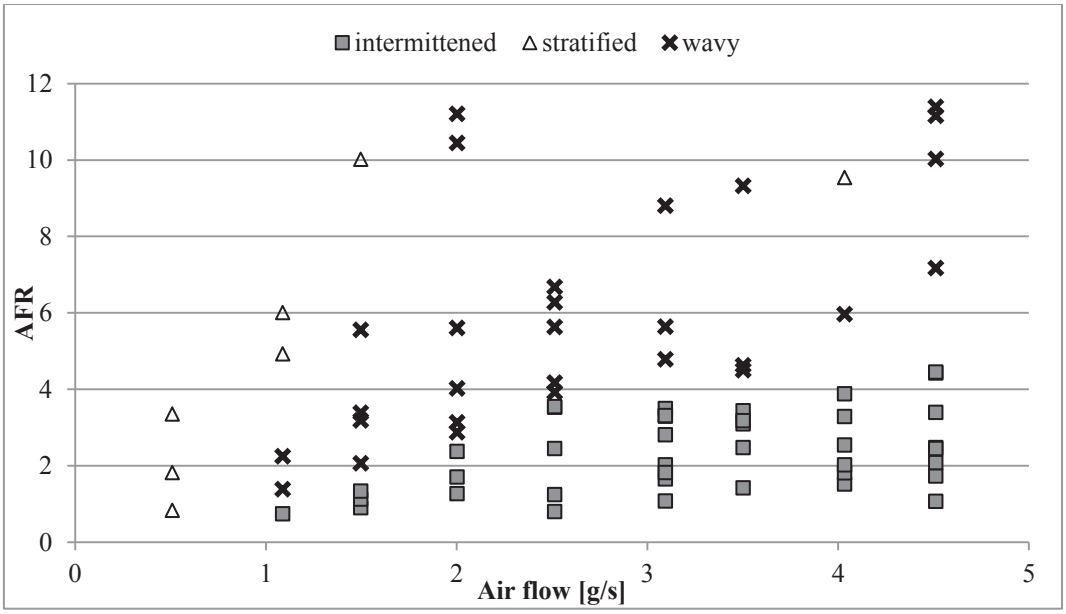


(b) Steadied flow section

**Figure 3-10 Classified flow regimes at 45 degree injection**

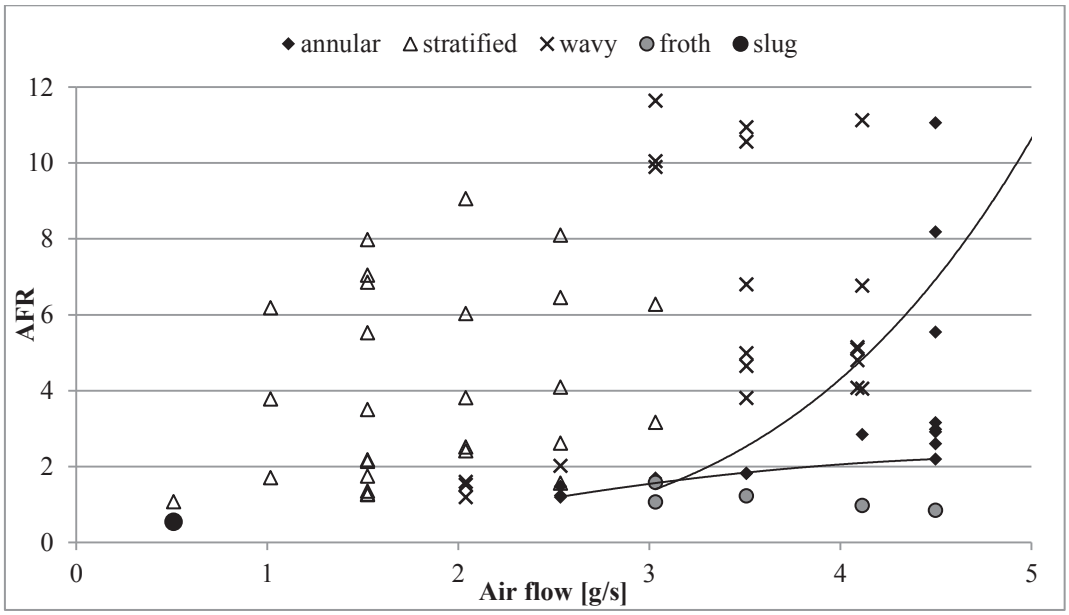


(a) Inlet flow section

Annular flow boundaries:

- With stratified flow: $AFR > 0.0157\dot{m}_{air}^{4.0522}$
- With frothy flow: $AFR < -0.1516\dot{m}_{air}^{2} + 1.5733\dot{m}_{air} - 1.8138$

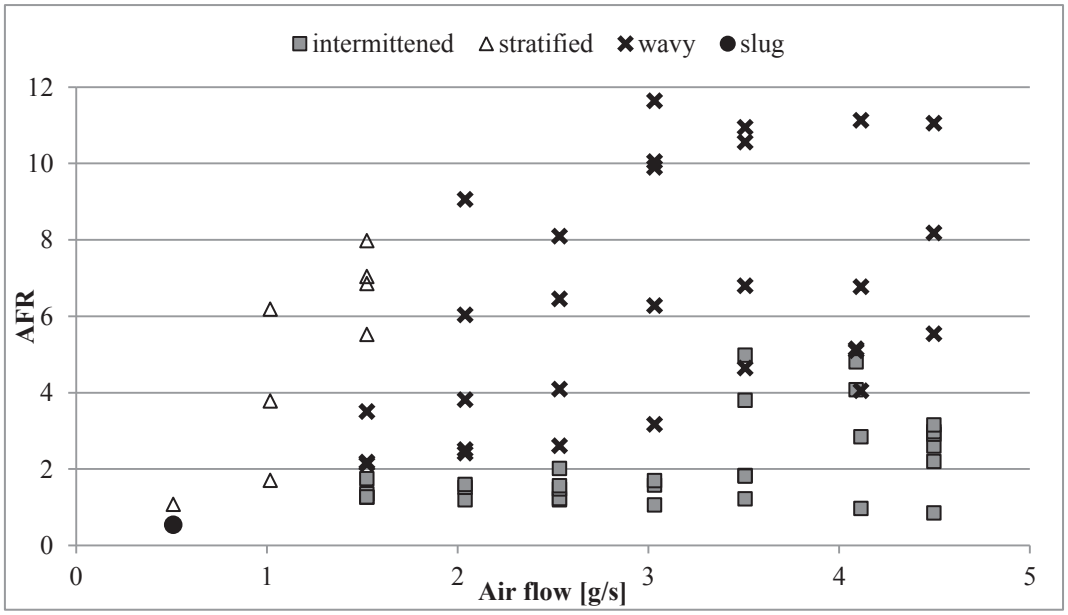


(b) Steadied flow section

**Figure 3-11 Classified flow regimes at 60 degree injection**

### 3.2.4 Discussion

Flow regimes were successfully identified which resulted in the population of relevant flow maps and thereby achieving the experimental objective. Significant influence of injection angle on observed inlet flow structures is noted with less profound effect on outlet flow regimes as expected.

All five flow regimes as presented in Figure 2-17 were encountered, but with the majority of conditions resulting in the four cases presented in Figure 3-8. Despite the apparent discreteness of flow regimes presented in in Figure 3-9, Figure 3-10 and Figure 3-11, actual discretion is observed to be less sudden with a more gradual transition between regimes. This gradual transition is best observed from the observed flows shown in Figure A-3 which show the effect of incrementally increased flow rates on flow structure for all three injection angles.

Flow structures are observed to be sensitive to the injection angle seen from the populated flow maps and more directly in Figure A-3. A reduction in the injection angle resulted in a wider occurrence of frothy flow as seen in Figure 3-9 and Figure A-3. The frothy flow produced with this injection angle also appears to be more aggressive compared to other injection angles during comparison of the highest flow conditions shown in Figure A-3. In contrast, the opposite is observed to be evident with an increase in the injection angle. The high injection angle appears to suppress the influence of liquid injection based on the similarity of inlet and downstream flow classifications presented in Figure 3-11. This is presumably due to less axial momentum being imparted to the injected paraffin as the injection angle increases. The lowered axial and increased radial velocity of the liquid with this adaption results in increasing the interphasic velocity gradient and resulting interphasic shear. This is reasoned to be the cause of the more rapid coalescence of fluid behaviour as deduced from the lowered and higher shifted regime boundaries apparent for the 60 degree injection shown in Figure 3-11 as opposed to the other investigated injection angles.

The transition boundary between frothy and annular flow appears to have a parabolic form and only occurring up to and including a maximum AFR value of approximately 2 for all injection angles. This observation is speculated to be one of the reasons supporting the operational recommendations from literature to remain above AFR of 3 (Barnes, 1954) or 6 (NREC, 1980). This speculation is addressed further during the vaporization experiments.

The similarity of steadied flow observations as presented in Figure 3-9, Figure 3-10 and Figure 3-11 contributes to the confidence of achieved experimental repeatability which is indicative of the accuracy of the measurement procedure.

## 3.3 Vaporization performance measurement

The performance of a vaporizer is reasoned to be logically quantified as the amount of vaporization that occurs for a given flow scenario. The flow structure to two-phase flows apparent in vaporizers is indicated to have a profound influence on heat transfer of two phase flows (Wojtan, Ursenbacher, & Thome, 2005). Building on the results obtained from the aforementioned experiment, the following experiment aims to investigate the relationship between flow structure and amount of vaporization. Using the resulting flow maps of the previous investigation, specific flow conditions and test setup is chosen to best simulate operational scenarios and achieve experimental objectives. The resulting measurements presented a definite trend indicative of a relationship between flow regime and vaporization performance.

### 3.3.1 Experimental rationale

The objective of this experiment is to identify and qualitatively determine the severity of a trend relating vaporization performance to flow structure. This is achieved by replicating a thermal exposure scenario as expected within a combustion chamber and using established flow maps to indicate flow behaviour within the test section.

Quantifying vaporization performance is subject to the design requirements and tolerances of the combustor. Previous experimental investigations by Barnes (1954) and Jasuja (1987) were primarily concerned with assessing the spray characteristics of vaporizers and as such measured the emitted droplets. These studies were, however, directed at larger combustors where incomplete vaporization can be tolerated (Lefebvre & Ballal, 2010). In contrast, MGTs do not have the needed combustor length to tolerate incomplete vaporization which consequently leads to combustion inefficiencies. Qualification of vaporizer performance for this study is therefore based on the quantitative measurement of the amount of vaporization that occurs. Furthermore, as this experiment intends to qualify trends rather than validate design, flow conditions and thermal exposure are selected to suit operational concerns and maximise measurement accuracy.

The thermal exposure profile within a combustion chamber is characterised for the purpose of this study by the form and magnitude of the temperature profile along the vaporizer's axis. Regulation, safety and practicality are the primary factors considered during the design of the thermal exposure equipment.

Replication of actual operational conditions necessitated the use of a combustion type heat source. Thermal regulation of a combustion heat source is achieved by controlling the combustion stoichiometry and this is done by varying the amount of fuel and air. Conventional experiments of vaporizers often reintroduced the

vaporized fuel to assist combustion, but this leads to sensitivity in regulating the combustion conditions (Barnes, 1954). It is decided to use a regulated auxiliary fuel source and isolate the flow through the vaporizer within a separate flow cycle.

Flame proximity to fuel carrying conduits was a large practical and safety concern in the design of an appropriate burner. A baffle body burner was considered due to its flame anchoring characteristics (Lefebvre & Ballal, 2010), but prototypes proved to result in significant back flow of the flame as shown in Figure 3-12 and high thermal exposure to the injection manifold. An alternative concept was developed based on the operational mechanism of a Bunsen burner whereby a venturi effect is created by the high velocity injection of fuel into a projection tube. A prototype shown in Figure 3-12 using this configuration is observed to result in a very stable, repeatable and projected flame which considerably reduces thermal exposure to supply components. This concept is chosen to be further developed.

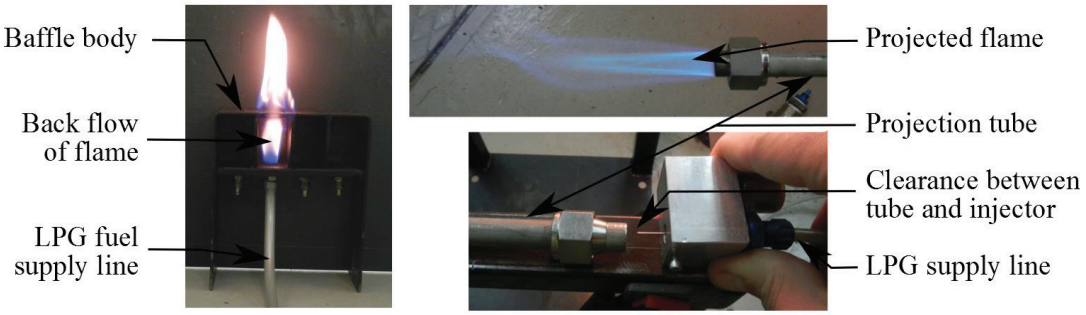


**Figure 3-12 Burner prototypes**

The vapour quality of the flow within vaporizer and test section is expected to increase as vaporization occurs. The flow in conventional flow scenarios transitions to a more gaseous mixture until complete dry out occurs as shown in Figure 3-13. Liquid injection is believed to force the flow into flow structures as observed during the aforementioned experiment. The increase in vapour quality, however, also is expected to influence the experienced flow structure. Despite these concerns, the opaqueness of paraffin vapour and combustion temperatures limits practical alternatives. Therefore flow maps as developed during non-vaporizing conditions are the best tool to guide flow structure expectations.

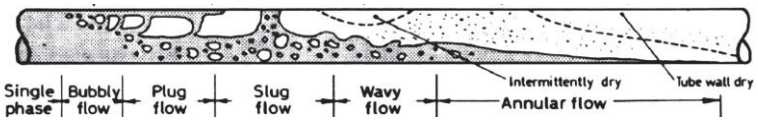


**Figure 3-13 Flow regime transition during horizontal two phase flow boiling**

(Adapted from (Thome, 2005))

The injection angle is observed to influence the resulting flow structure significantly. From the populated flow regime maps presented in Figure 3-9, Figure 3-10 and Figure 3-11 for the various injection angles, the largest occurrence of annular flow is observed to occur with a 45 degree injection angle. As such this injection angle is used to maximise the probability of resulting in annular flow. Indication of constant paraffin injection rates on the flow map shown in Figure 3-10 for this injection angle is shown in Figure 3-14.

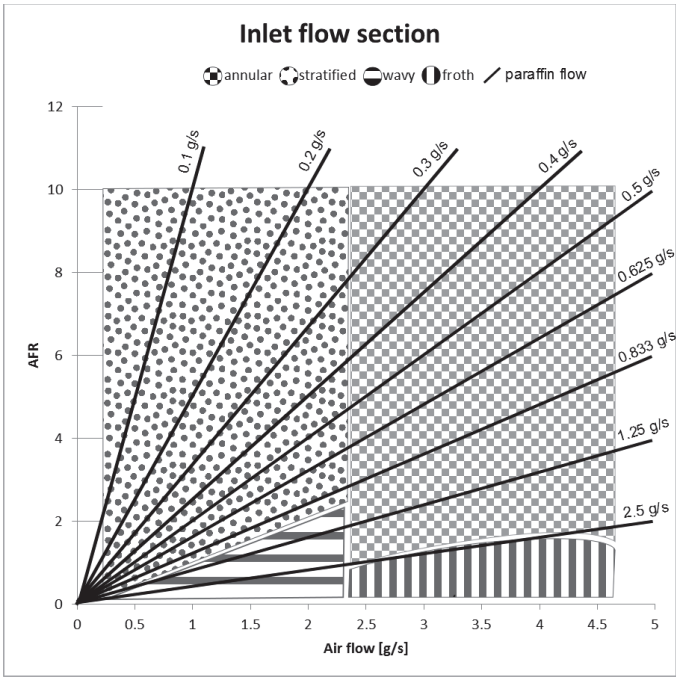


**Figure 3-14 Adapted inlet flow map for 45 degree injection**

Transitions across the flow map presented in Figure 3-14 can be achieved in one of three ways: vertical, horizontal or along lines of constant paraffin injection rates. Vertical transition requires flow to transition through frothy flow. The high flow rates and increased turbulence of this flow regime, increases measurement difficulty which contributes to inaccuracies. Furthermore, although a horizontal transition would best represent replication of indicated operational modes, the variance in liquid flow rate and the measurement methodology used would result in a large variance of required measurement resolution to maintain accuracy which is not practical. By elimination, the transition along a line of constant paraffin injection rate is selected.

The paraffin injection rate is chosen based on interpretation of Figure 3-14 and recommended operational conditions for vaporizers. As can be seen from this illustration, paraffin flow needs to be greater than 0.234 g/s and less than 2.5 g/s to ensure transition into annular flow whilst mitigating pure stratified flow and

frothy flow respectively. A flow rate of approximately 0.5 g/s maximises flow condition possibilities and thus is selected as the desired flow rate.

### 3.3.2 Experimental design and configuration

Vaporization performance experiments aim to measure the amount of vaporization occurring within 6mm ID Inconel vaporizer tube exposed to a simulated combustion scenario. These measurements are acquired from the test setup illustrated in Figure 3-15.

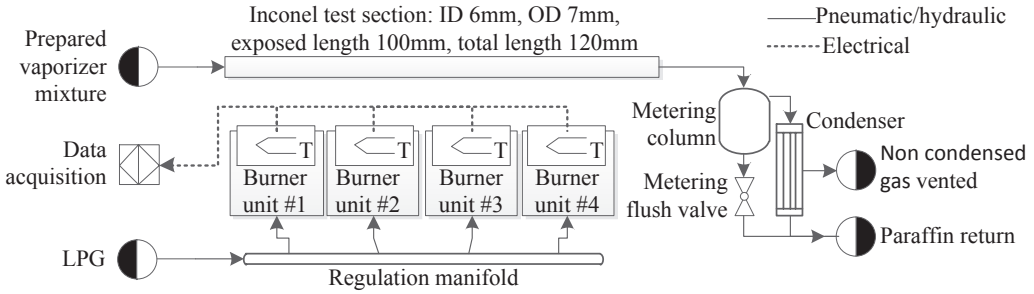


**Figure 3-15 P&ID of vaporization experiment**

Design, manufacture and selection of components required for the design shown in Figure 3-15 are based on functional requirements and practical considerations related to achieving the proposed objectives. The final form of the experimental setup illustrated above is shown in Figure 3-16. The orientation of the test section as presented is such that the Inconel test section is exposed to the emitting flame for the bottom and exhaust gasses are drawn from the top.

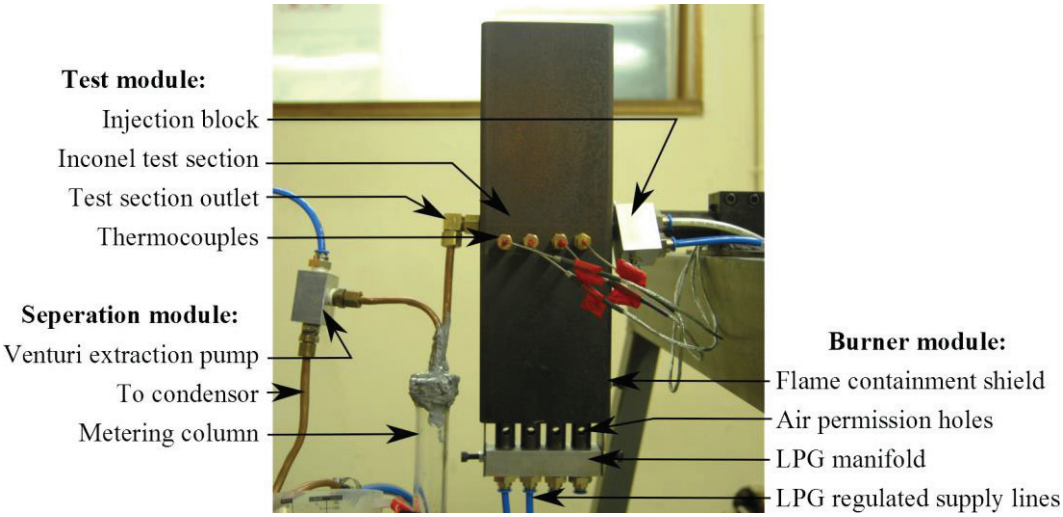


**Figure 3-16 Experimental setup for vaporizing flow**

The main components of the vaporizing test setup are the test module, burner module and separation module as indicated in Figure 3-16. The burner section uses adapted Bunsen burner design to produce a controllable pre-mixed high temperature flame. Additionally developed components include the injection block and post-vaporization separation and metering section.

The Inconel test section is 100 mm long and of similar surface finish, wall thickness and diameter than the vaporizers installed in the BMT 120 KS MGT. The tube is held in position by placement holes on either side of the flame shield wall and secured by compression fitted outlet and transition fit inlet fittings.

The thermal exposure profile is achieved with the use of a four burner apparatus which can be seen installed within a flame containment shield in Figure 3-17.

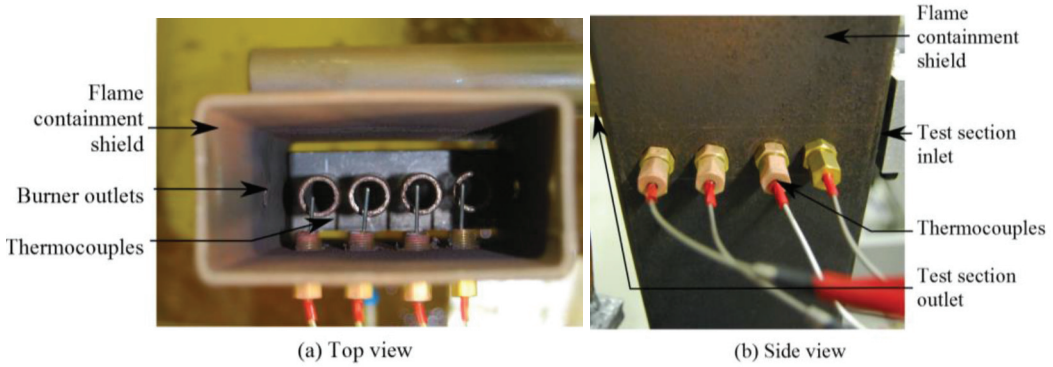


**Figure 3-17 Four segment burner unit**

The burner apparatus is designed to use venturi suction to draw in atmospheric air similar to a Bunsen burner and then project a premixed flame at the outlet of the tube. This ensured both improved safety and repeatability of combustion as well as providing dual flame control by means of air and LPG regulation.

The thermal exposure of this burner unit is quantified by four thermocouple measurements of the gas temperature above the burner outlets, directly below the test section as shown in Figure 3-17. Unshielded K-type thermocouples within a 1mm polished stainless steel sheath are used, despite recommendations regarding the accuracy of these values at the expected exposure temperatures (Van der Merwe, 2014). The constricted area between the burner outlets and the test section, however, limited the practicality of using conventional thermocouple shielding. Following recommendations by Shannon and Butler (2003) the measurement error due to thermal radiation and conduction is reduced as much as possible by selecting thermocouples as small as possible and ensuring a polished finish before experiments. The thermocouples are fixed in the flame containment shield at positions corresponding to 12.5mm, 37.5mm, 62.5mm and 87.5mm from the internal wall at the injection side of the flame shield.

Flow emitted from the test section is processed through a separation module as shown in Figure 3-18. This module is designed to reduce the amount of vapour condensation and liquid entrapment of exhaust air by separation of the two phases as soon as possible after expulsion from the test section.

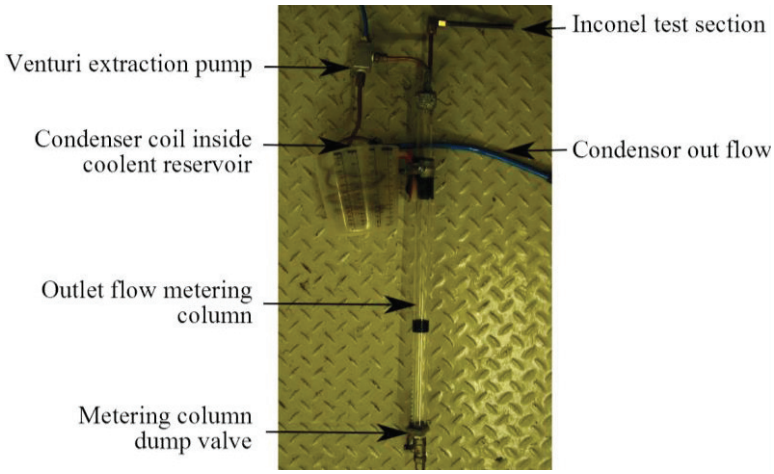


**Figure 3-18 Vaporization performance experiment separation module**

The vaporization rate is measured. The vaporization rate is determined as the difference of measured injection and accumulation rates of liquid paraffin. The accumulation rate is calculated from the required time to fill a predetermined volume within a metering column. The volume measurement is made using the metering column as shown in Figure 3-18 and filling time is recorded with the user guided timing programme described in section 3.1.2. The metering column is calibrated to a resolution of 4mm/ml within an accuracy of ± 1% per ml.

Extraction of vapour and air through a condenser is assisted by a venturi suction pump as indicated in Figure 3-18. This accompanied with the reduced distance between test outlet and gas-liquid separation limited the amount of condensate within the metering column and recuperated much of the vaporized paraffin.

Periodic return of accumulated paraffin and condensate ensured continuous testing to be conducted. This eliminated transients in the behaviour of the experimental setup caused by heating up of components.

The paraffin and air injection system is used as described in section 3.1.2, but with a slightly reduced test section mounting hole for the injection block.

The experimental procedure as previously described is conducted as the primary investigation of this experiment. Interest in how the flow responds to other flow structures and thermal exposure variations, however, prompted an additional set of test conditions to be evaluated. Measurements are summarised in Table A-3 found in Appendix A.

### 3.3.3 Results

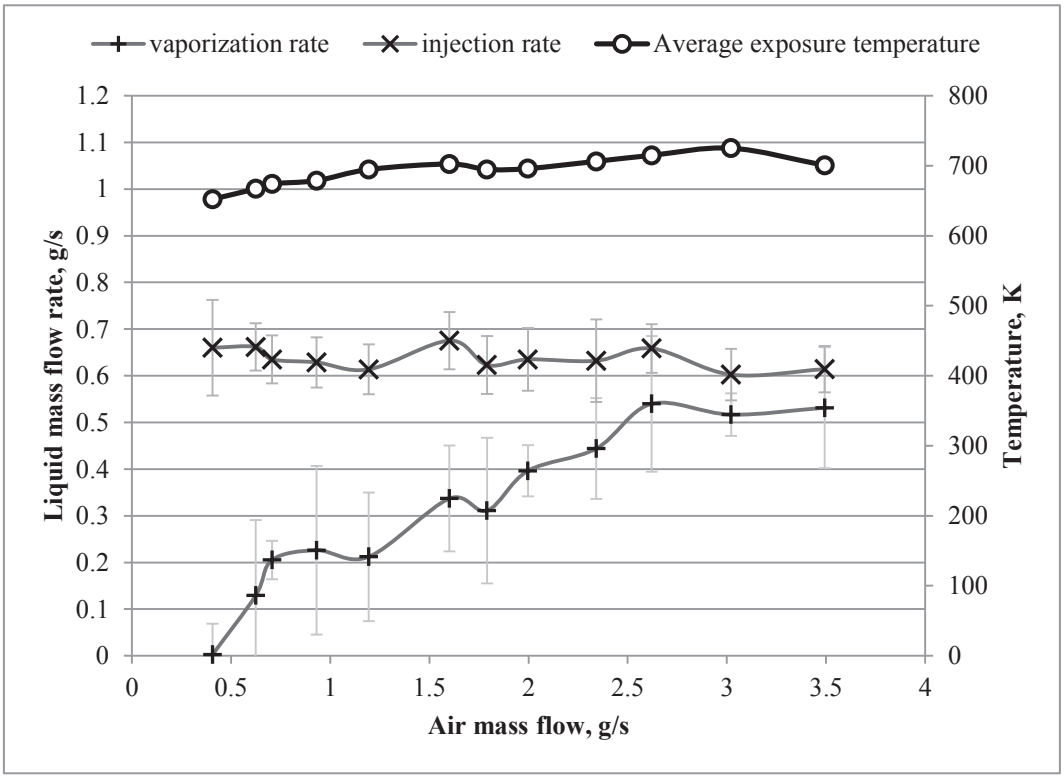


**Figure 3-19 Flow regime tests: Measured vaporization rates**

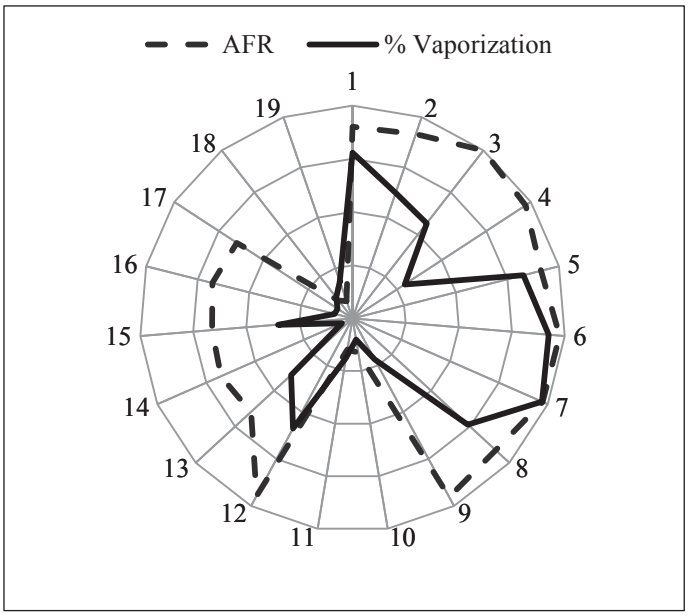


(a) AFR vs. Vaporization

**Figure 3-20 Normalised and scaled parameter and vaporization comparisons**

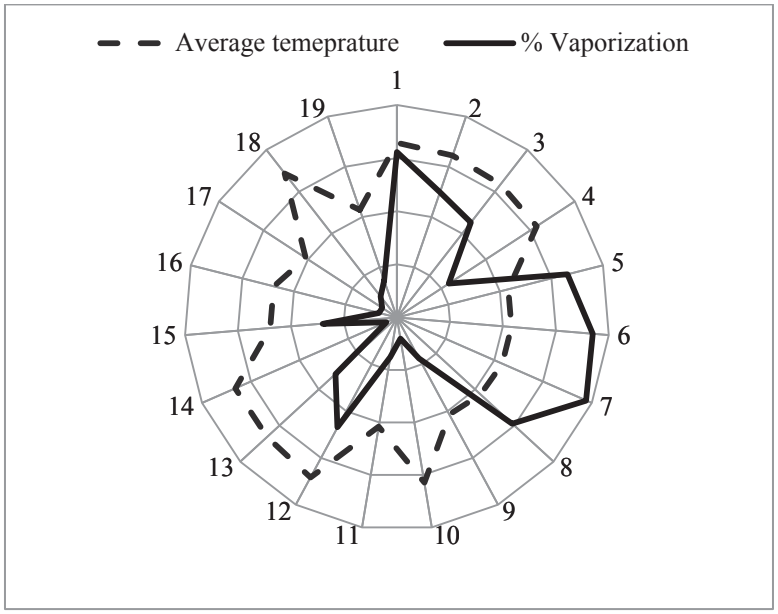


(b) Average temperature vs. Vaporization

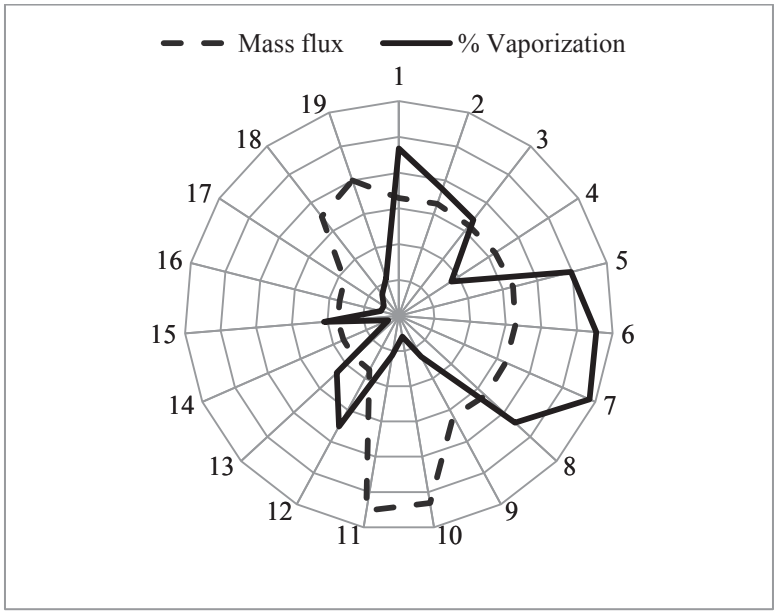


(c) Mass flux vs. Vaporization

**Figure 3-20 Normalised and scaled parameter and vaporization**

### 3.3.4 Discussion

The vaporization performance experiments investigated the dependency of vaporization on flow regime. The investigation led to the design and commissioning of a vaporizer test bench which is used with success to measure and observe vaporization performance.

The experimental method and setup used with this experiment proved to be readily manufactured, controlled and adapted to fit evolving requirements. The robustness of measurement design and decision to limit investigation to a single vaporizer configuration improved measurement confidence and negated much complexity anticipated with irregular distribution through the fuel ring visible in Figure 2-10. Although the experimental setup is designed to be able to rotate and provide alternative exposure orientations, time limited investigations to the single orientation as presented in Figure 3-16. During annular flow, the movement of paraffin is expected to result in indifferent results; however, stratified flow may exhibit varying behaviour dependent on heat source orientation.

The flow maps derived from visual observations proved to be a pivotal part in directing experimental design. The flow maps derived from experiments allowed for better estimation of the flow conditions required to obtain vaporization and adapt the measurement equipment accordingly. Transition between flow regimes is achieved by varying the air flow rate whilst maintaining an approximately constant liquid flow rate as indicated in Figure A-1. The measured amounts of vaporization indicated in Figure 3-19 indicate a trend towards the improvement of vaporization as flow transition towards a higher air flow rate. Assuming behaviour as indicated by the flow maps to be representative of that experienced within the test section, this increase in vaporization can be attributed to a transition to annular flow. This is further supported by observations that linked AFR to vaporization as seen in Figure 3-20, but noting that an additional factor must be attributed for the significant increase in vaporization between test cases B1-9 and B12-17.

Experimentation was performed on a representation of a single vaporizer with four separately controlled Bunsen burners projecting a flame perpendicular to the tube as external heat sources. This differs from the in-situ flame exposure which proceeds parallel to the axis of the vaporizer towards the rear of the combustor. The difference in the exposure profile of these two configurations undoubtedly influences the thermal energy transfer profile of the tube. This is, however, not expected to negate observed trends, but merely shift vaporization performance accordingly.

Possible factors that affect the vaporization measurement technique are droplet entrainment and condensation. The magnitude of influence these factors have, however, is impractical to determine on the current experimental configuration due to the low flow rates and turbulent nature of vaporizing two phase flow. Design of the test equipment is such to reduce these effects, but a degree of uncertainty is inevitable.

As literature suggests annular flow exhibit superior heat transfer due to increased liquid contact with the heated surface which should result in increased vaporization rates. Furthermore, the thinning of the annular liquid film suppresses nucleate boiling which leads to convective boiling to be the dominant heat transfer mechanism as the vapour quality increases. The suppression of gas bubbles forming near the wall-liquid interface apparent with nucleate boiling, results in convective boiling transferring heat more effectively. This is due to the gas bubbles having greatly reduced thermal conductivity than the liquid. On the other spectrum, observed frothy flow enforces bubble entrainment which is expected to result in lowered heat transfer rates.

During measurements it is assumed that density of the paraffin liquid remain constant. The thermal expansion of paraffin liquid, however, results in varying the density of the liquid such that conversion of volumetric to mass measurements becomes compromised. It is estimated from property reference literature that the volumetric measurement error range up to 4.3% at 60 degrees Celsius as compared to the reference value measured at 20 degrees Celsius.

Flow rate measurement deviations indicated on Figure 3-19 and Figure 3-20 are observed to 14.35% and 20.84% for the air and paraffin flows respectively. This is cause for concern, but further analyses are required to determine the best approach in addressing these tolerances.

## 3.4 Measurement certainty analysis

Air and paraffin flow uncertainty is estimated using tolerance values from equipment literature and statistical analyses of measurement data. Using equations 3-4 and 3-5 the value tolerance as indicated on Figure 3-19 and Figure 3-20 is calculated for each individual measurement. These tolerance values are incorporated into overall uncertainty parameter as indicated by equations 3-6 for each of the three flow rate measurement.

$$u_i = \sqrt{var(\varepsilon_i)} \qquad 3\text{-}6$$

Uncertainties of 0.0348 g/s, 0.0490 g/s and 0.0590 g/s are calculated for the air mass flow, paraffin mass flow and paraffin accumulation rate measurements

respectively. Based on the error functions shown in equations 3-6 the average estimated relative contribution made to each of the measurements have been quantified in the Pareto diagrams as shown in Figure 3-21.

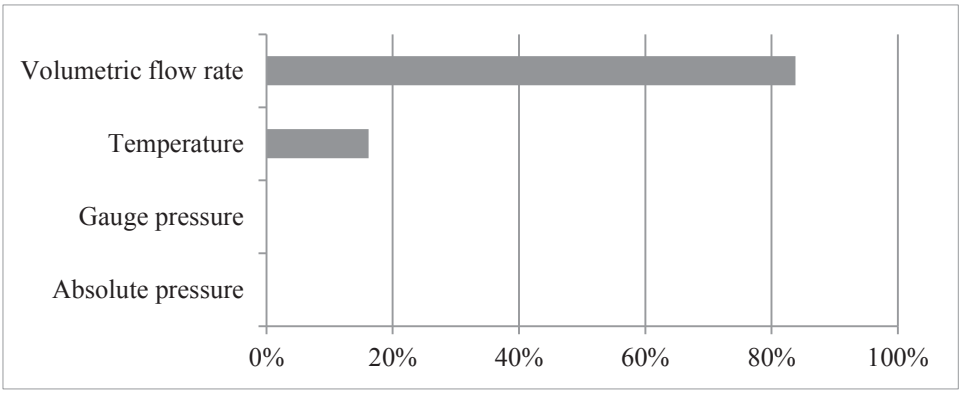


(a) Air injection rate measurement

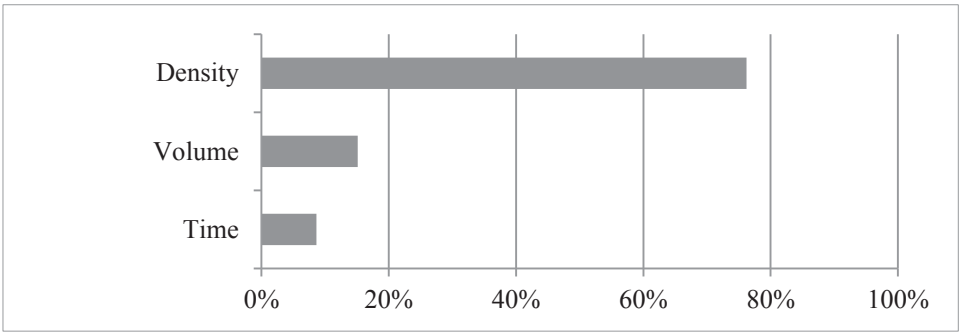


(b) Paraffin injection rate measurement

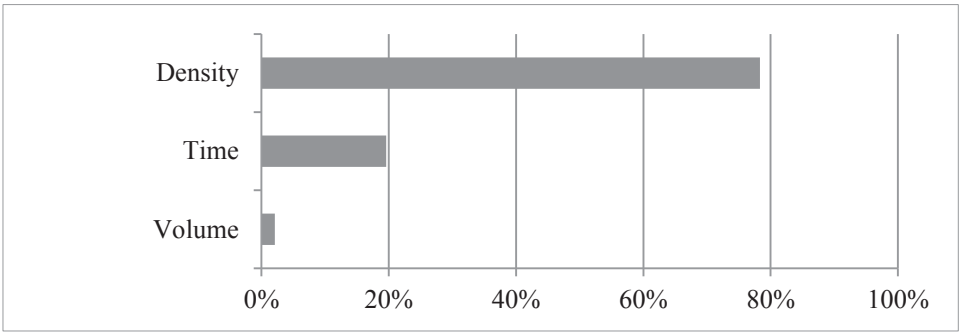


(c) Paraffin accumulation rate measurement

**Figure 3-21 Pareto diagrams of relative error contribution in measurements**

From Figure 3-21 it is evident that the volumetric flow rate measurement and constant density assumption are responsible for the majority of incurred error. The relative contributions of other measurement errors are all less than 20%. Endeavours to reduce the associated errors are thus best directed towards improving certainty of these measurement parameters.

# 4.
# *Numerical investigation*

The numerical model is developed as a sample approach to investigate the applied use of theoretical models to investigate flow through a vaporizer. This investigation is therefore not intended to be used in validating predictions, but rather explore the limits and behaviour of proposed models, assumptions and parameter variations. Model development is based on a flow structure approach as presented by Wojtan (2005) and experimental results are used to amend experimental parameters accordingly. Numerical analyses are conducted with regards to key parameters and the variances are noted.

## 4.1 Numerical model development

The development of the numerical model is presented in this section.

### 4.1.1 Discretization and computational algorithm

The numerical approach is limited to a steady state one-dimensional model. This is deemed sufficient for the purpose of the intended numerical investigations and comparable to conventional two phase flow treatments. The one dimensional numerical model is based on a simplified geometric representation shown in Figure 4-1 of a vaporizer exposed to combustor and test conditions.

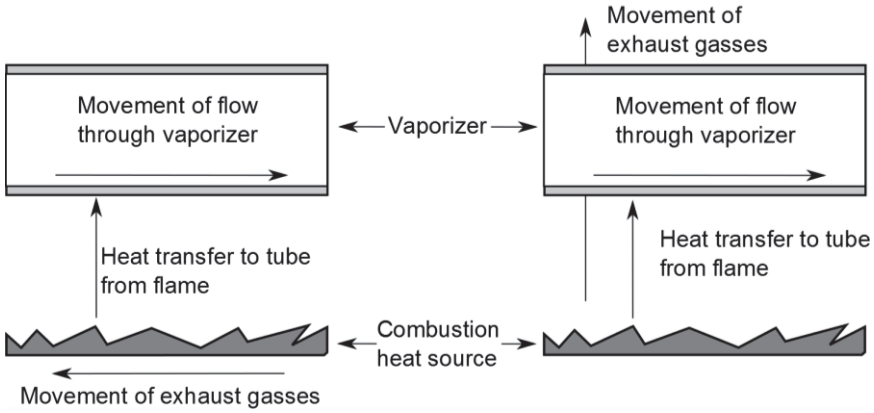


(a) in combustor (b) in test configuration

**Figure 4-1 Simplified representations of vaporizer flow conditions**

The main difference between these configurations is the movement of external gasses relative to the vaporizer either perpendicularly or parallel as indicated. Adaptation of the external convective heat transfer coefficient can therefore be adjusted accordingly to fit either configuration.

The simplified representation is discretized into one-dimensional elements as shown in Figure 4-2. Two phase conservation laws as presented in equations 2-11, 2-12 and 2-13 are applied to the interior flow of the element.

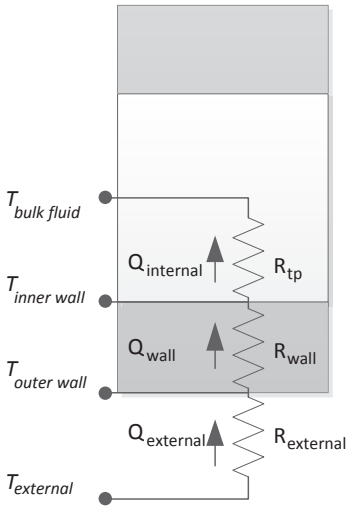


**Figure 4-2 One dimensional thermal resistance diagram**

The one-dimensional heat transfer model is computed from a thermal resistance diagram as shown in Figure 4-2. As seen from this diagram, the resistance to heat transfer is treated as three resistances each encompassing the external, wall and internal heat transfer rates respectively.

A forward marching computational scheme is applied to this model. Upstream interior flow conditions are used as input parameters and downstream flow conditions are concurrently calculated along with thermal energy transfer balancing to obtain a solution. Once convergence is met, the process is repeated for the next element until all elements defining the computational domain have been stepped through. The algorithm for this implicit calculation methodology is shown in Figure 4-3.

The advantage of this numerical scheme is the ease and simplicity by which it is implemented. Although inherently stable due to the fixed inlet flow property and exterior temperature values, a higher order quasi-transient adaptation to implicit parameter calculation can be done easily owing to the orderly format of this algorithm. The disadvantage to this computational scheme, however, arises from the forward marching methodology which negates downstream feedback to upstream calculations and carries imposed errors along up to completion. Discretization independence and logical qualifiers are used in this study to reduce observed errors from computational shortfalls.

A set of initial conditions are required to start the computational flow. The initialization parameters required for this model are geometric parameters, correlation constants, thermal exposure profile and initial inlet flow conditions. Additional parameters related to stability and accuracy improvement strategies as previously discussed may also be needed if employed.

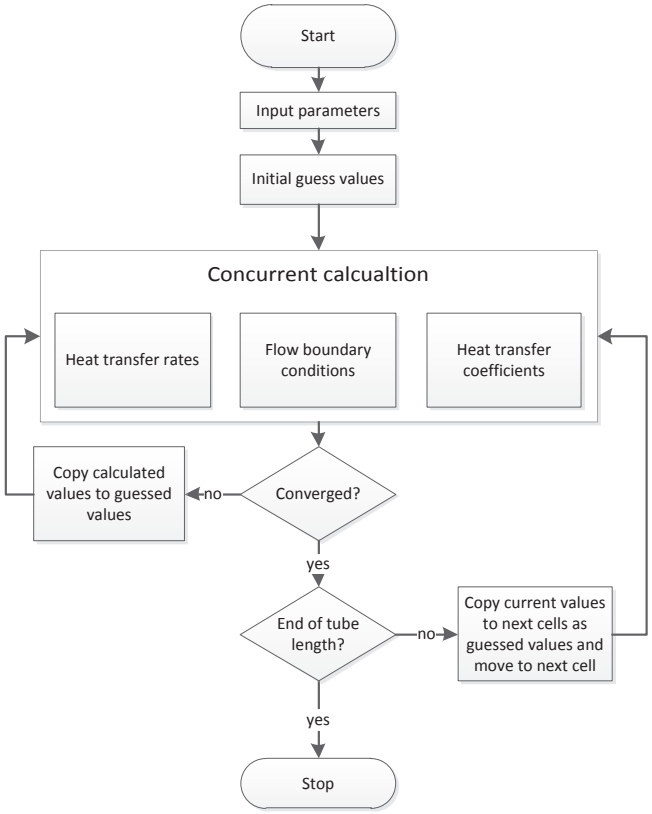


**Figure 4-3 Implicit numerical algorithm**

The heat and mass transfer models integrated into the implicit computational model described above is discussed in further detail in the proceeding section.

### 4.1.2 Internal heat transfer

The liquid and gas flows through the control volume element as represented in Figure 4-2 can be at dissimilar temperatures. In actual gas turbines, both fuel and air are subject to temperature rises prior to injection into a vaporizer respectively resulting from adiabatic temperature rise during compression and use of fuel as a coolant (Blazowski & Henderson, 1977). The practical implication of this is that interphasic heat transfer may occur which may contribute or reduce vaporization. Numerically, the lack of sufficient information to define the interphasic heat transfer is mitigated by the use of a thermodynamically equivalent homogenous mixture temperature. This temperature is related to the actual fluid temperatures with regards to mass weighted enthalpy values as shown in equation 4-1. Enthalpy

is used as it takes both internal energy and volumetric variations into account with the transition to the newly defined bulk fluid temperature. The bulk fluid temperature is only calculated as presented in equation 4-1 at the initial inlet plane with all proceeding liquid and gas temperatures inherently remaining similar.

$$xh_A(T_{flow}) + h_L(T_{flow}) = xh_A(T_A) + h_L(T_L) \quad 4\text{-}1$$

The heat transfer to the fluid flowing through the control element is dually calculated from the two phase heat transfer coefficient and energy conservation law represented in equation 4-2 and 4-3 respectively. The dual calculation method is also used as a convergence criterion owing to their partial numerical independence from one another.

$$Q_{internal} = h_{tp}A_{tube,inner}(T_{wall} - \overline{T_{flow}}) \quad 4\text{-}2$$

$$Q_{internal} = c_{p,mixture}(T_{flow,out} - T_{flow,in}) + h_{fg}\dot{m}_{vaporized} \quad 4\text{-}3$$

The two phase heat transfer coefficient is determined from a flow structure method as presented by Wojtan (2005) and described in section 2.4.4. This method requires, however, cooperation with experimental results to validate flow structure selection. This method further opens itself to varied complexity based on the extent of geometric models that are included for analyses. Adequate definition is obtained for the scope of this study by limiting the flow structure models to that of annular and stratified flow as illustrated in Figure 2-18.

### 4.1.3 Wall heat transfer

The very high heat transfer possible with vaporization and low thermal conductivity of Inconel is expected to result in a significant temperature difference across the tube wall. Assuming negligible axial conduction through the tube wall, the radial conduction heat transfer model used is shown in equation 4-4.

$$Q_{wall} = \frac{2\pi k_{Inconel} L_{element}}{\ln(D_{tube}/d_{tube})}(T_{tube,outer} - T_{tube,inner}) \quad 4\text{-}4$$

Constant thermal conductivity for Inconel of 20 W/mK as suggested in literature (Cengel & Cimbala, 2010) is used.

### 4.1.4 External heat transfer

Suitable numerical description of the heat transfer requires meaningful interpretation of the experimental data. The external heat source in the experimental setup is designed to replicate in-combustor conditions which resulted in a burner apparatus as shown in Figure 3-17. Visual observations of the

emitted flame structure shown in Figure 4-4 indicate a visible luminescent flame parameter with and without a vaporizer present.

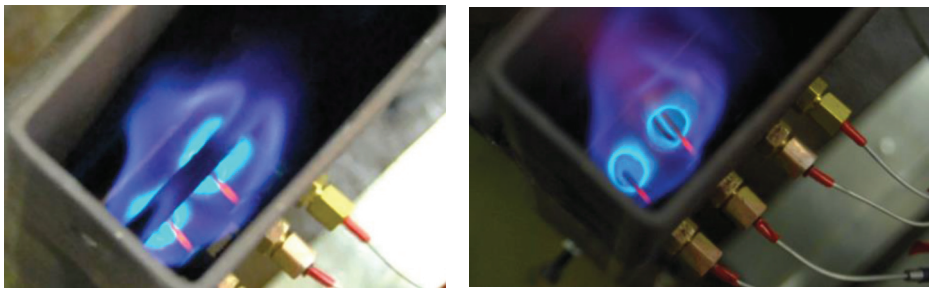

(a) flame structure with vaporizer (b) flame structure without vaporizer

**Figure 4-4 Experimentally observed flame structure**

Fundamentally, the external heat transfer from the combustion heat source to the tube wall has contributions by both convection and radiation heat transfers as indicated in equation 4-5.

$$Q_{external} = Q_{radiation} + Q_{convection} \quad 4\text{-}5$$

Conventional quantification of radiation and convection heat transfer rates are computed as shown in equations 4-6 and 4-7 respectively (Cengal & Cimbala, 2006).

$$Q_{radiation} = \varepsilon\sigma F A_{external}\left(T_{flame}^4 - T_{tube,outer}^4\right) \quad 4\text{-}6$$

$$Q_{convection} = h_{conv} A_{external}\left(T_{gas} - T_{tube,outer}\right) \quad 4\text{-}7$$

Interpretation of which temperature the thermocouples are measuring at the hand of Figure 4-5 reveal, however, that terms required to determine equations 4-6 and 4-7 are not easily obtained from measurement values.

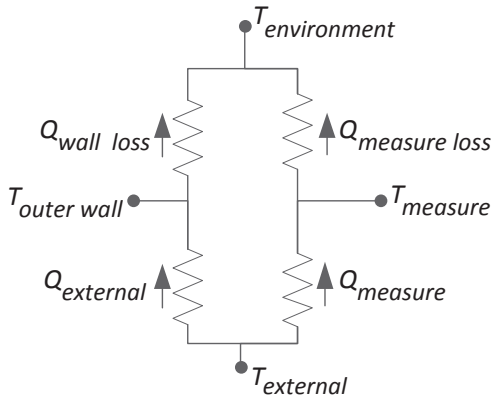


**Figure 4-5 Thermal resistance diagram relating to thermocouple measurement**

Nevertheless, the losses of the thermocouple to the environment, $Q_{measure\ loss}$, is minimized by reducing the thermocouple diameter and polishing the stainless steel sheaths (Shannon & Butler, 2002). Further, during experiments temperature measurements are allowed to stabilise which by application of Kirchhoff's current law on the thermal diagram shown in Figure 4-5 implies that $Q_{measure}$ has reached a similarly minimised value than $Q_{measure\ loss}$. The heat transfer from the tube wall to the environment, $Q_{wall\ loss}$, is inevitable, but is minimised by the position of the tube section within the flame as shown in Figure 4-4. Therefore, the measured temperatures are a sufficiently close approximation of the effective flame temperature to which the vaporizer is exposed to, albeit the incursion of reduced heat losses to the environment.

The relative contribution of radiation and convection heat transfer is expected to vary along the tube's length due to the high order temperatures dependency of radiation heat transfer and the varied external temperature profiles. Due to the restriction of temperatures to limit the amount of vaporization during experiments, however, the overall influence of convection is presumed to be greater than that of radiation. Therefore the numerical treatment of the effective external heat transfer more closely resembles that of convection heat transfer as shown in equation 4-8.

$$Q_{external} \cong h_{external} A_{external} (T_{external} - T_{tube,outer}) \qquad 4\text{-}8$$

The external heat transfer coefficient is determined as indicated in equation 4-9 using an empirically fitted Nusselt number.

$$h_{external} = \frac{Nu_{external} k_{external}}{D_{tube}} \qquad 4\text{-}9$$

The form and coefficient values for the Nusselt number are dependent on geometry and flow conditions (Cengal & Cimbala, 2006). With the experimental setup the hot gasses are directed perpendicular to the test section as illustrated in Figure 4-1. The specific implementation of the Nusselt number as an effective heat transfer correlation rather than a purely convective heat transfer correlation negates the validity of recommended constants. The general form of the Nusselt correlation as shown in equation 4-10 (Cengal & Cimbala, 2006, p. 435) is therefore used for empirical fitment.

$$Nu_{external} = CRe^{m} Pr^{n} \qquad 4\text{-}10$$

The exponents $m$ and $n$ are constant and usually have a value between 0 and 1 with the constant $C$ being dependent on flow geometry (Cengal & Cimbala, 2006). Based on the similarity of alternative correlations presented by Cengal &

Cimbala (2006, p. 436), the Prandtl number exponent is selected as $1/3$ to limit the investigation towards the determining of $m$ and $C$.

The absence of a velocity measurement in defining the external flow conditions inhibits the direct calculation of the Reynolds number. This is treated by removing the velocity term from the Reynolds number and grouping it with the correlation constant as shown below.

$$CRe^m \rightarrow C\left(\frac{v\rho D}{\mu}\right)^m \rightarrow (Cv^m)\left(\frac{\rho D}{\mu}\right)^m \rightarrow C^* Re^{*m}$$

The grouped velocity and correlation coefficient is represented as a modified constant, $C^*$, and the remainder of the Reynolds number parameters is represented as a partial Reynolds number, $Re^*$. Assuming a uniform velocity magnitude along the test length, the modified constant should remain constant irrespective of the internal flow conditions.

The aforementioned modifications allow for the application of the Nusselt correlation presented in equation 4-10 to describe external heat transfer using a competent methodology. All properties values are calculated assuming dry air behaviour using exterior temperature and ambient pressure.

### 4.1.5 Internal pressure gradient

The pressure gradient realising from flow through a vaporizer is caused by gravitational, interface shear and momentum forces. The current study, however, negates static pressure gradient contribution by limiting the scope to horizontally orientated flow. Due to the relative magnitudes of the two remaining pressure gradients, a further assumption is made that shear induced pressure gradient is negligible relative to that induced by momentum shift. This assumption is made with due regard to the relative low length to internal diameter ratio of the investigated flow domain and the high degree of momentum shift which occurs. The momentum pressure differential shown in equation 4-11 is obtained from integration of the differential form of the momentum conservation law presented in 2-13 with inclusion of the aforementioned assumptions.

$$\Delta P = \frac{\dot{m}_{total}{}^2}{A_{tube}{}^2}\left[\frac{(1-x)^2}{(1-\alpha)\rho_L} + \frac{x^2}{\alpha\rho_G}\right]_{inlet}^{outlet} \qquad 4\text{-}11$$

The necessity to include a pressure gradient calculation in initial computations is, however, questioned as reported accounts indicate maximum pressure differential magnitudes of only up to 12% of the upstream pressure for a comparatively sized MGT (Gonzalez, Wong, & Armfield, 2007). Additionally, the experimental design shown in Figure 3-15 only includes a pressure measurement of the ambient

pressure at the outlet of the vaporizer test section. Calculation of the upstream pressure by incorporating equation 4-11 into the forward marching computational scheme and using the measured outlet pressure values leads to an additional convergence criterion. This additional criterion results in making the model significantly more computationally expensive. With due regard to other implemented simplifications, the added complexity will arguably not lead to much improvement of the model's accuracy.

The increased simplicity resulting from expanding the pressure gradient assumption to further neglect any pressure differential over the computational domain, due to the low reported values thereof, is a compelling compromise which solicits further investigation.

### 4.1.6 Property models

Paraffin property models are approximated by Dodecane surrogate fuel. Dodecane is a recommended surrogate fuel to paraffin as it simplifies combustion analyses of multicomponent fuels (Gonzalez, Wong, & Armfield, 2007).

Air properties are determined assuming dry air conditions. Under these conditions the gas density is determined assuming the ideal gas behaviour using a gas molar mass of $28.964\ g/mol$. Other thermodynamic property models are derived from curve fitting to tabulated data as presented in B2.

All property data is obtained using miniREFPROP® (NIST, 2012).

### 4.1.7 Numerical stability and convergence

The aforementioned models are implemented into a computational algorithm as illustrated in Figure 4-3 using a first order upwind forward marching scheme. Although this scheme is inherently stable, three techniques are used to further promote numerical stability and accuracy.

A forwards marching scheme is inherently stable owing to two fixed initial conditions and a common end convergence criterion. The first technique used to improve the scheme's stability and convergence accuracy is first order quasi-transient damping. This technique is implemented on the implicitly calculated heat transfer rate as shown in equation 4-12. A history transition damping term, $\Phi$, is used in this equation to dampen the rate at which the implicitly acquired heat transfer rate is updated. This technique limits the risk of initial divergence considerably which would otherwise result owing to extreme initial guesses.

$$Q_{new} = \Phi Q_{old} + (1 - \Phi) Q_{calculated} \qquad 4\text{-}12$$

The majority of the correlations incorporated into the numerical model are only defined within certain ranges and present computational difficulties at their limits. The transition from two phase flow to fully gaseous flow is observed to result in such a numerical discrepancy. The apparent spiked increase of heat transfer coefficient (Wojtan, Ursenbacher, & Thome, 2005, p. 2981) that occurs just prior to complete dry out of annular flows especially results in inducing a wildly excessive prediction of vaporization which contradicts conservation laws. Logical qualifiers are used to enforced adherence to the mass conservation laws and negate irrational model behaviour.

The last strategy used to ensure numerical stability is to ensure discretization independence. An independence study is conducted whereby the resolution of the computational domain is decreased until a satisfactory compromise between computational time and accuracy is obtained.

The forward marching scheme works by incrementally attaining elemental convergence as it progresses through the computational domain. The convergence criteria used in this study is when either an error threshold from a computed energy transfer error variance or an iteration limit is reached.

The energy transfer error variance is calculated as the sum of the deviations from the mean value from the associated parameters. In addition to the two energy transfer values as computed from equations 4-2 and 4-3, an overall energy transfer value as computed from equation 4-13 is used as the three convergence criterion parameters.

$$Q_{total} = \left(R_{external} + R_{wall} + R_{tp}\right)^{-1}\left(T_{external} - \overline{T_{fluid}}\right) \qquad 4\text{-}13$$

Investigation of the model revealed that solution convergence is predominantly reached within 40 iterations, which is subsequently chosen as the iteration limit.

## 4.2 Analytical investigations

Analytical investigations are conducted to ascertain confidence in the numerical proficiency of the model, validate assumptions, observe model behaviour and adapt correlation coefficients to suit experimental data.

### 4.2.1 Discretization independence

Discretization independence is determined as the resolution required where after discretization has no significant effect on computation results. The influence of other factors and uncertainty is reduced by using a reference scenario of constant values and flow rates. This reference scenario is chosen so as to result in the full vaporization of liquid in both stratified and annular flow conditions and thus cover

the entire scope of fluid transition and induce progression past model discontinuities. This scenario is defined as:

- Constant external temperature of 800 $K$
- Constant external heat transfer coefficient of 4565.78 $W/m^2K$
- Air and paraffin flows of 4 $g/s$ and 0.5 $g/s$ respectively both at 300 $K$
- Constant pressure of 100 $kPa$
- Internal and external tube diameter of 6mm and 7mm respectively
- Constant slip ratio of 100
- Convergence criteria of 1e-6 error variance or 40 iterations

A uniformly spaced discretization is used over a 100mm computational domain. The overall heat transfer to the fluid is computed and normalised relative to the value obtained from the finest discretization scenario. The results of this analysis are presented in Figure 4-6 for domain resolutions from 25 to 200 nodes.

From Figure 4-6 it can be seen that variance in both annular and stratified models are rapid to converge to near perfect solutions. It should be noted, however, that even the coarsest discretization results in inducing only up to 0.6% variation to converged values. This is a good indication of the high degree of discretization independence achieved by the model.

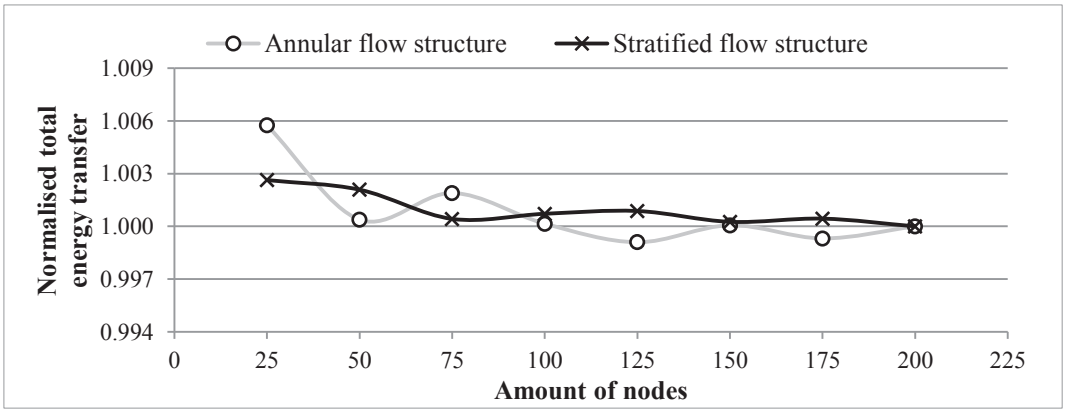


**Figure 4-6 Normalised total energy deviation vs. discretization resolution**

An inspection of the heat flux profile at the occurrence of dry-out, shown in Figure 4-7, is conducted to investigate the cause of oscillations observed in the convergence behaviour.

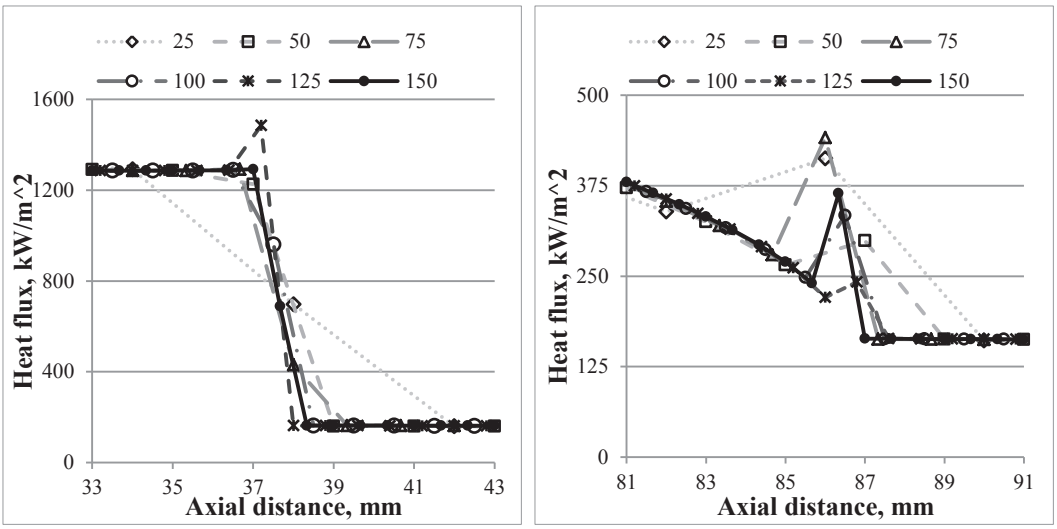


(a) Annular structure (b) Stratified structure

**Figure 4-7 Heat flux vs axial distance for various amounts of nodes**

The deviations visible from the profiles presented in Figure 4-7 are attributed to result from the model's inherent discontinuity at these locations. The oscillations visible in convergence are consequently resulting from discretization. An increase in discretization resolution is observed to reduce the weight of the incurred error, measured as area between the resulting curve and the more continuous curve, as well as varying its magnitude, measured as the height of the resulting peak. During initial refinement of coarse resolutions, the net effect of these two factors contributes to reduce the converged prediction. As refinement progresses beyond 100 nodes, the area over which the induced numerical error at the point of model discontinuity occurs is reduced to such an extent that area dependant properties such as heat flux appears as an apparent spike. This behaviour resembles that reported in literature for this model (Wojtan, Ursenbacher, & Thome, 2005).

Rational judgement is used to decide on using a 100 node discretization scheme for further numerical investigations. This resolution is observed to presents adequate numerical accuracy to describe the described phenomena, whilst being computationally less resource expensive than higher resolution discretization.

### 4.2.2 Behavioural analysis with regards to slip ratio

The slip ratio represents the ratio of gas to liquid velocity and is incurred during the derivation of the void factor as presented in equation 2-22. Although its accuracy in proper representation is debated (Ould Didi, Kattan, & Thome, 2002), its simple form is best suited for the current study as motivated in section 2.4.6.

Slip ratio values which are assumed to be constant are only reported for the value of 1 validating homogenous flow conditions. The flow through vaporizers is

observed to defy this condition most strongly owing to the injection of the liquid and short flow distance through the vaporizer itself. The desirability of using a constant slip ratio is motivated further as it is

- adjustable to best fit behaviour inclusive of interphasic shear
- solves model divergence at discontinuity without additional terms
- reduces the amount of dependencies between parameters

The first reason given is representative of a compromise between empirical observations and numerical proficiency. As mentioned in section 2.4.2, definition of interaction at interphasic surface is limited, yet the occurrence of certain phenomena is noted. Using similar conditions as for the analysis performed in section 4.2.1, the slip ratio is kept constant and its value varied from $10^{-1}$ to $10^{4}$. The overall heat transfer rate and resulting percentage pressure drop as calculated from equation 4-11 is used to indicate model behaviour. This interpreted use of the slip ratio appears to be more prominent on the stratified than annular flow models as seen from the profiles presented in Figure 4-8.

Values between 1 and $10^{3}$ appear to have inconclusive influence on annular flow model behaviour. A gradual approach of both calculated measurement parameters using the stratified model towards those resulting from the annular model is visible with an increase of the slip ratio value. The sudden decline in pressure drop above values of $10^{3}$ is, however, conspicuous behaviour. It should be noted, however, that such a high value implies either near stationary liquid or very high velocity gas movement; both of which are scenarios not expected to occur for flow through vaporizers.

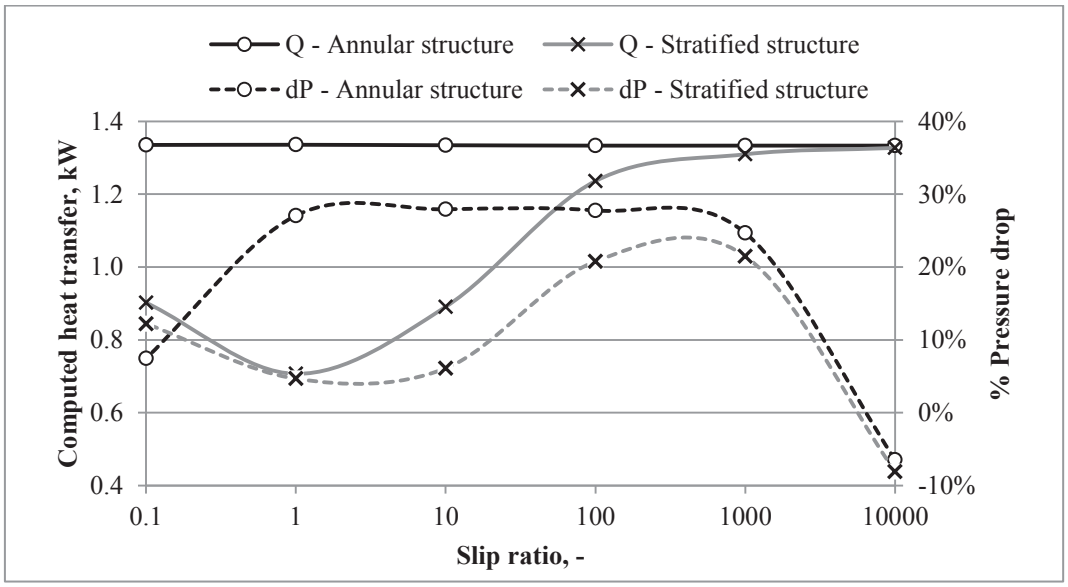


**Figure 4-8 Influence of slip ratio on heat transfer and % pressure drop**

An investigation of alternative model behaviour with regards to the slip ratio parameter is conducted by reducing the fixed value assumption to that of the liquid phase. The gas phase is calculated from conservation laws and the resulting slip ratio is then calculated as shown in equation 4-14.

$$S = \frac{\dot{m}_{gas}}{\rho_{gas} A_{tube} v_L} \qquad 4\text{-}14$$

The assumption of fixing the liquid's axial velocity is validated by due regard of the dynamics influencing liquid movement. The liquid's initial velocity resulting from injection is assisted by the interphasic shear, yet opposed by the wall shear. The additional momentum decrease resulting from vaporization adds increased gas velocity and thereby also the probability of significant turbulence. Therefore assuming that the resulting velocity gradients pertaining to the opposing stresses will result in a maintained apparent liquid velocity until dry out seems reasonable. The liquid's velocity is determined from equation 4-15 using injection characteristics.

$$v_L = \left( \frac{4\dot{m}_L}{\rho_L \pi d_{needle}^2 \cos\theta_{injection}} \right)_{@inlet} \qquad 4\text{-}15$$

Comparison of the model behaviours is conducted by referring to the calculated heat flux profiles as shown in Figure 4-9 using equation 4-14 and varied constant slip ratio values.

The method of determining the slip ratio appears to have no influence on the annular flow heat transfer model, but a significant influence is observed on the stratified flow model as seen in Figure 4-9. Unique features from the stratified flow results that require further attention are the apparent humps and sudden spike occurring before transition to the lower asymptotic value. Judging from the results presented in Figure 4-9, a constant slip ratio of 100 is selected for further numerical investigations. This fixed value presents less numerical complexity and a similar heat flux profile for stratified flow than using a calculated slip ratio.

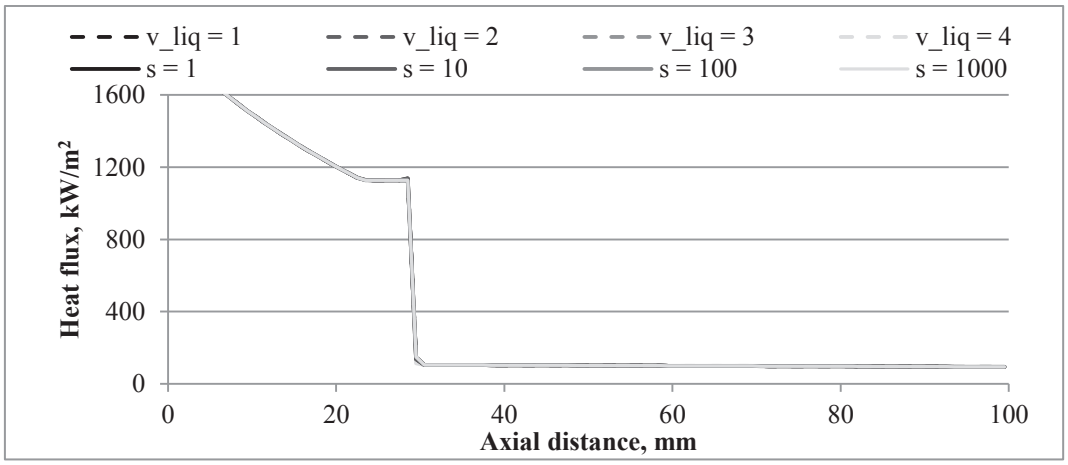


(a) Annular structure

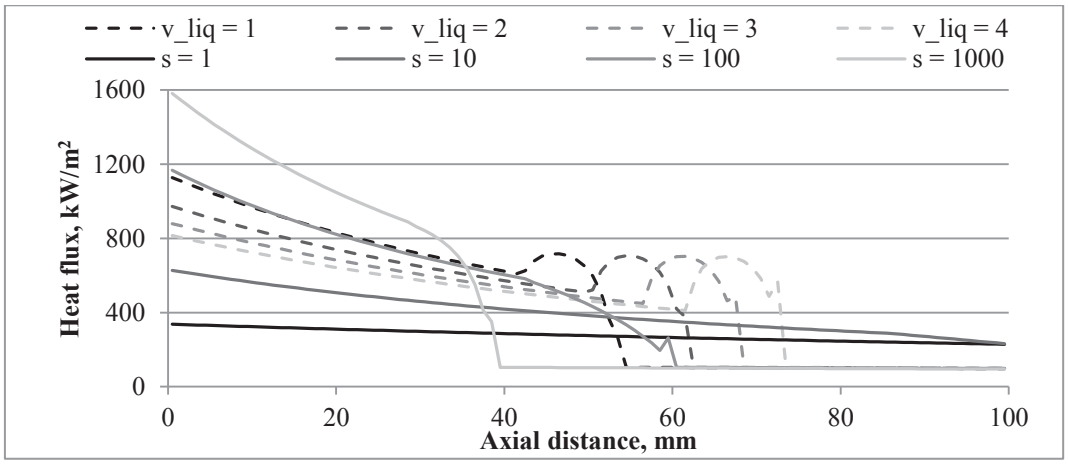


(b) Stratified structure

**Figure 4-9 Heat flux comparison using alternative slip ratio models**

### 4.2.3 Suitability of thermal exposure profile

Experimental measurements of the exterior thermal profile are made at four positions as indicated in Figure 3-17. Relating these discretely defined measurements to the continuity of the numerical model solicits creative adaption reinforced by critical consideration.

The apparent high temperature rings visible in Figure 4-4 appear to merge somewhat with the inclusion of the vaporizer test section. The apparent smoothing of the flame structure with the presence of the vaporizer tube gives reasonable motivation to approximate the thermal profile as four plateaus with a smooth transition in between. This is numerically simulated as a continuous function by summating of series of Sigmoid functions as shown in equation 4-16.

$$T_{flame} = T_{measure_1} + \sum_{i=1,2,3} \Delta T_{measure_{i,i+1}} \left(\frac{1}{1+e^{x_i - x}}\right)^{damping} \qquad 4\text{-}16$$

The four quadrant model proposed is a crude representation of the thermal profile, but successfully achieves the incorporation of measurements into the numerical model as a continuously defined function. Additionally, the damping parameter provides a further degree of smoothing. The model behaviour is analysed with regards to the variation of the thermal profile damping factor using quadrant temperatures of 400, 600, 800 and 1000 degrees Kelvin respectively as indicated in Figure 4-10. Model behaviour is again evaluated based on heat flux profile for variations in the damping parameter of equation 4-16. Only annular flow is considered using all other computational parameters as presented in section 4.2.1.

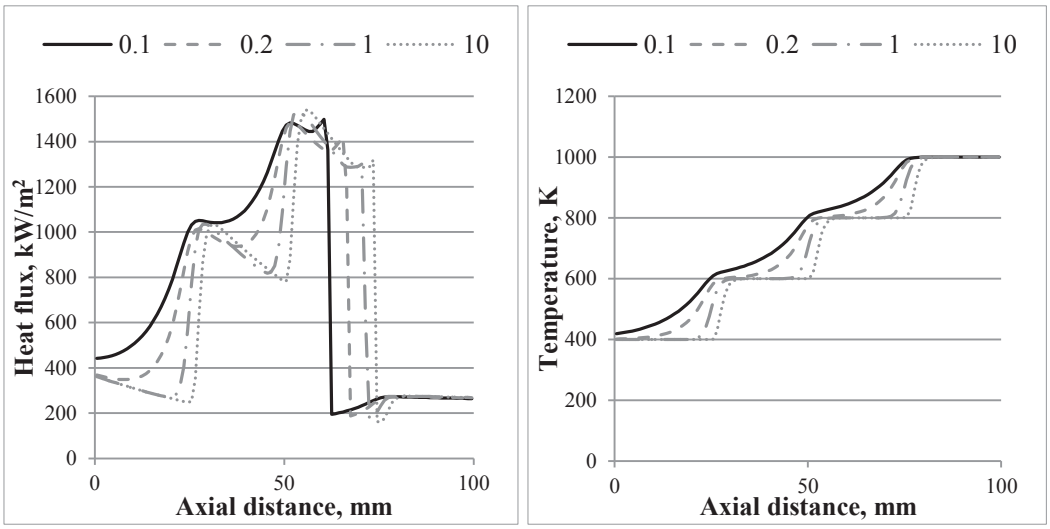


(a) Heat flux profile (b) External thermal profile

**Figure 4-10 Effect of thermal profile damping on heat flux**

A decrease in the damping coefficient results in smoothing the thermal profile and as expected also the exhibited heat flux profile. A variance of up to 45.18 degrees Kelvin and 71.10 W are calculated from the average exposure temperatures and overall heat transfers respectively. This realised to a variance of 9.54 degrees Kelvin of the internal flow outlet temperature and a shift in the dry out point of 7 mm. These indicators are, however, relatively inconclusive with regards to other known uncertainties in directing selection of an appropriate damping value.

It can be noted that a damping coefficient larger than 1 is observed to result in promoting a more stepped thermal profile which decreases both the average thermal exposure and resulting heat transfer and vice versa for a damping coefficient smaller than 1. A damping value of 0.2 is therefore recommended. This value results in a transition which maintains localised plateaus where measurements are taken and results in a smooth transition as expected.

### 4.2.4 Empirical fitment of convective coefficients

External heat transfer is determined from an effective heat transfer coefficient as shown in equation 4-8. The effective external heat transfer coefficient is empirically determined from the Nusselt correlation presented in equation 4-10. The lack of an external gas velocity measurement, however, solicits further numerical manipulation of this correlation to accommodate its usage.

The modified constant, $C^*$, is empirically determined by correlating predicted and measured vaporization performance. This is done for varied values of the Reynolds exponent, $m$, and using a constant value of $1/3$ for the Prandtl exponent, $n$. The value of $m$ is reported (Cengal & Cimbala, 2006) to vary between 0 and 1 and as such the values of 0.5, 0.6 and 0.7 where used. These values are selected to be large enough to give significant influence by the factors described by the Reynolds number, whilst not dominating subsequent factors described by the Prandtl number. The resulting modified constant values are presented in Figure 4-11 relative to AFR as calculated using forced annular and stratified flow structure for heat transfer calculations respectively.

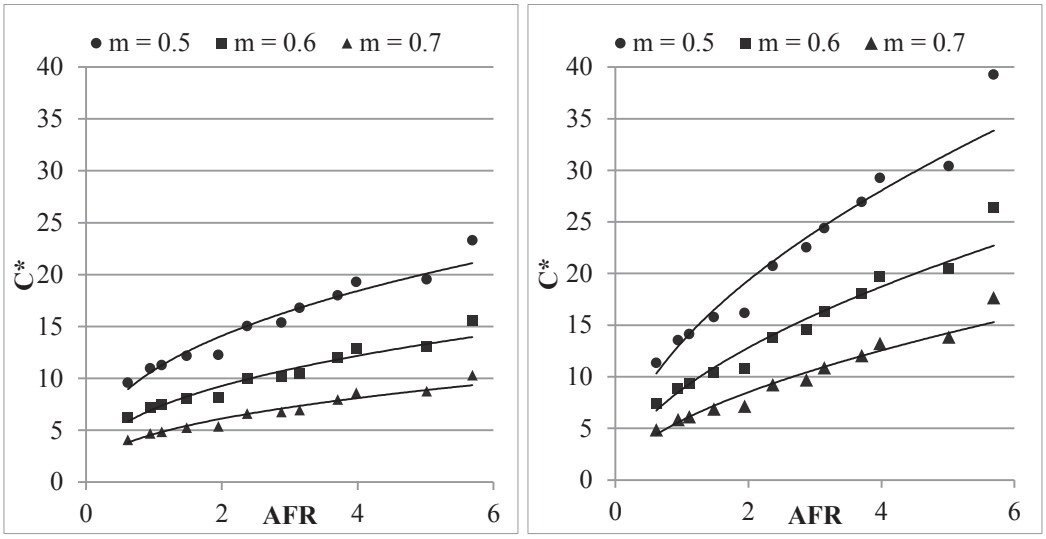


(a) Annular flow structure (b) Stratified flow structure

**Figure 4-11 Modified convection coefficients: Separate structure models**

Inspection of Figure 4-11 shows an apparent decline and sudden jump occurring near AFR of 2 with both models. Although this occurrence may be due to experimental error, its close agreement with flow conditions corresponding with the transition between stratified and annular as deduced from Figure A-1 solicits an investigation to the possibility of influence by flow regime. A synergy of computed results is made using stratified flow values prior to AFR of 2 and annular flow values thereafter. The resulting modified constant data set is presented in Figure 4-12.

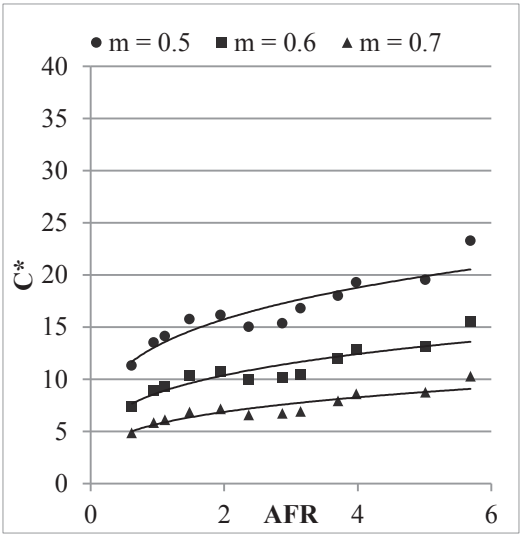


**Figure 4-12 Modified convection coefficients: Combined structure model**

The decision to represent empirically determined data with respect to AFR is prompted from the close relationship observed between vaporization to AFR seen in Figure 3-20. Results resented in Figure 4-11 and Figure 4-12 contradicts the expectation of a constant value for the $C^*$ parameter.

The relationship between $C^*$ and the AFR is best described using a power function. Inspection of the resulting power functions indicated similar exponent values for all fitted functions of each separate flow structure model data sets. This solicits the amendment of the $C^*$ parameter to include the AFR raised to an empirically determined exponent. This amends the Nusselt correlation indicated in equation 4-10 to the form as presented in equation 4-17.

$$Nu_{external} = CRe^m Pr^n AFR^p \qquad 4\text{-}17$$

The constants of the fitted functions are used to derive values for the instituting parameters of the $C^*$ term. The values of the correlation constant and effective uniform velocity are calculated using a GRG Nonlinear solver within MS Excel using the fitted function constants and known $m$ values. The determined values for $C$, velocity and AFR exponent, $p$, are summarised in Table 4-1.

**Table 4-1 Empirically determined values**

| Flow structure | $C$ | Velocity [m/s] | $p$ |
|---|---|---|---|
| Annular | 89.339 | 0.0146 | 0.3946 |
| Stratified | 93.016 | 0.0206 | 0.5476 |
| Combined | 113.375 | 0.0137 | 0.2598 |

### 4.2.5 Behavioural analysis of including and neglecting pressure

Numerical analyses until now have assumed a constant pressure scenario to reduce model complexity and isolate parameter influences. As previously discussed, the large degree of phase transition and short distance of the analysed vaporizer is adequately described by assuming only a pressure gradient due to momentum shift. The need to include this, however, is questioned as literature accounts indicated very low pressure differentials.

It is reasoned that neglecting pressure would not result in much error at low vaporization conditions and maximise during near complete vaporization. As test case A12 resulted in the highest amount of vaporization, similar flow conditions are used for this investigation.

Mass dependent properties are expected to not be affected as significantly by a variation in pressure than temperature, but this cannot be said for volume dependent properties of compressible fluids. Assuming the liquid representative of paraffin to be incompressible, the only flow properties expected to be significantly influenced during this investigation are gas densities. As the slip ratio is closely related to the volumetric flow of gas and thus its density, this parameter is included in variations.

The configurations investigated relate to the four possibilities of varied or constant slip and pressure values. The constant slip and constant pressure configuration is used as a reference case. The converged results of these configurations are shown in Figure 4-13 and Figure 4-14 showing parameter variations along the flow axis and variation relative to the reference case values.

The reference case resulted in a predicted pressure differential of 12.77kPa and overall heat transfer rate of 1114W with an average simulated pressure of 100kPa and a resulting Nusselt number constant of 23.279 using a 0.5 Reynolds exponent.

Because the Nusselt relation parameters are subject to large degree of inherent variance, the empirical constant is adjusted to fit measured data whilst using a varied pressure and varies slip configuration. In doing so, the Nusselt constant is observed to be reduced by 7% in order to achieve similar vaporization amounts. The resulting pressure differential is observed to be on 8% higher and the average simulation pressure 10% higher than for the reference scenario.

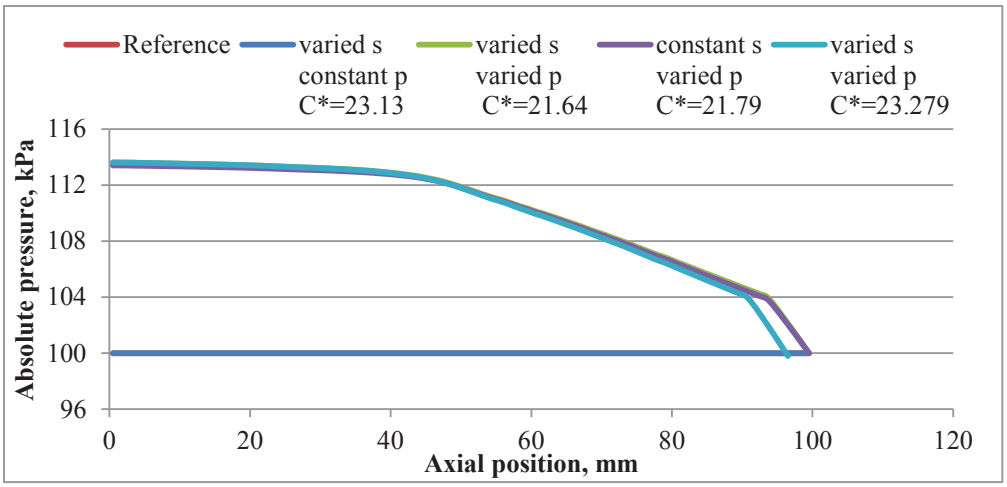


(a) Pressure profile

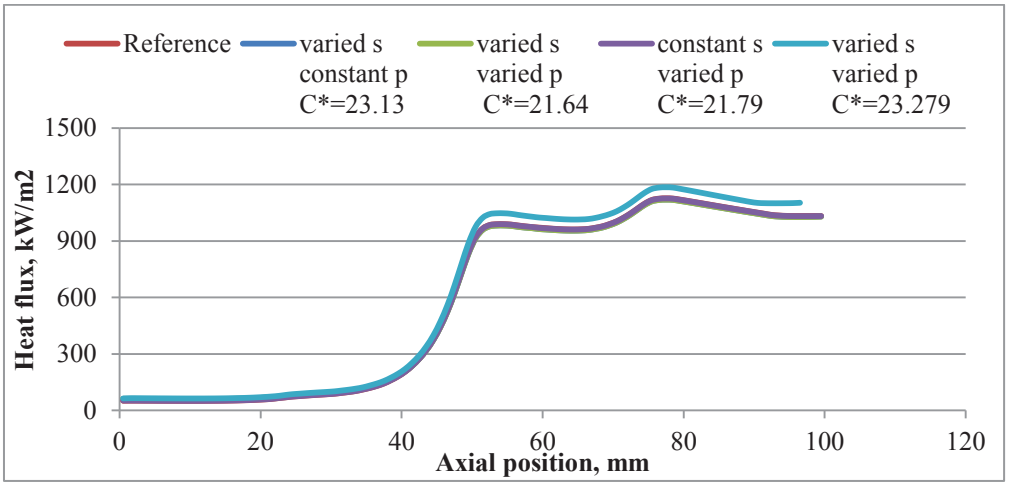


(b) Heat flux profile

**Figure 4-13 Influence of pressure variance on predicted flow profiles**

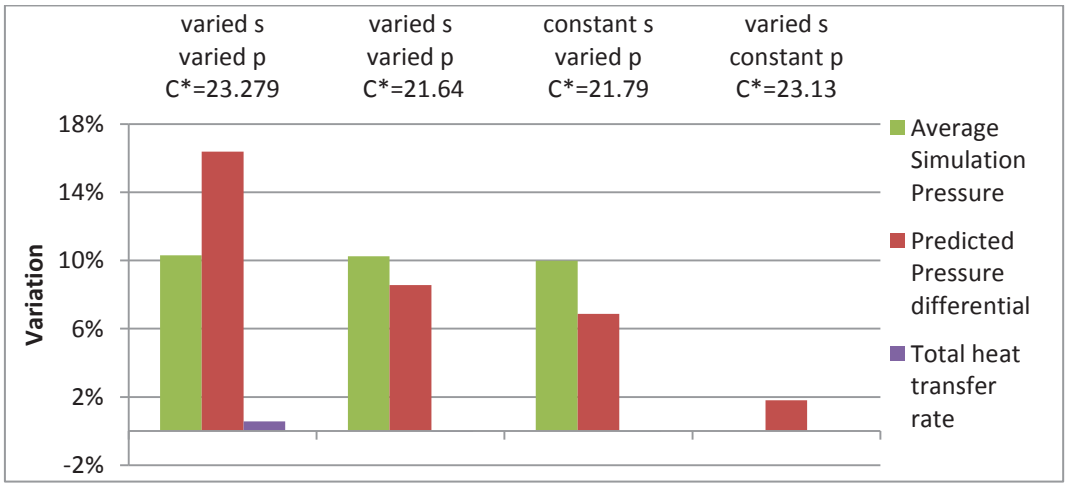


**Figure 4-14 Relative variation relative to reference case**

Using a constant slip ratio value and adjusting Nusselt parameters to fit the predicted vaporization amounts, resulted in only marginally reducing the magnitudes of all variances. This confirms that the selected value and simplification of using a constant slip ratio has relatively insignificant influence on the presented flow scenario and is therefore a valid approximation.

Inspection of the results presented in Figure 4-13 and Figure 4-14 shows an increase of 16% and 0.57% in the predicted pressure drop and overall heat transfer respectively with the use of similar amended Nusselt relation parameters as determined for the reference configuration. The percentage variation of the predicted pressure is considerably higher than would be acceptably negligible. It should be noted, however, that the magnitude of the variation is merely 2 kPa and is attributed to the additional amount of vaporization resulting from the difference in the computational scenario used to fitted coefficients of equation 4-17.

The small magnitude of the variation is, however, small enough to not influence crude combustor analyses significantly based on the observed variation of only 2% it induces on the operational pressure ratio (Lefebvre & Ballal, 2010) shown in equation 4-18.

$$Overall\ pressure\ loss = \frac{\Delta P_{combustor}}{P_{abs,upstream\ from\ combustor}} \qquad 4\text{-}18$$

Therefore, the assumption to neglect pressure gradient within a numerical model is deemed valid for crude analyses of vaporizers and associated combustors if coefficients are fitted using a similar numerical configuration.

### 4.2.6 Model proficiency analysis

The final form of the numerical model using the recommendations presented in the aforementioned sections is used to predict vaporization performance using experimentally measured flow conditions.

The numerical model is configured with a constant slip value of 100, an external thermal profile with damping of 0.2 and incorporated the amended Nusselt number correlation with values presented in Table 4-1 using a Reynolds exponent of 0.5. The three possible flow structure models relating to purely annular, purely stratified and combined stratified-annular flow structures are used. Measurement values of the ingest flow rates, the amount of vaporization and temperatures of the aforementioned model configuration are used as input arguments to predict vaporization performance. Figure 4-15 shows the correlation of measured and predicted values for all three flow structure models with 20.84% error tolerance bands relating to the determined uncertainty of the vaporization rate measurement as determined in section 3.4.

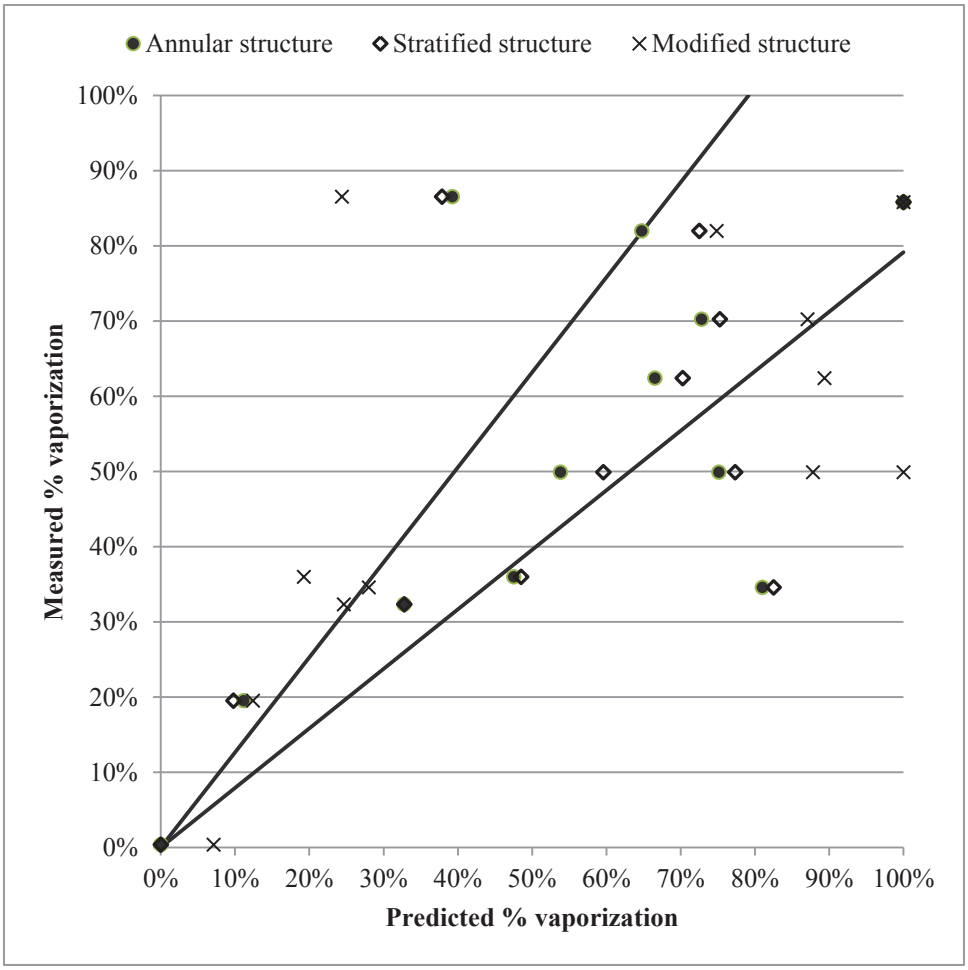


**Figure 4-15 Comparison of predicted vaporization to measured vaporization**

A clustering of vaporization performance data is seen in Figure 4-15. Prediction values of the annular and stratified models are closely correlated, but the combined model deviates substantially. A general tendency of all three models to over predict vaporization performance is apparent from the majority right shift of correlated points from the unity line except for very low values of vaporization which are under predicted. Prediction accuracy of 58.33%, 58.33% and 41.67% is attained with the annular, stratified and combined structured models respectively within the experimental error bands.

The prediction confidence of the model is classified as fair for use of either pure annular or stratified flow owing to achieving more than 50% prediction accuracy. Using a combined empirically fitted model did, however, result in reduced accuracy contrary to initial expectations.

## 4.3 Model review

The numerical modelling approach investigated provided insight into the dynamics of theoretical models and empirical requirements to amend deficiencies and produce a robust model. The resulting profile predictions is discussed and followed by noteworthy insights derived along the way.

The derived model achieved fair prediction confidence by using either pure annular or stratified flow structured model, but deteriorated when using a part-wise empirically fitted data model. This is based on results shown in Figure 4-15 where predicted vaporization performance is presented against measured values within experimental error bounds. The degree of scatter suggests that additional attention should be given to generating more empirical data and refinement of the numerical model as presented.

The flow structure approach proposed by Wojtan (2005) gives logical definition of the contribution by each individual heat transfer mechanisms and as such can easily be numerically manipulated to represent flow structures as observed experimentally. Forced behaviour based on flow regime expectations is, however, observed to not be as accurate in predicting vaporization amounts as using purely annular or stratified flow structured models. The lack of accuracy is attributed to a lack of definition and empirical data to adequately define empirically determined coefficients.

The large degree of variability inherent in the derivation as described lends itself to much uncertainty. The uncertainty is largely, however, unavoidable due to measurement limitations and computational capabilities which necessitate simplifications and assumptions. Despite the assumptions imposed by limitations and accompanying inherent uncertainty, the presented model does achieve in uniting many individually defined phenomena into a unified descriptive model.

Notable simplifications are those concerning the slip ratio, the thermal profile and the pressure gradient. Arguments are presented in support of the associated assumptions and following a series of analyses recommendations are presented based on critical judgement and reasonable justification.

The assumption to neglect pressure gradient during analyses of vaporisers is proposed due to low reported pressure drop of comparable configuration (Gonzalez, Wong, & Armfield, 2007) and the high operational vapour quality. Analyses of this assumption revealed that a neglect of pressure gradient during calculation results in under predicting the pressure drop due to over prediction of the vaporization. The magnitude of this under prediction is, however, observed to have a relatively insignificant influence on the overall pressure loss ratio indicated in equation 4-18 used for combustor design. Thus the assumption to neglect a

pressure gradient during simulation of vaporizers is validated for mass fluxes similar to those presented in this study.

The assumption to use a non-unity slip ratio is proposed due to lack of defining parameters required for alternative correlations and inevitable requirement to make an assumption regarding phasic velocities. Analysis of the influence that present with variation of the slip ratio value led to the recommendation of applicability limits between 1 and 1000 for a fixed slip ratio value based on reasonability of observed model behaviour. Comparison of the heat flux and pressure profiles shown in Figure 4-9 and Figure 4-13 respectively derived using a fixed and intrinsically determined slip ratio as calculated from equation 4-14 indicates that a constant slip ratio value of 100 replicates model behaviour well. The similarity in behaviour and benefit towards numerical stability and simplification qualify in making using a constant non-unity value slip ratio a reasonable assumption, despite concerns of reported inaccuracies (Thome, 2005).

The assumption of using Dodecane to approximate fluid properties of paraffin is expected to result in over predicting the amount of vaporization as compared to paraffin. Dodecane only accounts for the more volatile components within the paraffin mixture. Furthermore, the age and fidelity of dodecane property values from literature cause some concern. The use of fitted models at constant pressure further adds to the error uncertainty associate with the numerical model. In light of the lack of characteristic data for the paraffin mixture used in tests, the application of these assumptions and approximations are as accurate as required.

The saturated vaporization model as presented in equation 2-23 deliver a simple and efficient manner of predicting vaporization. The structure of this relation negates the possibility of sub-cooled nucleate boiling to occur and as such is reported to under predict the amount of vaporization (Doster, 2006). Complications relating to the vaporization profile through the vaporizer are negated by empirical fitment based on the measured and predicted amounts of vaporization. The vaporization process is, however, dependent on the liquid's volatility and inevitable variations can be expected. Incorporation of more complex vaporization mechanisms such as sub-cooled nucleation boiling will benefit analyses regarding the critical operational conditions of vaporizers. Nevertheless, the added complexity is not recommended for the current state of vaporizer analyses as ideal vaporizer operation is to result in full vaporization which will negate the measureable difference between the use of equation 2-23 and a more detailed model.

# 5.
# Conclusion

The series of experimental and numerical work conducted as part of this study aimed to establish an introductory investigation towards vaporizers and relate results to their application in combustion chambers. Some notable insights were obtained during the analyses and are presented here in conclusion to this study.

## 5.1 Summary

The results indicate that flow regime is important in assisting vaporization. This is attributed to the variation in heat transfer which occur dependent on flow structure. Of the observed flow regimes, the annular flow structure is seen to contribute the most to assisting vaporization. Flow structures are observed to be influenced by flow rate, in-tube AFR and injection angle.

Experimental replication of in-combustor conditions to determine vaporization performance is subject to much uncertainty. The largest contribution of uncertainty with the used measurement equipment determined to be fluid property variations.

Theoretical modelling of vaporizers requires much empirical data to determine correlation coefficients and adequately replicate vaporizer performance behaviour. A series of assumptions and simplifications were investigated and their error contribution qualitatively evaluated. Following these assumptions, a pure annular flow structured numerical model is seen to more accurately predict vaporization than either stratified or part-wise defined structured models.

In all, good agreement of vaporizer operating conditions and recommendations are seen between experimental, predicted results and literature.

## 5.2 Experimental results

Two experimental investigations were conducted based on guidance from literature and measured amount of vaporization as performance criteria.

Results from the first experimental investigation indicated that the initial flow length following injection is much affected by injection angle. Within this initial flow length the resulting flow regime is much dependent on air and paraffin flow rates and the resulting AFR. Populated flow maps for three different injection angles indicated a shift in the occurrence of annular flow with a 45 degree injection angle resulting in the largest possibility of annular flow within tested

flow condition ranges. A similar analysis is conducted on the flow observed within the test section near its outlet and revealed alike flow regime maps for all injection angles. This similarity of flow maps at the outlet section confirms experimental repeatability as it indicates that bulk flow conditions of the experimental scenarios are unaffected between tests.

The second experimental investigation was aimed at validating vaporizer performance. Design and manufacture of experimental equipment was conducted with guidance of equipment capabilities and flow regime results. A 45 degree injection angle was used to maximise the probability of achieving annular flow as visually confirmation is impractical. The rig replicated thermal exposure conditions to the vaporizer test section with combustion heat source imitative of that within the combustor and readily achieved vaporization. From consolidating experimental results with the applicable flow regime map, it is deduced that flow regime has a profound effect on vaporization with annular flow exhibiting maximized vaporization.

Flow condition within the recommended AFR range for vaporizers agreed well with measurements of vaporization and observed conditions resulting in annular flow. This observation further agrees well with recommendations found in literature regarding the recommended in-tube AFR.

## 5.3 Numerical model development

The numerical investigation was aimed at observing the behaviour of a numerical model to validate assumptions, propose simplifications and identify shortfalls. As such the array of correlations and accompanying assumptions and manipulation methods presented during the numerical investigation provide a benchmark towards further numerical investigation and areas of concern and further attention.

A forward marching computation scheme was used on a steady state one-dimensional heat and mass transfer model. The model was developed based on correlations found in literature and derived conservation laws for two-phase flow. Due to the significance of flow structure within the vaporizers, a two phase heat transfer correlation which incorporated flow structure as proposed by Wojtan (2005) was used. This modelling approach allowed for the numerical manipulation of flow structure to better agree with observed flow regimes.

Incorporation of all the presented correlation and simplifications resulted in providing an empirically tuned model that correlated predicted data with experimental results up to 58.33% accuracy within experimental tolerance bounds. Individual numerical models exhibited behaviours similar to those reported in literature which adds to the confidence of overall model integration.

The thermal exposure profile derived for the numerical investigation is made to facilitate numerical representation and experimental data incorporation. Observed variations of the flame structure from experimental equipment indicate possible increases of the temperatures at distinct locations away from thermocouple positions. The capabilities and experimental setup available during this study limited further investigation into this concern. A further implication of this is the use of an effective heat transfer coefficient as opposed to separate contributions by radiation and convection. An analysis of the thermocouple measurement is used to argue the validity of this approach which is observed in retrospect to deliver good performance. Future endeavours are recommended, however, to better define the external temperature profile experimentally. This is important in further numerical investigations as temperature dependency of the heat transfer mechanisms play a significant role in vaporization near critical operational conditions such as start-up and re-ignition.

The predicted pressure drop over the vaporizer agrees well with reported pressure drops for MGTs. This comes despite a critical assumption to neglect the pressure gradient during calculations and to determine its value from resulting boundary conditions. Nevertheless, its magnitude is observed to remain small within a 16% variation which relates to an induced error of 2% variation of the pressure drop to operating pressure ratio used for combustor design. Thus, because of the high vapour quality of the fluids moving through vaporizers, relatively low pressure differentials can be expected and a pressure gradient can be reasonable neglected during element based simulations without affecting combustor design significantly.

The slip ratio is inherent in all two phase correlations as it is used to relate the void factor to the vapour quality factor. The use of a constant non-unity slip ratio value was compared to a scenario where only liquid velocity was assumed to be fixed. These two methods were observed to result in similar behaviour and resulted in affecting predicted pressure drop by less than 1%. Thus a constant non-unity slip ratio can be reasonably used without significantly influencing vaporizer flow behaviour.

# 6.
# Recommendations

This study is intended as an introductory investigation towards vaporizers. As such, many topics were investigated with due adequacy, but limited scope. During the course of investigations, many alternative investigations were identified which are recommended to direct the continuation of research into vaporizers.

It is recommended to use flow regime maps to assist in the design of incorporating vaporizers into combustors as to promote conditions which increase the probability of attaining annular flow structure. Population of flow maps to assist in this process can be conducted similar to that presented in this study.

Future experimental investigations should be aimed at determining the influence of heat source to vaporizer orientation on vaporization. The settling of paraffin at the bottom of the vaporizer during stratified flow may be negatively affected by a heat source exposed to the upper surface of the vaporizer as opposed to the bottom surface as was tested here.

Development of future investigations will benefit much from measurements of the pressures upstream and downstream of the combustor, the axial temperature profile within the combustion volume and the temperature of the vaporizer wall during actual operation of the BMT120KS MGT. These measurements can be used to better define the operational conditions of the combustor and vaporizers which can be used to better evaluate performance and gauge contributions of design variations. Inevitably vaporizers will benefit from a more defined combustor and design variations required to promote vaporizer performance can be made with due regard for the influence it may have on combustor characteristics.

Endeavours regarding the numerical modelling of vaporizers should be focused on the accuracy and synergy of experimental data and numerical interpretation. Despite the high level of simplification of the presented experimental setup in comparison to alternative studies conducted on vaporizers by Barnes (1954) and Jasuja (1987), numerical interpretation of the data still required a high degree of deduction and interpretation. Future work should aim to reduce this amount of required deduction as it induces inaccuracies and increases parameter independency. The two parameters of most concern are those of the temperature of the vaporizer and the pressure differential across the vaporizer.

# 7.
# References

Ambrose, D., & Tsonopoulos, C. (1995). *1-Dodecane*. Retrieved September 29, 2014, from National Institute of Standards and Technology: Material Measurement Laboratory: http://webbook.nist.gov/cgi/cbook.cgi?ID=C112403&Mask=4#ref-1

Baker, O. (1954). Design of pipelines for the simultaneous flow of oil and gas. *Oil Gas Journal, vol. 53*, pp. 185–195.

Barnes, R. (1954). *A study of the effect of various fuels on the optimim length of a gas turbine combustor equipped with a vaporizer tube.* Minnesota: University of Minnesota.

Biberg, D. (1999). An Explicit Approximation forthe Wetted Angle in Two-Phase Stratified Pipe Flow. *The Canadian Journal of Chemicla Engineering*, 1221-1224.

Blazowski, W., & Henderson, R. (1977). *A review of turbopropulsion combustion.* Springfield: National Technical Information Service.

Cengal, C., & Cimbala, C. (2006). *Heat and Mass transfer 4th ed.* McGraw Hill.

Cengel, Y., & Cimbala, J. (2010). *Fluid Mechanics: Fundamentals and Applications.* New York: McGraw Hill.

Chen, J. (1966). A Correlation for Boiling Heat Transfer to Saturated Fluids in Convective Flow. *Industrial and Engineering Chemistry, Process Design and Development, Vol. 5, No. 3*, 322-329.

Chisholm, D. (1973). Pressure gradients due to friction during the flow of evaporating two-phase mixtures in smooth tubes and channels. *International Journal of Heat and Mass transfer*, 16:347-358.

Cohen, H., & Rogers, G. (1958). *Gas Turbine Theory.* London: Longmans, Green and Co.

De Villiers, L. (2014). *Design of a Centrifugal Compressor for Application in Micro Gas Turbines, Masters thesis.* Stellenbosch: Stellenbosch University.

Dittus, F., & Boelter, L. (1930). *University of California Publication, Vol. 2*, 443.

Doster, J. (2006, August 23). *Two Phase Flow* . Retrieved May 31, 2014, from North Carolina State University: http://www4.ncsu.edu/~doster/NE402/Text/TwoPhaseFlow/TwoPhaseFlow.pdf

Englar, B. (2010, December 16). *Build your own RC turbine engine.* Retrieved July 8, 2014, from http://sv -precious-moments.com/xbob.htm

Friedel, L. (1979). Improved friction pressure drop correlations for horizontal and vertical two-phase pipe flow. *European Two-Phase Flow Group Meeting, Paper E2*.

Giedt, W. (1949). Investigation of variation of point unit-heat transfer coefficient around cylinder normal to an air steam. *Transcript ASME, vol.71*, 375-381.

Gonzalez, C., Wong, K., & Armfield, S. (2007). Computational study of a micro-turbine engine combustor usign large eddy simulation and Reynolds averaged turbulence models. C407-C422.

Gronemann, P. (2012, July 7). *File:RAF Eurofighter Typhoon.jpg*. Retrieved November 5, 2014, from Wikipedia: http://en.wikipedia.org/wiki/File:RAF_Eurofighter_Typhoon.jpg

GTBA. (1999, unknown unknown). *FD3-64 Engine design*. Retrieved August 7, 2014, from Gas turbine builders association: http://gtba.co.uk/engine_designs/schreckling.php

GTBA. (2010). *Engine designs*. Retrieved July 8, 2014, from Gas Tubrine Builders Association: http://gtba.co.uk/engine_designs/

Henderson, R., & Blazowski, W. (1989). *Aircraft Propulsion Systems: Technology and Design.* Washington, DC: American Institute of Aeronautics and Astronautics, Inc.

Herzog, J. (2013, June 17). *File:Eurojet EJ200 for Eurofighter Typhoon PAS 2013 01 free.jpg*. Retrieved November 5, 2014, from Wikipedia: http://en.wikipedia.org/wiki/File:Eurojet_EJ200_for_Eurofighter_Typhoon_PAS_2013_01_free.jpg

http://img.vx.com/uploadfile/data/2014/0126/. (n.d.). Retrieved November 19, 2014, from http://img.vx.com/uploadfile/data/2014/0126/20140126082524576.jpg

Jasuja, A., & Low, H. (1987). *Spray performance of a vaporizer fuel injector.* Cranfield: DTIT.

Jung, D. S., & Radermacher, R. (1989). Prediction of Pressure Drop During Horizontal Annual Flow Boiling of Pure and Mixed Refrigerants. *Int. J. Heat Mass Transfer, Vol. 32, No. 12*, 2435-2446.

K.S. Shannon, K., & Butler, B. (2003). *A Review of error associated with thermocouple temperature measurement in fire environments.* Missoula, Montana: USDA Forest Service, Fire Sciences Laboratory, Rocky Mountain Research Station.

Kandlikar, S. (1990). A General Correlation for Saturated Two-Phase Flow Boiling Heat Transfer Inside Horizontal and Vertical Tubes. *Journal of Heat Transfer, vol. 112*, 219-228.

Kattan, N. (1998). Flow boiling in horizontal and vertical tubes: the effect of tube orientation on heat transfer.

Krige, D. (2013). *Performance Evaluation of a Micro Gas Turbine, Masters thesis.* Stellenbosch: Stellenbosch University.

Krige, D., & Beard, A. (2014, March). (A. Olivier, Interviewer)

Kroeger, D. (1998). *Air-cooled Heat Exchangers and Cooling Towers.* Stellenbosch: Stellenbosch University.

Lefebvre, A. (1989). *Atomization and Sprays.* Boca Raton, Florida, USA: CRC Press.

Lefebvre, A., & Ballal, D. (2010). *Gas turbine combustion.* Boca Raton, Florida, USA: CRC press.

Liu, X. (2012). Influence of gravity on gas-liquid two-phase flow in horizontal pipes. *International journal of multiphase flow 41*, 23-35.

Lockhart, R., & Martinelli, R. (1949). Proposed correlation of data for isothermal two-phase two component flow in pipes. *Chemical Engineer Progr 45*, 39-45.

Mattingly, J. (2006). *Elements of Propulsion: Gas Turbines and Rockets.* Blacksburg, Virginia: American Institute of Aeronautics and Astronautics, Inc.

Muller-Steinhagen, H., & Heck, K. (1986). A simple friction pressure drop correlation for two-phase flow in pipes. *Chemical Engineering Process*, 20:297-308.

NATO. (1971). *Small gas turbines for helicopter and small gas turbines.* London: Advisory Group for Aerospace Research and Development.

NIST. (2012). miniREFPROP, database 23, vers. 9.1. United States of America.

NREC. (1980). *The design and development of gas turbine combustors.* Woburn: Northern Research and Engineering Corporation.

Ould Didi, M., Kattan, N., & Thome, J. (2002). Prediction of two-phase pressure gradients of refrigerants in horzontal tubes. *International Journal of Refridgeration*, 935-947.

Overton, D., Langley, K., & Millener, P. (1992). *Patent No. 5,133,192.* United States of America.

Quiben, J., & Thome, J. (2007). Flow pattern based two-phase frictional pressure drop model for horizontal tubes, Part II: New phenomenological model. *International journal of heat and fluid flow 28*, 1060-1072.

Rouhani, S., & Axelsson, E. (1970). Calculation of volume void fraction in the subcooled and quality boiling regions. *International journal of Heat Mass Transfer, vol 13*, 383-393.

Rowley, G. (2003). *Patent No. 6,578,532.* United States of America.

Shah. (1982). Chart Correlation for Saturated Boiling Heat Transfer: Equations and Further Study. *ASHRAE Transactions, vol 88 part 1*, 185-196.

Shannon, K., & Butler, B. (2002). *A review of error associated with thermocouple temperature measurement in fire environements.* Montana: USDA Forest Service, Fire Sciences Laboratory, Rocky Mountain Research Station.

Taitel, Y., & Dukler, A. E. (1976). A Model for Predicting Flow Regimes Transitions in Horizontal and Near Horizontal Gas-Liquid Flow. *AIChE, vol. 22, No. 1*, 47-55.

Thome, J. (2005). Update on advances in flow pattern based two-phase heat transfer models. *Experimental Thermal and FLuid Science 29*, 341-349.

Van der Merwe, S. (2014, October 28). (A. Olivier, Interviewer)

Wambsganss, M., FranceD.M., Jendrzejczyk, J., & Tran, T. (1993). Boiling heat trnasfer in a horizontal small-diameter tube. *Journal of heat transfer, vol 115*, 963-972.

Wattelet, J. (1994). Predicting boiling heat transfer in a small-diameter round tube using an asymptotic method. *Convective flow boiling*, 377-382.

Whittle, F. (1946). The early history of the Whittle jet propulsion gas turbine. *Institute of Mechanical Engineering*, 419-435.

Williams, F. (1985). *Combustion Theory: The Fundamental Theory of Chemically Reacting Flow Systems 2nd ed.* Menlo Park, California: The Benjamin/Cummings Publishing Company, Inc.

Wojtan, L., Ursenbacher, T., & Thome, J. (2005). Investigation of flow boiling in horizontal tubes: Part 2 - Development of a new heat transfer model for stratified-wavy, dryout and mist flow regimes. *International journal of heat and mass transfer, vol. 48*, 2970–2985.

Wojtan, L., Ursenbacher, T., & Thome, J. (2005). Investigation of flow boiling in horizontal tubes: Part I - A new diabatic two-phase flow pattern map. *International journal of heat and mass transfer*, 2955-2969.

Zürcher, O., Thome, J., & Favrat, D. (2000). Evaporation of ammonia in a smooth horizontal tube: heat transfer measurements and predictions. *Journal of Heat Transfer, vol. 121*, pp. 89–101.

# Appendix A.
# *Experimental work*

## A1. Measured data

The experimental data for experiments as described in section 3 of this report.

**Table A-1 Vaporization performance test: flow regime dependency tests**

| Scenario ID | Air mass flow rate | Paraffin mass flow rate | Vaporization rate | Mass flux | AFR |
|---|---|---|---|---|---|
| # | [g/s] | [g/s] | [g/s] | [kg/sm$^2$] | [-] |
| a1 | 0.407 | 0.660 | 0.003 | 37.731 | 0.616 |
| a2 | 0.625 | 0.662 | 0.129 | 45.491 | 0.944 |
| a3 | 0.707 | 0.635 | 0.205 | 47.460 | 1.113 |
| a4 | 0.932 | 0.629 | 0.226 | 55.184 | 1.482 |
| a5 | 1.194 | 0.614 | 0.212 | 63.947 | 1.946 |
| a6 | 1.601 | 0.675 | 0.337 | 80.515 | 2.371 |
| a7 | 1.791 | 0.623 | 0.311 | 85.371 | 2.875 |
| a8 | 1.997 | 0.635 | 0.396 | 93.094 | 3.145 |
| a9 | 2.342 | 0.632 | 0.444 | 105.173 | 3.704 |
| a10 | 2.621 | 0.659 | 0.540 | 115.979 | 3.980 |
| a11 | 3.021 | 0.602 | 0.517 | 128.165 | 5.016 |
| a12 | 3.493 | 0.614 | 0.531 | 145.275 | 5.689 |

**Table A-2 Vaporization performance test: varied parametric tests**

| Scenario ID | Air mass flow rate | Paraffin mass flow rate | Vaporization rate | Total mass flux | AFR |
|---|---|---|---|---|---|
| # | [g/s] | [g/s] | [g/s] | [kg/sm^2] | [-] |
| b1 | 4.001 | 0.647 | 0.202 | 164.383 | 6.183 |
| b2 | 4.029 | 0.641 | 0.160 | 165.151 | 6.285 |
| b3 | 3.932 | 0.573 | 0.130 | 159.330 | 6.864 |
| b4 | 3.953 | 0.594 | 0.069 | 160.817 | 6.660 |
| b5 | 4.018 | 0.641 | 0.212 | 164.766 | 6.268 |
| b6 | 4.018 | 0.601 | 0.222 | 163.336 | 6.690 |
| b7 | 4.018 | 0.601 | 0.233 | 163.336 | 6.690 |
| b8 | 4.017 | 0.641 | 0.189 | 164.748 | 6.267 |
| b9 | 3.928 | 0.601 | 0.052 | 160.157 | 6.540 |
| b10 | 3.953 | 3.556 | 0.142 | 265.574 | 1.112 |
| b11 | 3.917 | 3.894 | 0.294 | 276.251 | 1.006 |
| b12 | 2.111 | 0.325 | 0.076 | 86.144 | 6.498 |
| b13 | 1.968 | 0.442 | 0.069 | 85.252 | 4.449 |
| b14 | 1.968 | 0.425 | 0.009 | 84.651 | 4.627 |
| b15 | 1.983 | 0.437 | 0.061 | 85.579 | 4.541 |
| b16 | 1.983 | 0.426 | 0.015 | 85.194 | 4.657 |
| b17 | 2.096 | 0.470 | 0.016 | 90.748 | 4.456 |
| b18 | 2.099 | 2.864 | 0.144 | 175.553 | 0.733 |
| b19 | 2.097 | 3.559 | 0.262 | 200.029 | 0.589 |

**Table A-3 Vaporization performance tests: measured data**

| scenario ID | Absolute pressure | Air | | | Paraffin | | Thermocouples | | | |
|---|---|---|---|---|---|---|---|---|---|---|
| | | Flow rate | Temperature | Gauge pressure | Flow rate in | Flow rate out | @ 12.5mm | @ 37.5mm | @ 62.5mm | @ 87.5mm |
| # | [kPa] | [L/min] | [K] | [Bar] | [mL/s] | [mL/s] | [K] | [K] | [K] | [K] |
| **Flow regime dependency tests** | | | | | | | | | | |
| a1 | 100.7 | 2.759 | 290.3 | 6.425 | 0.825 | 0.822 | 322 | 385 | 922 | 981 |
| a2 | 100.6 | 4.167 | 290.4 | 6.393 | 0.827 | 0.666 | 339 | 384 | 928 | 1017 |
| a3 | 100.6 | 4.781 | 290.4 | 6.388 | 0.794 | 0.537 | 347 | 384 | 928 | 1038 |
| a4 | 100.6 | 6.304 | 290.4 | 6.349 | 0.786 | 0.503 | 350 | 378 | 945 | 1042 |
| a5 | 100.6 | 8.153 | 290.4 | 6.313 | 0.767 | 0.502 | 351 | 376 | 952 | 1099 |
| a6 | 100.6 | 11.032 | 290.3 | 6.282 | 0.844 | 0.423 | 351 | 377 | 973 | 1108 |
| a7 | 100.6 | 12.294 | 290.3 | 6.274 | 0.779 | 0.390 | 350 | 371 | 947 | 1111 |
| a8 | 100.6 | 13.806 | 290.3 | 6.261 | 0.794 | 0.298 | 349 | 369 | 948 | 1119 |
| a9 | 100.6 | 16.140 | 290.3 | 6.233 | 0.790 | 0.235 | 347 | 370 | 994 | 1115 |
| a10 | 100.6 | 18.145 | 290.3 | 6.215 | 0.823 | 0.148 | 345 | 363 | 986 | 1165 |
| a11 | 100.6 | 21.064 | 290.3 | 6.186 | 0.753 | 0.107 | 344 | 361 | 1014 | 1181 |
| a12 | 100.6 | 24.422 | 290.2 | 6.149 | 0.768 | 0.103 | 342 | 362 | 963 | 1135 |
| **Varied parametric test** | | | | | | | | | | |
| b1 | 101.4 | 28.076 | 287.3 | 6.053 | 0.809 | 0.557 | 485 | 865 | 941 | 341 |
| b2 | 101.4 | 28.253 | 287.5 | 6.048 | 0.801 | 0.602 | 474 | 861 | 918 | 323 |
| b3 | 101.4 | 27.816 | 287.1 | 5.977 | 0.716 | 0.554 | 443 | 835 | 927 | 336 |
| b4 | 101.4 | 27.705 | 286.8 | 5.993 | 0.742 | 0.655 | 439 | 835 | 902 | 334 |
| b5 | 101.4 | 28.194 | 287.3 | 6.052 | 0.801 | 0.536 | 380 | 490 | 529 | 330 |
| b6 | 101.4 | 28.194 | 287.3 | 6.052 | 0.751 | 0.473 | 380 | 490 | 529 | 330 |
| b7 | 101.4 | 28.194 | 287.3 | 6.052 | 0.751 | 0.459 | 380 | 490 | 529 | 330 |
| b8 | 101.4 | 28.224 | 287.4 | 6.050 | 0.801 | 0.565 | 376 | 488 | 521 | 326 |
| b9 | 101.4 | 27.746 | 287.1 | 5.986 | 0.751 | 0.685 | 355 | 472 | 506 | 325 |
| b10 | 101.4 | 27.705 | 286.8 | 5.993 | 4.444 | 4.267 | 447 | 839 | 892 | 337 |
| b11 | 101.5 | 27.685 | 286.9 | 5.978 | 4.867 | 4.500 | 365 | 467 | 506 | 327 |
| b12 | 101.4 | 14.530 | 286.8 | 6.163 | 0.406 | 0.311 | 434 | 943 | 1025 | 330 |
| b13 | 101.4 | 13.718 | 287.7 | 6.188 | 0.553 | 0.466 | 514 | 882 | 919 | 339 |
| b14 | 101.4 | 13.718 | 287.7 | 6.188 | 0.532 | 0.520 | 514 | 882 | 919 | 339 |
| b15 | 101.4 | 13.596 | 287.7 | 6.195 | 0.546 | 0.469 | 413 | 506 | 647 | 347 |
| b16 | 101.4 | 13.596 | 287.7 | 6.195 | 0.532 | 0.514 | 413 | 506 | 647 | 347 |
| b17 | 101.4 | 14.440 | 287.0 | 6.160 | 0.588 | 0.568 | 355 | 462 | 500 | 325 |
| b18 | 101.4 | 14.394 | 287.0 | 6.143 | 3.580 | 3.400 | 447 | 963 | 1003 | 337 |
| b19 | 101.4 | 14.454 | 287.1 | 6.153 | 4.448 | 4.121 | 382 | 487 | 516 | 328 |

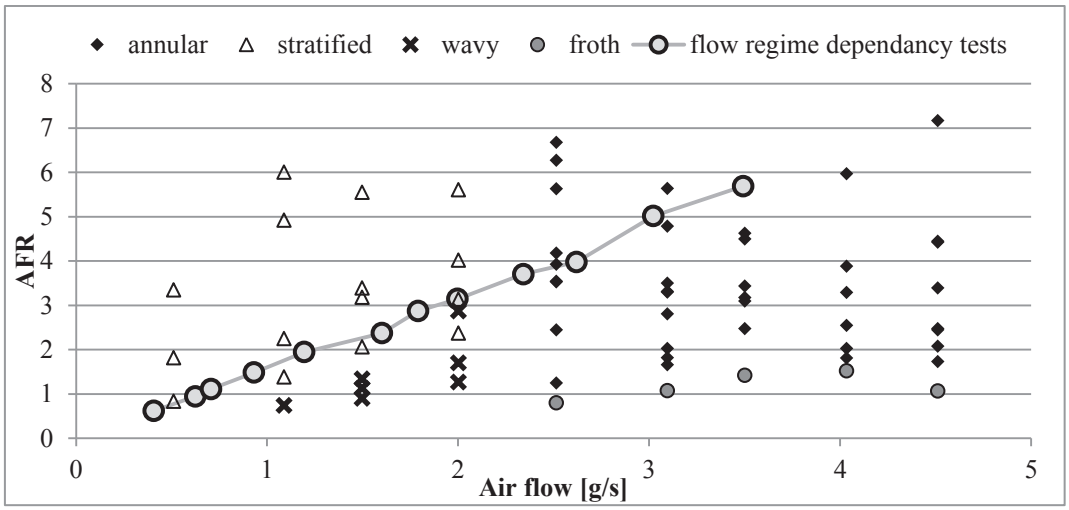


**Figure A-1 Flow regime tests: conditions relative to Figure 3-10 (a)**

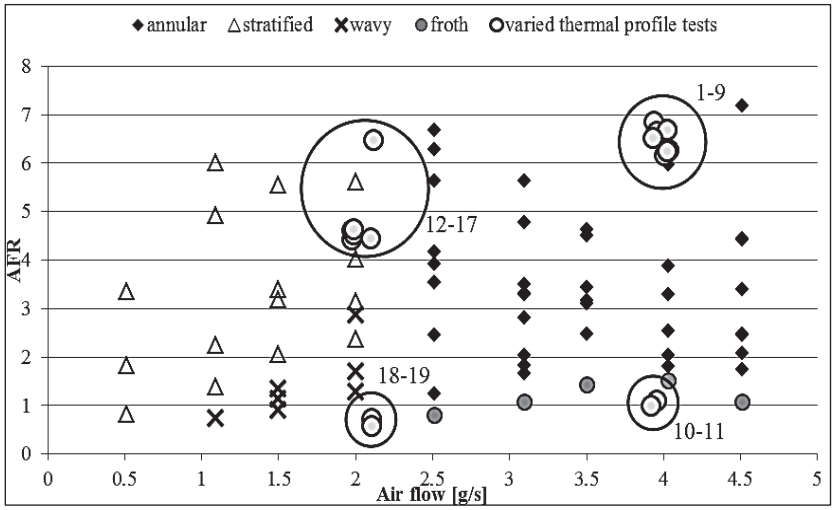


**Figure A-2 Parametric tests: conditions relative to Figure 3-10 (a)**

**Table A-4 Operation conditions of BMT 120 KS**

| Operational speed [kRPM] | Fuel flow [g/s] | Air flow [g/s] |
|---|---|---|
| 34 | 0.855 | 26.786 |
| 49 | 1.704 | 49.018 |
| 65 | 1.889 | 70.478 |
| 77 | 2.335 | 127.312 |
| 89 | 3.064 | 178.496 |
| 99 | 3.502 | 215.012 |
| 107 | 4.086 | 245.287 |
| 114 | 4.669 | 277.435 |
| 119 | 5.202 | 294.825 |
| 123 | 5.666 | 304.025 |
| 130 | 6.262 | 314.819 |

## A2. Observed flow structures

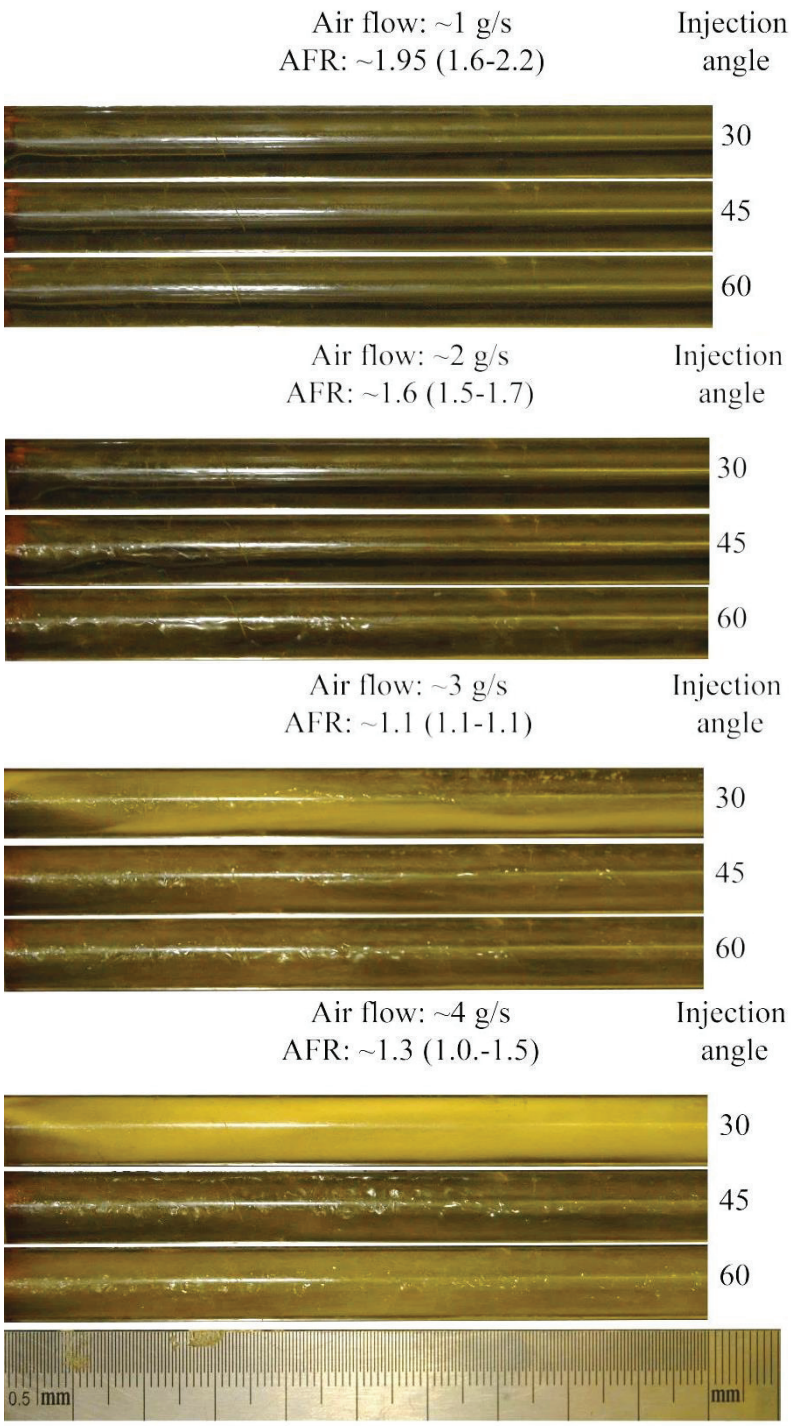


**Figure A-3 Visual observations at low AFRs for varied air flow and injection angles**

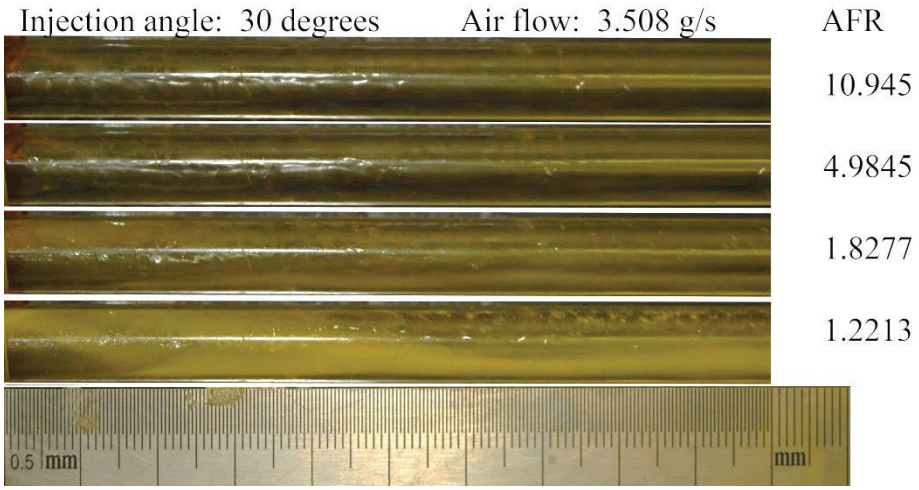


**Figure A-4 Visual observations at inlet region for 30 degree injection angle**

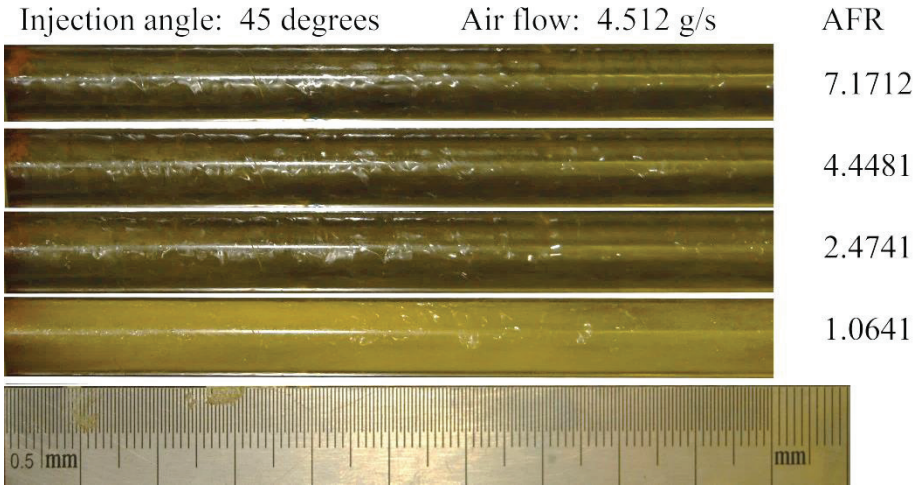


**Figure A-5 Visual observations at inlet region for 45 degree injection angle**

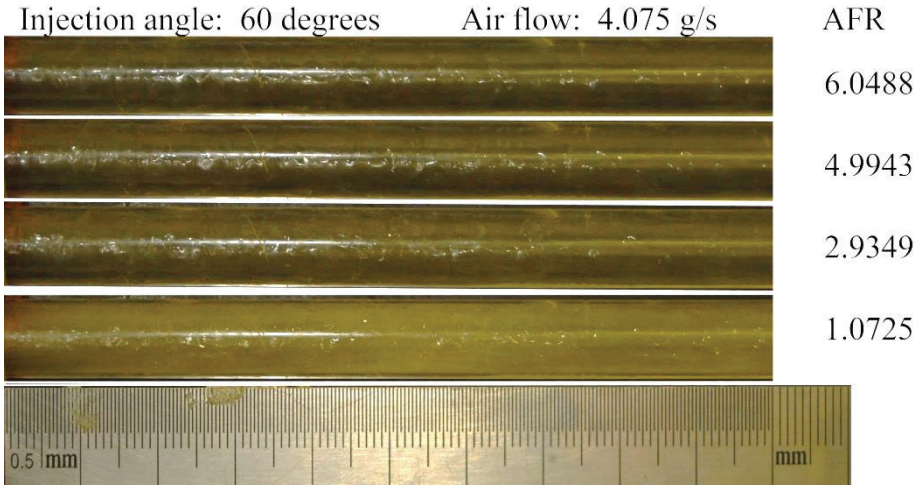


Figure A-6 Visual observations at inlet region for 60 degree injection angle

## A3. Sensor calibrations

Calibration is conducted for all measurement equipment. This included all pressure transducers and thermocouples, but excluded the volumetric flow meter which is received calibrated by the manufacturer prior to installation. The methods used for calibration and calibration data are presented in this appendix.

The supply pressure is calibrated with a precision dial gauge with range up to 1000 kPa and rated accuracy of 0.3% accuracy with a 5 kPa resolution. The pressure transducers used for tube pressure measurements were calibrated using a Betz 5000 with resolution of 2 Pa. The results from calibration are summarized in Table A-5 with calibration curves shown in Figure A-7.

**Table A-5 Calibration information: Pressure transducers**

| Measurement | Zero offset [mA] | Resolution [Pa/mA] | Variance [mPa] |
|---|---|---|---|
| $P_{supply}$ | 4.071 | 62893.1 | 0.69344 |
| $P_{cera}$ | 4.014 | 625.0 | 0.01116 |
| $P_{delta}$ | 4.047 | 187.6 | 0.15089 |

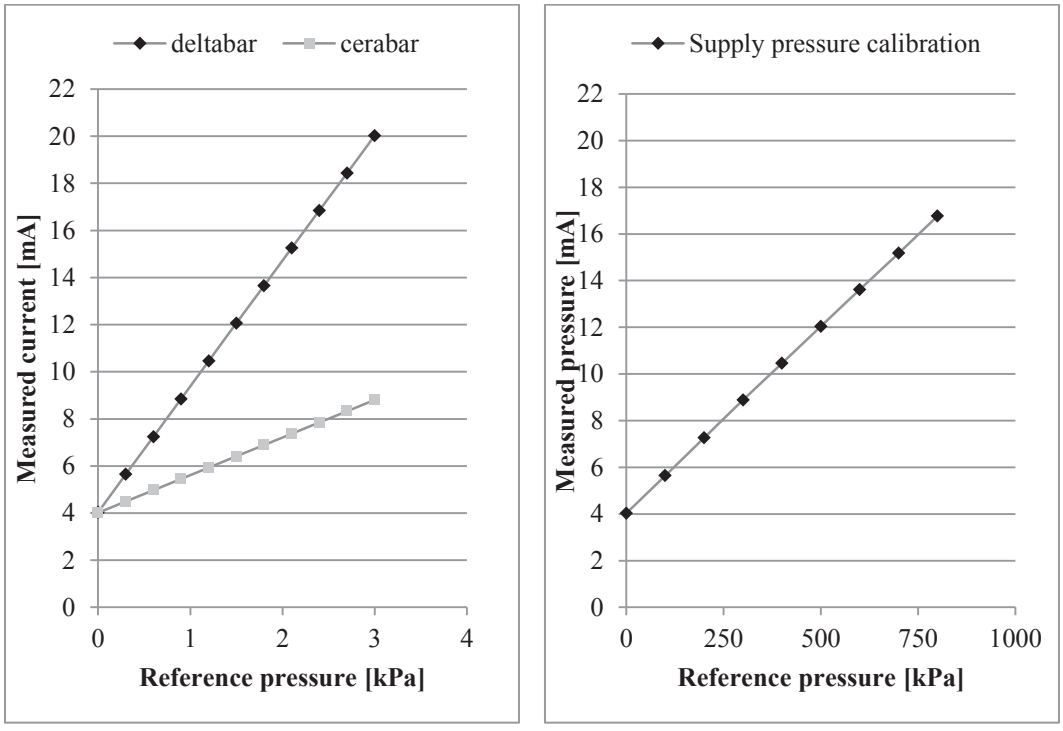


(a) Low pressure sensors (b) High pressure sensor

**Figure A-7 Calibration curves: Pressure sensors**

Thermocouples are calibrated using ice and boiling water. It is noted that vaporizing experiments exposed the thermocouples to temperatures exceeding the calibration range, but due to practical considerations higher temperatures could not be accurately attained. The accuracy of temperature measurements with these experiments was, however, not as important as the axial thermal profile that they indicated. Calibration results are summarized in Table A-6 with calibration curves shown in Figure A-8.

**Table A-6 Calibration information: Thermocouples**

| Measurement | Zero offset | Measurement gradient |
|---|---|---|
| | [K] | [K/K] |
| $T_{@12.5mm}$ | 0.161 | 1.00047 |
| $T_{@37.5mm}$ | 5.057 | 1.27719 |
| $T_{@62.5mm}$ | 5.280 | 1.28856 |
| $T_{@87.5mm}$ | 5.156 | 1.28698 |
| $T_{Air\ inlet}$ | 0.541 | 1.02857 |

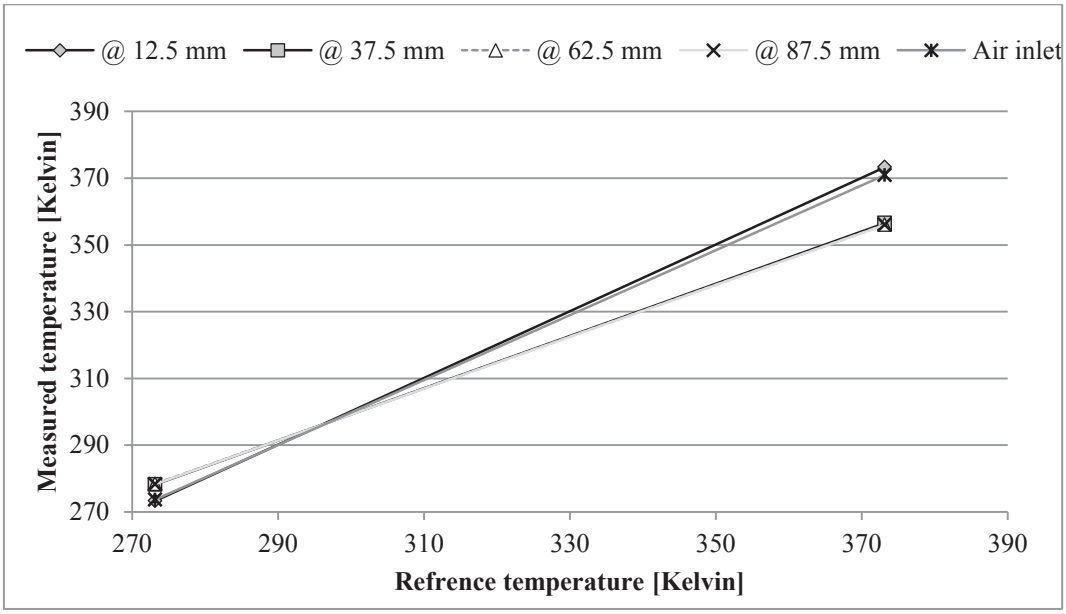


**Figure A-8 Calibration curves: Thermocouples**

Flow sensor is assumed to be calibrated as per manufacturer's specifications. The current output is therefore calibrated to sensor's displayed value. The calibration results are summarized in Table A-7 with calibration curve shown in Figure A-9.

**Table A-7 Flow sensor calibration information**

| Measurement | Zero offset | Measurement gradient |
|---|---|---|
| | [mA] | [Lpm/mA] |
| $\dot{V}_{supply}$ | 4.00546 | 3.12520 |

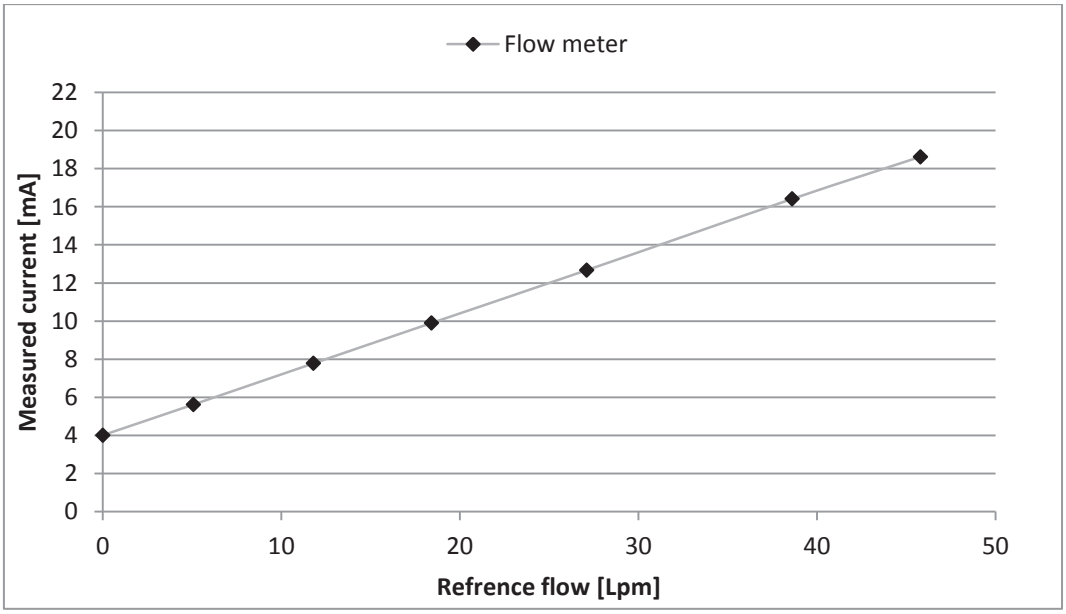


**Figure A-9 Calibration curves: Flow meter**

Calibration of the fuel metering column was performed with a calibrated metering column and 10ml syringe with specified 1% accuracy per millilitre. No calibration data is available for this measurement as it is user influenced. Therefore, statistical variance is used to quantify uncertainty of user involvement along with the specified calibration accuracy.

## A4. Uncertainty analysis

The full decomposition using in the uncertainty analyses found in sections 3.1.3 and 3.4 are presented here for clarity.

The focus of the uncertainty analyses is the mass flow parameters of paraffin and air, each determined from measurements as presented in equations 3-1 and 3-2 respectively.

Air mass flow rate calculated using equation 3-2. The error term for this parameter presented in equation 3-4 is obtained by decomposing each of the parameters of equation 3-2 except the Universal gas constant into a nominal value and an incremental error term as shown below.

$$\dot{m}_A = \dot{Vol}_{Air}\frac{P_{A,absolute}}{R_{dry\ air}\,T_A}$$

$$(\overline{\dot{m}_A} + \varepsilon_A) = \left(\overline{\dot{Vol}_{Air}} + \varepsilon_{\dot{Vol}_{Air}}\right)\frac{\left(\overline{P_{A,absolute}} + \varepsilon_{Pabs} + \varepsilon_{Pgauge}\right)}{R_{dry\ air}\,(\overline{T_A} + \varepsilon_T)}$$

$$\varepsilon_A = \frac{(\overline{\dot{Vol}_{Air}} + \varepsilon_{\dot{Vol}_{Air}})(\overline{P_{A,absolute}} + \varepsilon_{Pabs} + \varepsilon_{Pgauge})(\overline{T_A} + \varepsilon_T)}{R_{dry\ air}\left(\overline{T_A}^2 - \varepsilon_T^2\right)} - \overline{\dot{m}_A}$$

Because the error terms are assumed to have a small magnitude, higher order error terms become negligibly small in comparison and thus are neglected. The aforementioned equation then simplifies to equation 3-4.

$$\varepsilon_A \approx \varepsilon_{Pabs}\frac{\overline{\dot{Vol}_{Air}}}{R\overline{T_A}} + \varepsilon_{Pgauge}\frac{\overline{\dot{Vol}_{Air}}}{R\overline{T_A}} + \varepsilon_T\frac{\overline{P_{A,absolute}}}{R\overline{T_A}^2} + \varepsilon_{\dot{Vol}}\frac{\overline{P_{A,absolute}}}{R\overline{T_A}} \qquad 3\text{-}4$$

Using the similar procedure for paraffin flows using equation 3-1, equation 3-5 is derived. Equation 3-5 is used for both paraffin injection rate and accumulation rate.

$$\dot{m}_L = \frac{Vol_L\rho_L}{t_L}$$

$$(\overline{\dot{m}_L} + \varepsilon_L) = \frac{(\overline{Vol_L} + \varepsilon_{vol})(\overline{\rho_L} + \varepsilon_\rho)}{(\overline{t_L} + \varepsilon_t)}$$

$$\varepsilon_L \approx \varepsilon_\rho\frac{\overline{Vol_L}}{\overline{t_L}} + \varepsilon_{Vol}\frac{\overline{\rho_L}}{\overline{t_L}} + \varepsilon_t\frac{\overline{Vol_L}\,\overline{\rho_L}}{\overline{t_L}^2}$$

## A5. Equipment design

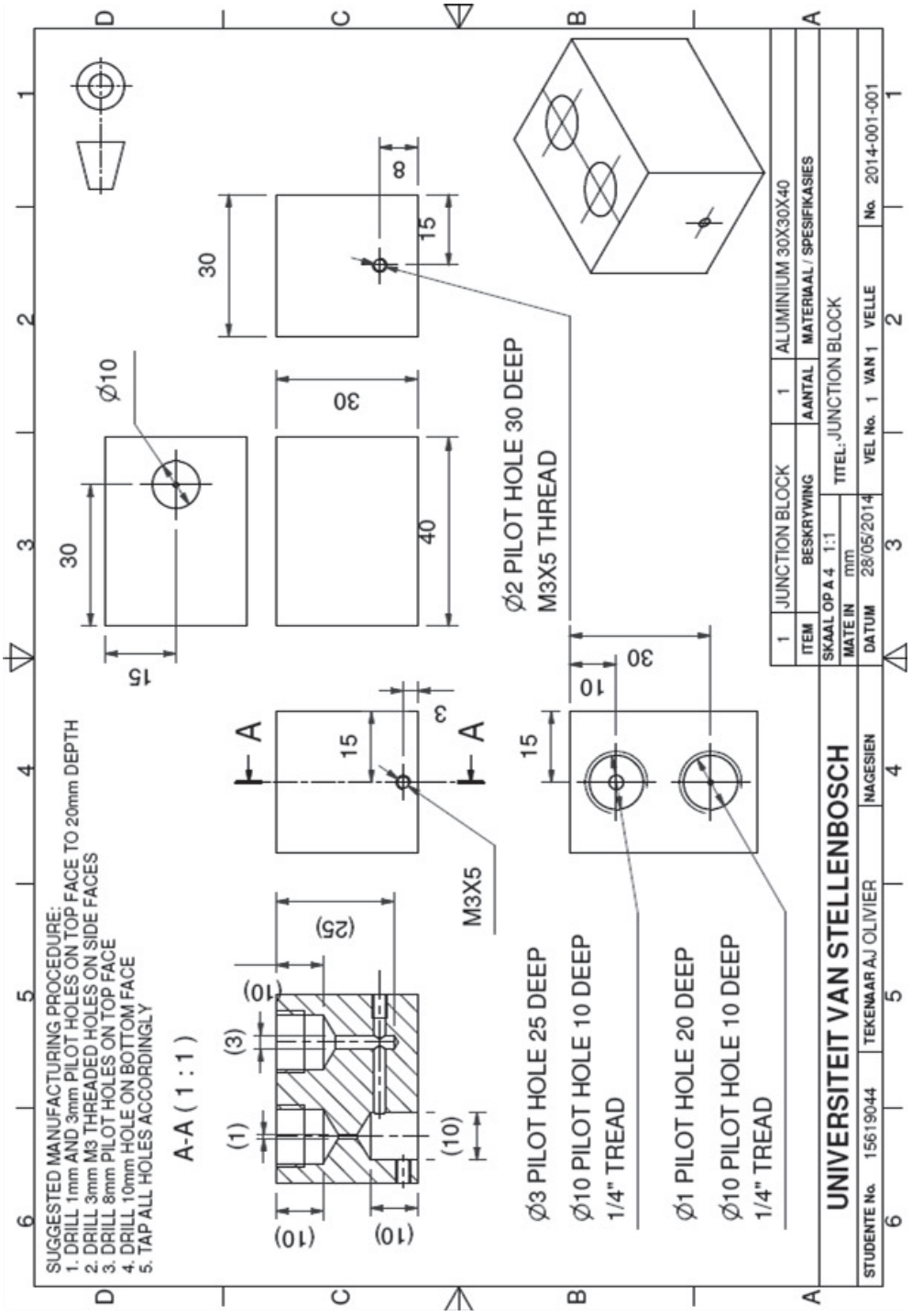


**Figure A-10 Manufacture drawing: Junction block**

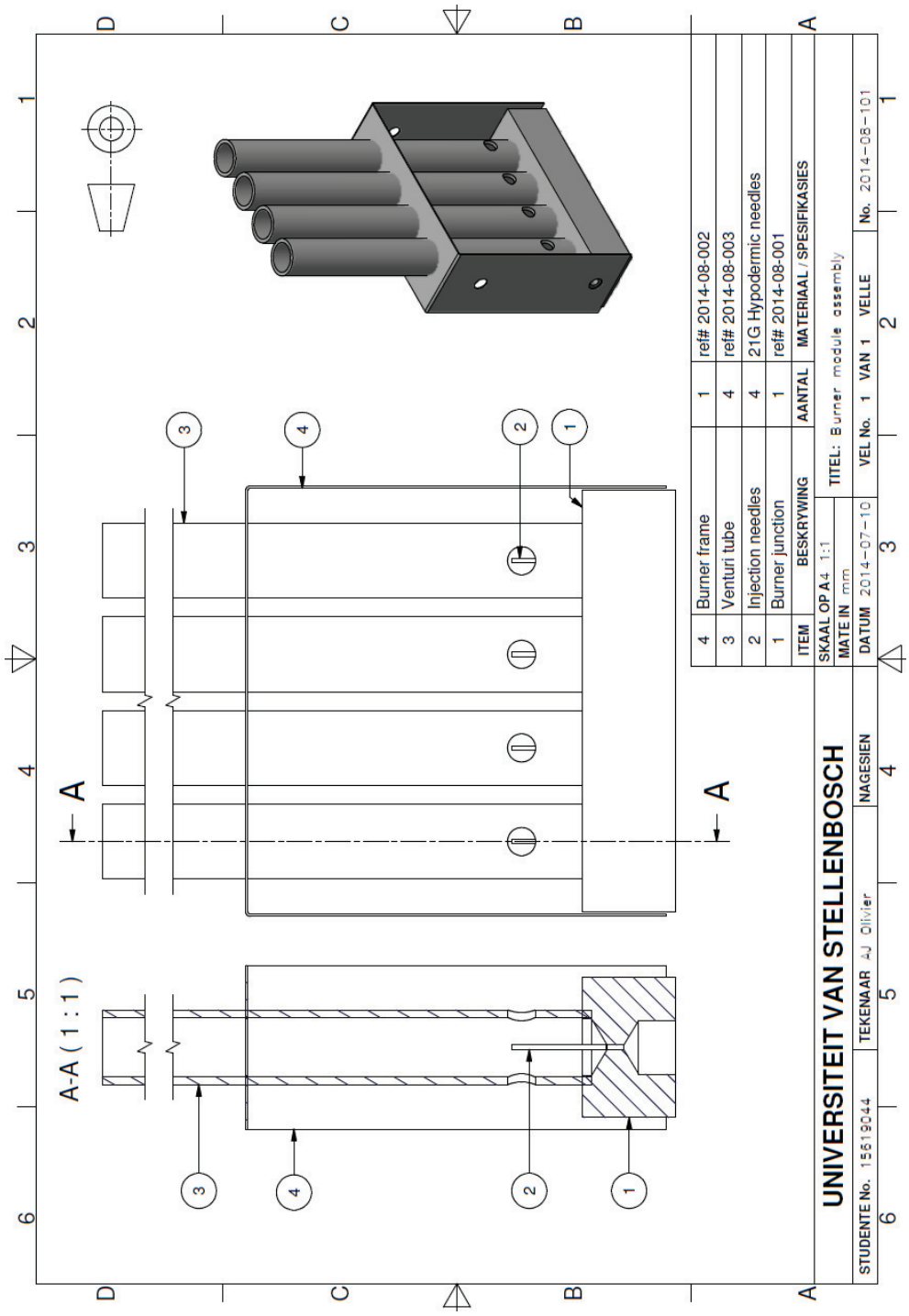


**Figure A-11 Manufacture drawing: Burner module assembly**

# A6. Component specifications

Festo SFAB volumetric flow meter:

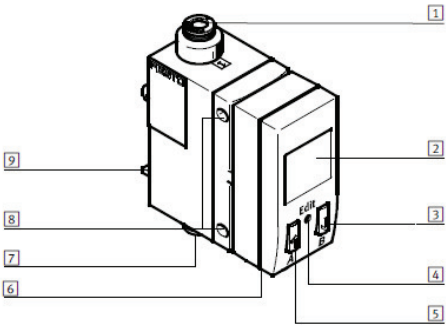


1 Supply port 1
➔ Marking on the product
2 Display
3 B button
4 Edit button
5 A button
6 Plug for electrical connection (M12)
7 Supply port 2
➔ Marking on the product
8 Hole for fitting the plate
9 Fastening slide for hat rail fitting and wall fitting (rear)

| SFAB | | -10U | -50U | -200U | -600U | -1000U |
|---|---|---|---|---|---|---|
| **General information** | | | | | | |
| Certification | | C tick, c UL us - Recognised (OL) | | | | |
| CE symbol (➔ conformity declaration) | | to EU EMC directive<br>to EU Explosion Protection Directive (ATEX) | | | | |
| Note on materials | | RoHS-compliant | | | | |
| **Input signal / Measurement element** | | | | | | |
| Measured variable | | flow, air consumption | | | | |
| Direction of flow | | unidirectional P1 → P2 | | | | |
| Measuring principle | | thermal | | | | |
| Flow measuring range | [l/min] | 0.1...10 | 0.5...50 | 2...200 | 6...600 | 10...1000 |
| Operating pressure | [bar] | 0...10 | | | | |
| Nominal pressure | [bar] | 6 | | | | |
| Pressure drop | [mbar] | < 100 | | | | |
| Ambient temperature | [°C] | 0...0 | | | | |
| Medium temperature | [°C] | 0...50 | | | | |
| Nominal temperature | [°C] | 23 | | | | |
| Operating medium | | Compressed air to ISO 8573-1:2010 [6:4:4] | | Compressed air to ISO 8573-1:2010 [7:7:4] | | |
| | | Nitrogen | | | | |
| **Output, general** [1] [2] | | | | | | |
| Accuracy, zero point ±FS [3] | [%] | 0.3 | | | | |
| Accuracy range ±FS [3] | [%] | 3 | | | | |
| Repeat accuracy, zero point ±FS | [%] | 0.2 | | | | |
| Repeat accuracy, zero point ±FS | [%] | 0.8 | | | | |
| Temperature coefficient range ±FS/K | [%] | ≤ 0.1 | | | | |
| Pressure-dependence range ±FS/bar | [%] | 0.5 | | | | |
| **Switching output** | | | | | | |
| Switching output | | 2x PNP or 2x NPN, adjustable | | | | |
| Switching symbols | | Window comparator or threshold-value comparator, adjustable | | | | |
| Switching element function | | NC or NO contact adjustable | | | | |
| Max. output current | [mA] | 100 | | | | |
| Voltage drop | [V] | max. 1.5 | | | | |
| Switch-on time | [ms] | adjustable (Factory setting: approx. 80 ms) | | | | |
| Switch-off time | [ms] | adjustable (Factory setting: approx. 80 ms) | | | | |
| Inductive protective circuit | | adapted to MZ, MY, ME coils | | | | |

| | | | | | | |
|---|---|---|---|---|---|---|
| **Analogue outputs** | | | | | | |
| Characteristic flow rate curve | [l/min] | 0...10 | 0...50 | 0...200 | 0...600 | 0...1000 |
| Output characteristics curve, current | [mA] | 4...20 | | | | |
| Output characteristics curve, voltage | [V] | 0...10 | | | | |
| Max. load resistance at current output | [Ohm] | 500 | | | | |
| Min. load resistance at voltage output | [kOhm] | 10 | | | | |
| Rise time | [ms] | 15, 30, 60 (factory setting), 125, 250, 500, 999 adjustable | | | | |
| **Output, additional data** | | | | | | |
| Protection against short circuit | | yes | | | | |
| Protection against overloading | | yes | | | | |
| **Electronics** | | | | | | |
| Operating voltage range DC | [V] | 15...30 | | | | |
| Protection against polarity reversal | | for all electrical connections | | | | |
| **Electromechanics** | | | | | | |
| Electrical connection | | straight plug, M12x1, 5-pin | | | | |
| Max. length of connecting cable | [m] | < 10 | | | | |
| **Mechanical components** | | | | | | |
| Temperature dependency of the throttle setting [4] ±FS (0...50 °C) | [%] | 8 | 8 | 2 | – | – |
| Assembly position | | as desired | | | | |
| Pneumatic connection | | QS6 | QS6 | – | – | – |
| | | QS8 | QS8 | QS8 | – | – |
| | | QS10 | QS10 | QS10 | QS10 | QS10 |
| | | QS12 | QS12 | QS12 | QS12 | QS12 |
| | | QS¼ | QS¼ | – | – | – |
| | | QS⅜ | QS⅜ | QS⅜ | – | – |
| | | QS½ | QS½ | QS½ | QS½ | QS½ |
| Product weight | [g] | 160 | | | | |
| Material of housing | | reinforced polyamide | | | | |

## A7. Experimental procedure to determine flow through vaporizers

The mass flow through the combustor and each of its individual hole set and vaporizer tube bundle is determined by measuring the difference in air mass flow that moves through the combustor. For this study it is required to determine the amount of air flow through the vaporizer tube bundle. Thus, the mass flow through the combustor is measured for a case with all holes and vaporizers open and a case where the vaporizers are blocked off.

The air mass flow measurement is achieved using an orifice plate flow meter according to the BS1042 standard. The orifice diameter, pipe diameter and resulting ratio between these diameters have values as shown.

$$D_{orriface} = 100mm$$
$$D_{pipe} = 160mm$$
$$\beta = \frac{D_{orriface}}{D_{pipe}} = 0.625$$

Measurements are made for the differential pressure across and the pressure and temperature upstream of the orriface and are represted by the symbols $P_{deltabar}$, $P_{cerabar}$ and $T$ respectively.

The mass flow is determined from measurements and orriface specification as indicated in equation A-1.

$$\dot{m} = C_d \pi \left(\frac{D_{orriface}}{2}\right)^2 \sqrt{\frac{2P_{deltabar}\rho}{1-\beta^4}} \qquad \text{A-1}$$

The discharge coefficient, $C_d$, is determined from a correlation presented by Cengel and Cimbala shown in equation A-2 and is valid for Reynolds numbers in the range of .

$$C_d = 0.5959 + 0.0312\beta^{2.1} - 0.184\beta^8 + 91.71\beta^{2.5}Re^{-0.75} \qquad \text{A-2}$$

The Reynolds number required is calculated as shown in equation A-3.

$$Re = \frac{4\dot{m}}{D_{pipe}\pi\mu} \qquad \text{A-3}$$

Apparent from the structure of these the three aforementioned equations, implicit calculations are required. The scheme used for this study used a guessed Reynolds value within the specified range and then proceeded to update the value until its value remained unchanged.

The air density is calculated assuming ideal gas behaviour and using the molecular weight for dry air. Viscosity is determined using a correlation by Kroger (1998) as shown in equation A-4.

$$\mu = 2.288 \times 10^{-6} + 6.260 \times 10^{-8}T - 3.132 \times 10^{-11}T^2 + 8.150 \times 10^{-15}T^3 \qquad \text{A-4}$$

The method described above is performed on the two cases related to flow through combustor with and without blocking the flow through the vaporizers. Measurements are summarized in Table A-8 with atmospheric pressure remaining constant at $101.8\ kPa$ during tests.

**Table A-8 Air flow through vaporizers: Measurements**

| **Input variables** | | **Measured values** | | | **Calculated values** | | | |
|---|---|---|---|---|---|---|---|---|
| Fan frequency | Temperature at orifice | Cerabar | Deltabar | Downbar | Density | Viscosity | Cd | Mass flow rate |
| [Hz] | [K] | [kPa] | [kPa] | [kPa] | [kg/m3] | [$10^{-5}$ Ns/m] | [-] | [g/s] |
| All holes open | | | | | | | | |
| 10 | 294.15 | 0.210 | 0.013 | 0.197 | 1.208 | 1.820 | 0.626 | 29.950 |
| 20 | 294.15 | 0.857 | 0.052 | 0.805 | 1.216 | 1.820 | 0.617 | 59.202 |
| 30 | 294.15 | 1.953 | 0.120 | 1.833 | 1.229 | 1.820 | 0.613 | 89.867 |
| 40 | 294.15 | 3.511 | 0.216 | 3.295 | 1.247 | 1.820 | 0.611 | 121.069 |
| 50 | 294.15 | 5.516 | 0.340 | 5.176 | 1.271 | 1.820 | 0.610 | 153.007 |
| Vaporizer holes closed | | | | | | | | |
| 10 | 294.15 | 0.210 | 0.012 | 0.198 | 1.208 | 1.820 | 0.627 | 28.807 |
| 20 | 294.15 | 0.858 | 0.048 | 0.810 | 1.216 | 1.820 | 0.618 | 56.918 |
| 30 | 294.15 | 1.954 | 0.110 | 1.844 | 1.229 | 1.820 | 0.614 | 86.088 |
| 40 | 294.15 | 3.512 | 0.197 | 3.315 | 1.247 | 1.820 | 0.612 | 115.675 |
| 50 | 294.15 | 5.518 | 0.307 | 5.211 | 1.271 | 1.820 | 0.610 | 145.456 |

Blockage of the vaporizers is seen to have minimal effect on the fan loading apparent from the close similarity of upstream pressure with corresponding supply frequencies. As such less error is induced by direct comparison of the mass flow rates with relation to input frequency than with curve fitted functions relative to upstream pressure. The corresponding mass flow rates and apparent variation is summarized in Table A-9.

**Table A-9 Air flow through vaporizers: Mass flow percentages**

| Frequency [Hz] | All holes open [g/s] | Vaporizers closed [g/s] | Difference [g/s] | as % of all open |
|---|---|---|---|---|
| 10 | 29.950 | 28.807 | 1.143 | 3.82% |
| 20 | 59.202 | 56.918 | 2.284 | 3.86% |
| 30 | 89.867 | 86.088 | 3.779 | 4.20% |
| 40 | 121.069 | 115.675 | 5.393 | 4.45% |
| 50 | 153.007 | 145.456 | 7.551 | 4.93% |

The amount of air permitted through the vaporizers is observed to vary between 3.82% and 4.93% of the total air permitted through the combustor.

# Appendix B.
# *Numerical work*

## B1. Numerical algorithm

The numerical algorithm is presented here in pseudo code logical flow structure.

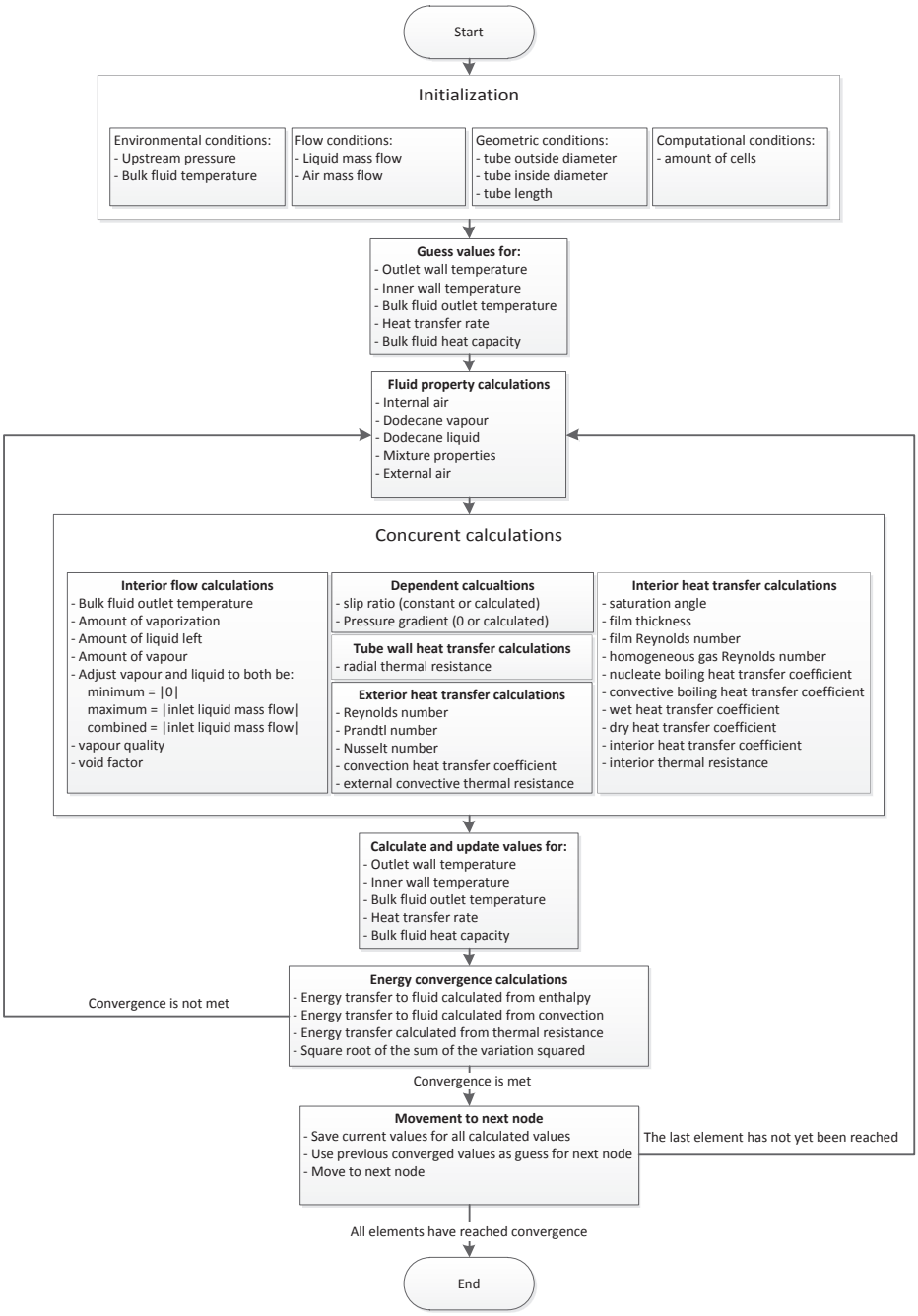

## B2. Property models

Property models were derived from property values obtained from miniREFPROP version 9.1 using the NIST Standard Reference Database 23. Models are fitted using least-squares curve method to tabulated data obtained at a constant pressure of 100kPa. This is done under the assumption of negligible influence of pressure on property values except gaseous densities where ideal gas behaviour is assumed.

**Constant fluid properties:**

$$T_{sat,Dodacane} = 489.44\ K$$
$$h_{fg,Dodacane} = 256.16\ kJ/kg$$

**Homogeneous gas and mixture properties**

$$Pr_V = (Pr_A\dot{m}_A + Pr_V\dot{m}_V)/(\dot{m}_A + \dot{m}_V)$$
$$k_V = (k_A\dot{m}_A + k_V\dot{m}_V)/(\dot{m}_A + \dot{m}_V)$$
$$\mu_G = (\mu_A\dot{m}_A + \mu_V\dot{m}_V)/(\dot{m}_A + \dot{m}_V)$$
$$c_{p_M} = \left(c_{p_A}\dot{m}_A + c_{p_V}\dot{m}_V + c_{p_L}\dot{m}_L\right)/(\dot{m}_A + \dot{m}_V + \dot{m}_L)$$
$$\rho_G = (\dot{m}_A + \dot{m}_V)/(\dot{m}_A\rho_A^{-1} + \dot{m}_V\rho_V^{-1})$$

**Property models for air:**

$$Pr_A = \begin{matrix} T < 600\ : & 5.1762\times10^{-7}T^2 - 5.8336\times10^{-4}T + 0.85714 \\ T > 600\ : & 4.8971\times10^{-5}T + 0.66239 \end{matrix}$$
$$k_A = 5.66043\times10^{-5}T + 1.00757\times10^{-2}$$
$$\mu_A = 3.1561\times10^{-8}T + 1.0123\times10^{-5}$$
$$c_{p_A} = -2.7451\times10^{-7}T^3 + 6.4472\times10^{-4}T^2 - 0.25940T + 1032$$
$$\rho_A = (PM_{air})/(RT)$$

**Property models for liquid dodecane:**

$$Pr_L = 2.1218\times10^{8}T^{-2.8229}$$
$$k_L = -2.1320\times10^{-4}T + 0.19863$$
$$\mu_L = 1.5497\times10^{7}T^{-4.0651}$$
$$c_{p_L} = 3.8639T + 1056.5$$
$$\rho_L = -0.77775T + 978.69$$

**Property models for vapour dodecane:**

$$Pr_V = -3.5332\times10^{-5}T + 0.76873$$
$$k_V = 1.0149\times10^{-4}T - 0.025214$$
$$\mu_V = 1.6702\times10^{-8}T - 7.5154\times10^{-7}$$
$$c_{p_V} = 3.0254T + 1037.3$$
$$\rho_V = (PM_{dodacane})/(RT)$$

Tabulated data and fitted curves are presented in the proceeding graphs.

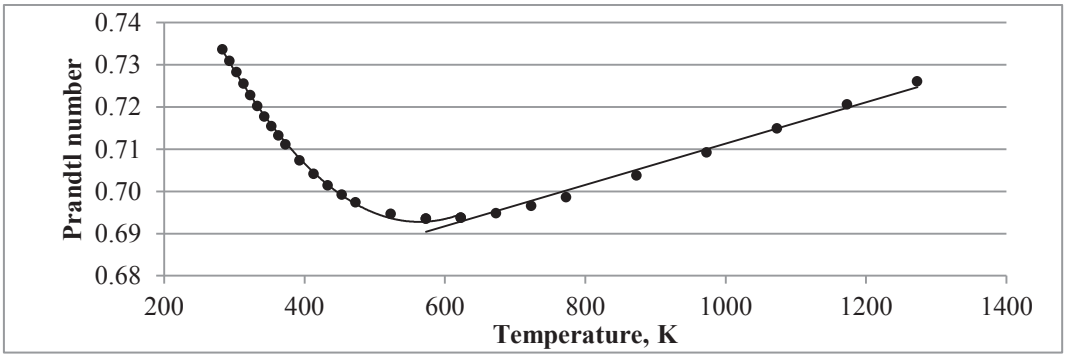


(a) Prandtl number

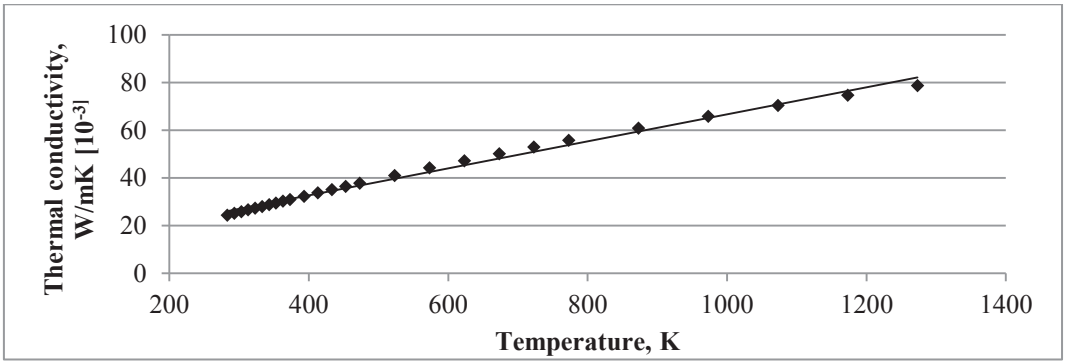


(b) Thermal conductivity

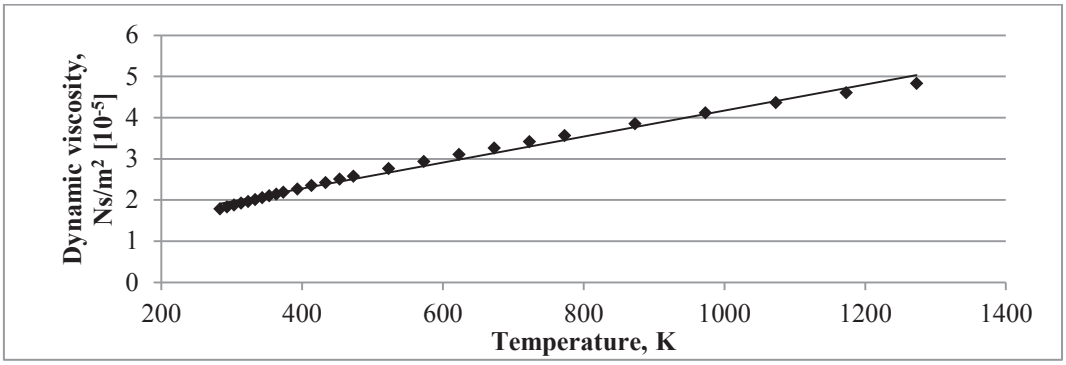


(c) Dynamic viscosity

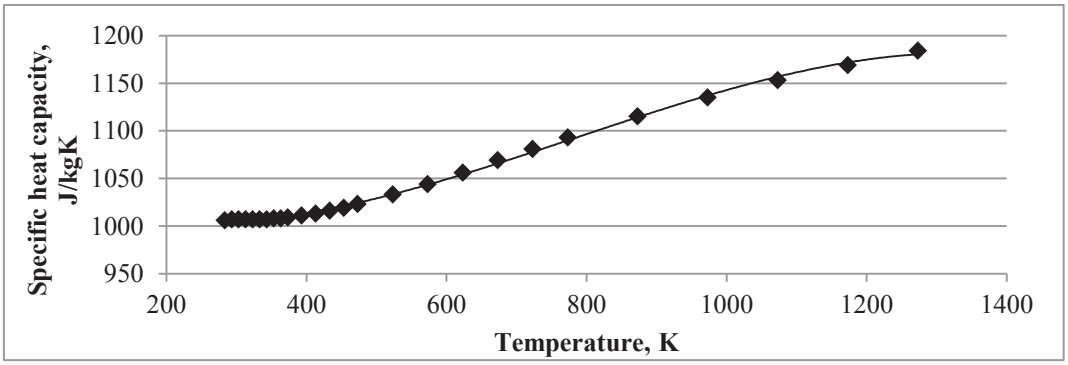


(d) Specific heat

**Figure B-1 Property models: Air**

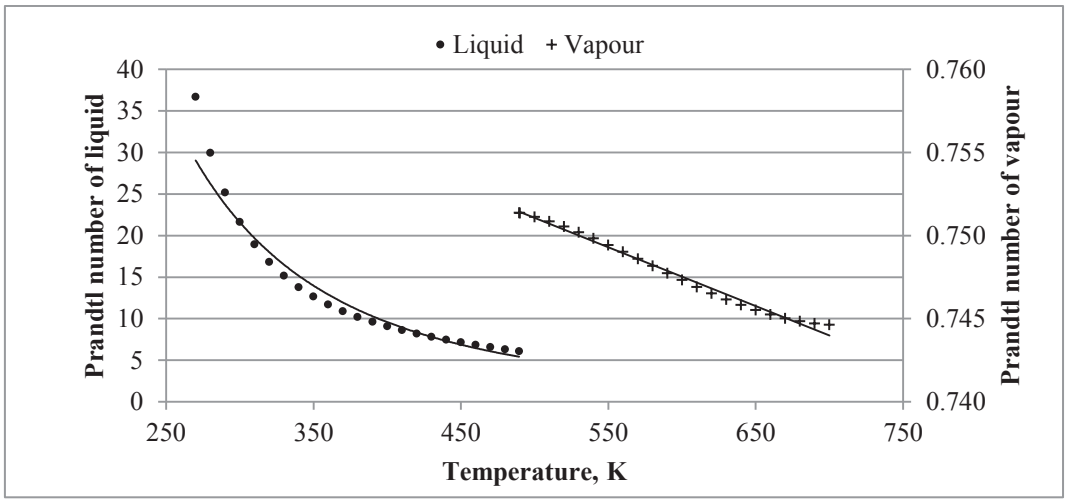


(a) Prandtl number

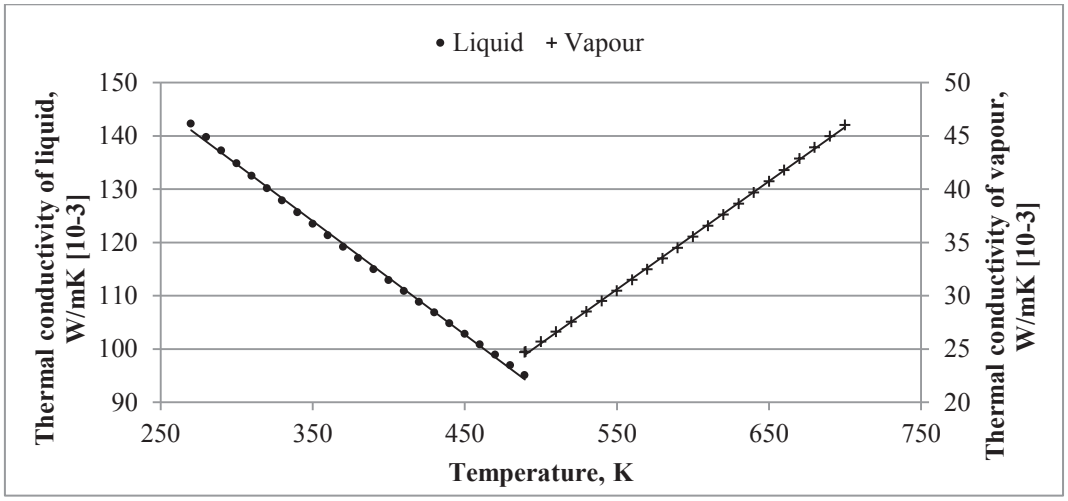


(b) Thermal conductivity

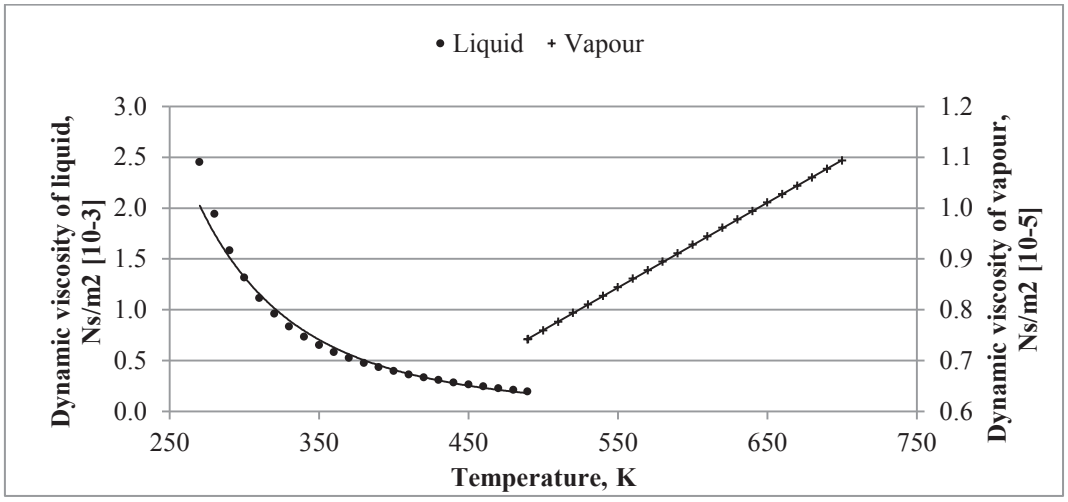


(c) Dynamic viscosity

**Figure B-2 Property models: Dodecane**

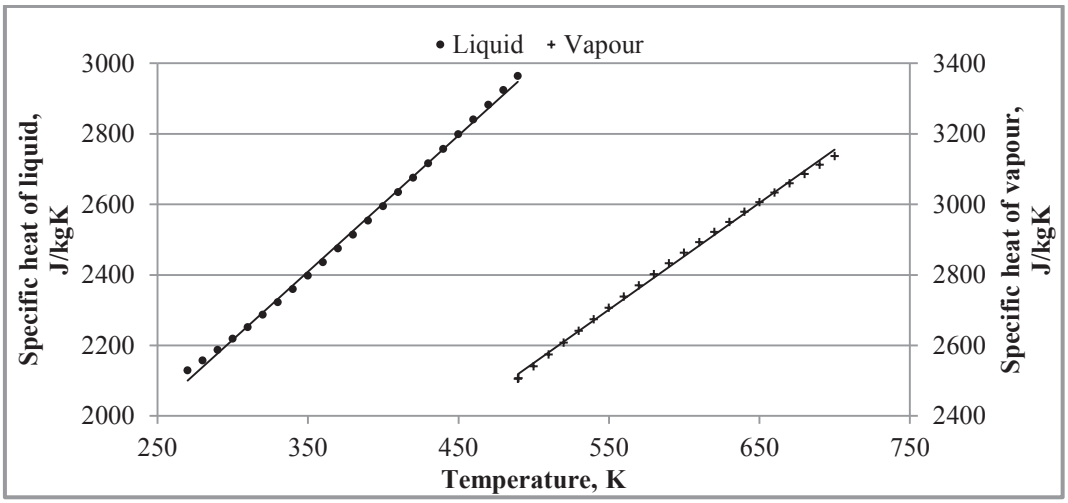


(d) Specific heat

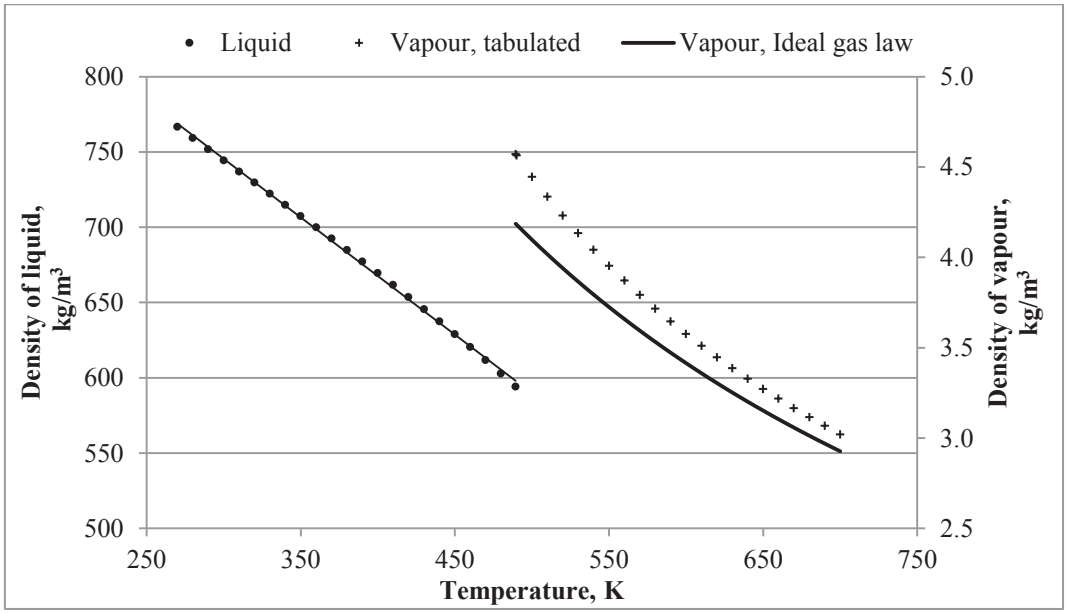


(e) Density

**Figure B-2 Property models: Dodecane**